Université Sorbonne Paris Cité

Thèse de doctorat
De l'université Sorbonne Paris Cité
Préparée à l'Université Paris Diderot
Ecole doctorale Physique en Ile-de-France
Laboratoire Matériaux et Phénomènes Quantiques
Equipe Microscopie electronique Avancée et Nano-Structures

Nanoscale *in situ* studies of Au and Au-Cu nanoparticle synthesis by liquid-cell transmission electron microscopy

Par Nabeel AHMAD

Thèse de doctorat de Physique

Dirigée par Damien Alloyeau et Christian Ricolleau

23 Novembre 2017

TESTARD Fabienne, Ingénieur CEA	RAPPORTEURE
MOLHAVE Kristian, Pr.	RAPPORTEURE
GIORGIO Suzanne, Pr.	RAPPORTEURE
PIQUEMAL Jean-Yves, Pr.	PRESIDENT DE JURY
ALLOYEAU Damien, C.R.	Co-DIRECTEUR DE THESE
RICOLLEAU Christian, Pr.	DIRECTEUR DE THESE

Acknowledgements

I would like to acknowledge the support of several individuals to whom I am highly indebted to regarding the completion of my PhD research.

First and foremost I would like to express my deep gratitude and appreciation to Dr. Damien Alloyeau who was instrumental in encouraging me to proceed with this project. It was a pleasure for me to work in a conducive research environment which enabled me to experiment with novel ideas. I believe through his sheer patience, advice and trust in my abilities, Dr Damien was able to hone my skills as a research scientist. I would also like to thank the valuable insights of my committee members, Dr. Kristian Molhave, Dr. Fabienne Testard, Dr. Suzanne Giorgio and Dr. Jean-Yves Piquemal.

I am also thankful for the valuable discussions conducted during regular lab meetings. In this regard Prof. Christian Ricolleau and Dr. Jaysen Nelayah were central figures who gave very useful suggestions. Additionally the support of our lab engineer Dr. Guillaume Wang was absolutely critical for my work as those in TEM community know the ever present technical glitches in instrumentation. These acknowledgements would not be complete without mentioning my lab colleagues, Ouafi Mouhoub and Adrian Chmielewski. They provided a great working atmosphere along with good sense of humor.

The work could not have materialized without the support of National University of Sciences & Tech. research grant. This grant partially funded my PhD project for which I am highly grateful.

Lastly but not least, I would like to acknowledge the support of my family and friends. They were a constant source of motivation throughout the entire duration of my Phd thesis. I deeply appreciate their patience and understanding.

Abstract

Recent years have seen a remarkable increase in research activities related to the synthesis of metallic nanocrystals. This intense interest is fueled by the unique and fascinating properties delivered at such size domains. Indeed, electrons confinement by nanocrystals is a powerful means to modulate electronic, optical and magnetic properties of a material. Most current strategies employ chemical synthesis to formulate unique nanoparticle morphologies by exploiting the versatility of liquid reaction media to control the formation mechanisms. Although the chemistry of metal nanocrystal synthesis is not complicated, understanding the nucleation and growth processes in complex liquid media and the influence of each chemical species is altogether a different challenge. It is in this regard, that we have utilized liquid cell transmission electron microscopy to visualize relevant growth phenomenon at the nanoscale. This recent *in situ* technique allowed us to study in real time the dynamics of growth of Au and Au-Cu nanoparticles in reaction media of controlled composition. The primary goal of this thesis was to distinguish the kinetics effects (related to the flow of matter) and the thermodynamics effects (related to the environment-dependent equilibrium of nanostructures) on final nanoparticle shapes. In addition to this, systematic studies were performed to separate the inevitable beam effects from the influence of specific synthesis parameters such as the seed crystal morphology and the organic functionalization that are of primary importance for colloidal chemists. Beam induced phenomena were also utilized to understand the solution chemistry of the exposed solvent which is in turn responsible for driving reversible redox reactions in bimetallic nano-systems.

Résumé

La fabrication de nano-cristaux métalliques suscite un effort de recherche en constante augmentation depuis plusieurs années. Cet immense intérêt est motivé par les propriétés uniques et fascinantes qui apparaissent à l'échelle des tailles nanométriques. En effet, le confinement des électrons au sein d'un nanocristal est un moyen puissant de moduler les propriétés électroniques, optiques et magnétiques d'un matériau. Les synthèses par voies chimiques sont des stratégies très repandues pour fabriquer des nanoparticules métalliques avec des morphologies originales en exploitant la versatilité des milieux réactionnels liquides pour contrôler les mécanismes de formation. Cependant, si la chimie employée lors de ces synthèses n'est pas très compliquée, la compréhension des processus de nucléation/croissance en milieu liquide complexe et l'influence de chaque espèce chimique est un tout autre challenge. Pour y répondre, nous avons utilisé la microscopie électronique en transmission en milieu liquide pour visualiser des phénomènes de croissance à l'échelle nanométrique. Cette récente technique de microscopie *in situ* nous a permis d'étudier en temps réel la dynamique de croissance de nanoparticules d'or et d'or-cuivre dans des milieux réactionnels de composition contrôlée. Le premier objectif de cette thèse était de distinguer les effets cinétiques (liés aux flux de matière) et les effets thermodynamiques (liés à l'équilibre des nanostructures en fonction de leur environnement) qui dictent tous les deux la forme finale des nanoparticules. De plus, des études systématiques nous ont permis de séparer les inévitables effets du faisceau d'électron, des effets de paramètres spécifiques de la synthèse, comme la forme des germes ou la fonctionnalisation organique, qui sont de toute première importance en chimie des colloïdes. Enfin, des phénomènes induits par le faisceau ont aussi été exploité pour comprendre l'influence de l'irradiation sur la chimie du milieu réactionnel, qui peut induire des réactions d'oxydo-réductions réversibles et contrôlables dans les nano-systèmes bimétalliques.

Table of contents

General Introduction

The idea of studying nanomaterials in liquids using a transmission electron microscope (TEM) had always fascinated chemists and materials scientists alike. The main hurdle was enshrined in the basic fact that liquids were incompatible with the high vaccum environment of a typical TEM instrument[1]. The solution was simple yet impractical for variety of reasons. Therefore, until a little over a decade ago observations of crystal growth in liquid environment were uncommon and even impossible in most cases. It is only in the past few years that this dream has become a reality due to massive improvement in microfabrication technology of liquid cell chambers. Liquid cell transmission electron microscopy (LCTEM) opens up an opportunity to study biological structures without the need for freezing as well as operando electrochemical processes and nanomaterial dynamics (growth, etching, self-assembling…)[2]. A plethora of recent studies have appeared in recent years demonstrating the true potential and application of liquid cell electron microscopy[3-7].

In this thesis we focus on the materials science aspects of liquid cell electron microscopy. Although the success in directly observing nucleation processes is still limited since the nanocrystals observed by electron microscopists have already grown beyond the nucleation stage, however being able to dynamically observe even the seed crystal growing into a final nanocrystal shape can reveal remarkable insights into the growth mechanisms of metallic and bimetallic nanoparticles[8, 9]. Utilizing the excellent spatial and temporal resolution provided by this technique, this PhD thesis focuses on the formation processes of Au and Au-Cu nanoparticles. With the view to provide a fresh look at well-established fabrication strategies of nanocrystals, our primary challenge is to identify the individual role of key parameters of the growth process of nanoparticles: (i) the growth speed, (ii) the structure of the initial seeds, (iii) the surface functionalization, (iv) the type of solvent, (v) oxidative etching and of course (vi) the effects of the electron beam that are inherent to LCTEM. This work formed part of the larger project undertaken few years ago by Dr. Damien Alloyeau (MeANS team) at Paris Diderot University. The environmental electron microscopy facilities at the lab provide state of the art facilities such as aberration corrected ARM 200F microscope and commercial Poseidon 210 *in situ* liquid holder to monitor dynamics of these interesting nano objects.

References

1. Ross, F. M. *Science* **2015,** 350, (6267), aaa9886.
2. De Jonge, N.; Ross, F. M. *Nature nanotechnology* **2011,** 6, (11), 695-704.
3. Liao, H.-G.; Zheng, H. *Journal of the American Chemical Society* **2013,** 135, (13), 5038-5043.
4. Mehdi, B. L.; Qian, J.; Nasybulin, E.; Park, C.; Welch, D. A.; Faller, R.; Mehta, H.; Henderson, W. A.; Xu, W.; Wang, C. M. *Nano letters* **2015,** 15, (3), 2168-2173.
5. Mirsaidov, U.; Matsudaira, P., Nanoscale Water Imaged by In Situ TEM. In *Liquid Cell Electron Microscopy*, Ross, F. M., Ed. Cambridge University Press: Cambridge, 2016; pp 258-275.
6. Peckys, D. B.; de Jonge, N. *Nano letters* **2011,** 11, (4), 1733-1738.
7. Zheng, H.; Claridge, S. A.; Minor, A. M.; Alivisatos, A. P.; Dahmen, U. *Nano letters* **2009,** 9, (6), 2460-2465.
8. Xia, X.; Xia, Y. *Nano letters* **2012,** 12, (11), 6038-6042.
9. Xia, Y.; Xiong, Y.; Lim, B.; Skrabalak, S. E. *Angewandte Chemie International Edition* **2009,** 48, (1), 60-103.

Chapter 1

Introduction

1.1 Understanding the Growth Mechanisms of Metallic Nanoparticles: A Challenge in Materials Sciences

A detailed understanding of nanoscale growth processes is of paramount importance for designing complex new systems. This is especially true from a materials science perspective since most nanomaterials have a size range of few nanometers and lie in the domain between molecular sizes and bulk materials[1]. This attribute of nanocrystals leads to them exhibiting physical and chemical properties somewhere in between. At nanoscale the quantum confinement of the electrons or photons can be used to manipulate optical, electronic and magnetic properties of nanocrystals. Recent years have seen a plethora of applications for these novel structures ranging in areas such as life sciences, energy conversion & storage and electronics and catalysis. The foremost challenge in harnessing the true potential of these nanomaterials is in controlling the size and shape parameters. Changing either of these physical parameters may result in a remarkable change in functional properties of the material. Additionally other parameters such as type of exposed facet on the surface of the nanocrystal may result in change of catalytic activity[2] simply due to change in atomic packing order. Among all different kinds of nanomaterials, metallic nanostructures are among most studied due to their ease of characterization and interesting applications in photonics and catalysis.

Among nanocrystal fabrication routes, liquid phase synthesis is the most versatile one for the formation of complex morphologies. Like all bottom-up synthesis methods, the growth of metallic nanostructures in liquid is simultaneously driven by kinetic and thermodynamic effects, dictated by the flows of matter (growth speed) and the stability of nanomaterials with their environment, respectively. Therefore, a wide variety of strategies have been explored to manipulate the growth processes with the view to control the shape of nanoparticles. They all consist in controlling the growth speed and/or the environment-dependent equilibrium of the

nanostructures. Many review articles have already discussed the shape-controlled syntheses of metal nanocrystals[3-7]. It is therefore clear that the use of shape-specific seeds, capping agents and/or oxidative etching agents are three methods of choice to control the growth processes. Briefly, seed-mediated synthesis consists in inserting single-crystal, singly or multiply-twinned clusters in the reaction media. As the low-index facets or the twin planes of these clusters can be preferential sites for ad-atom adsorption, oriented or anisotropic growth can be exploited to fabricate metallic nanoparticles with various morphologies, including nanorods, bipyramids, nanoplates and faceted 3D morphologies like octahedral, decahedral and icosahedral nanoparticles[8-12]. If the correlation between the symmetry of the seeds and the final shape of the nanocrystals was established by *ex situ* TEM, understanding the complex atomic mechanisms involved in these transformations remains a challenge that can only be overcome with *in situ* nanoscale analyses. The use of capping agents that are able to selectively functionalize the facets of nanoparticles is frequently described as thermodynamic means to control the shape of nanocrystals. Thus, surface capping is expected to favor the stability of particular facets by reducing their interfacial free energies through chemisorption[7, 13]. However, despite the importance of face-blocking methods in nanomaterial synthesis, the explicit roles of functionalization in the growth mechanisms are poorly defined, because it cannot be unambiguously determine by analyzing *ex situ* snapshots of nanomaterials extracted from their formation medium at given time points of the synthesis. Usable with various metals, selective-surface etching that occurs in presence of complexing and oxidative agents can also be exploited to select the type of seeds formed in solution[14] or to reach nanocrystals shapes which cannot be synthesized with conventional growth methods[15]. Interestingly, atomic-level oxidative etching is also a major factor for the degradation of nanostructures used in electrocatalysis[16] and in biological media[17]. Nevertheless, the dissolution dynamics of nanomaterials as function of their shape, structure, composition or dispersion in solution remains elusive without *in situ* nanoscale observations. To summarize, in metallic nanoparticle synthesis chemical reactions are fairly simple, however for a long time the main hurdle faced by colloidal chemists was the lack of tools to study the complex atomic-scale mechanisms arising at solid-liquid interfaces[3]. Therefore, the development of *in situ* microscopy techniques such as LCTEM, provides unique possibilities to end the guessing game regarding the formation mechanisms of complex nanomaterials.

1.2 Development of Liquid Cell TEM

Tackling this core issue of following nanoparticle growth requires use of recent advances that have been made in the form of liquid cell transmission electron microscopy (LCTEM). LCTEM is a relatively new field in the process of development. Despite this it has already made significant contributions in studying nanoscale processes[18]. Since the early development of electron microscopes there has been a desire to image liquids as it is the natural medium of many nanoscale phenomena. The main hindrance in realizing this goal was the incompatibility of microscope vacuum with the high vapor pressures of the liquids such as water which is the solvent of choice for most chemical reactions. Another area of concern was controlling the liquid thickness[19]. Too thick of a liquid layer may result in complete loss of signal due to multiple scattering events while very thin liquid layer might not mimick the actual experimental conditions of growth. Advances in microfabrication technology and microscope design have enabled researches to overcome these issues.

Other *in situ* methods have been developed for analyzing the nucleation and growth of nanomaterials in liquid environments. Many *in-situ* studies have been carried out using multitude of X-ray techniques, for which the high brilliance of the synchrotron radiation is an essential benefit to probe dynamic nanoscale processes with a high degree of temporal resolution. For example *in-situ* small angle and wide angle x-ray scattering techniques together with UV-visible spectroscopy is an efficient combination to follow in real time the density, the size distribution and the atomic structure of metallic nanoparticles during liquid phase syntheses[20, 21]. By probing the concentration of metallic species with different redox states, X-ray absorption near edge structure (XANES) spectroscopy can provide additional information on the chemical mechanisms implied in the reaction media[22]. The use of fast mixing liquid-cell, which have less constraining size limitations than liquid-cells for TEM, enables quantitative studies of the growth and reaction kinetics as a function of the environment composition (the effects of ligands, presence of seeds…). Nevertheless, as the data of X-ray scattering and absorption are averaged over large nanoparticle assemblies, the interpretation of nanoscale processes under study is time consuming and it becomes more complex when size or shape dispersions are involved. It is worth noticing that the developments of *in situ* X-ray microscopy techniques, such as scanning transmission X-ray microscopy (STXM) are very promising and complementary approaches to probe nanoscale processes in liquid with a good chemical sensitivity (XANES) and a resolution of a few tenth of

nanometers[23]. *In liquid* microscopy has also been developed on near field microscopes such as AFM or STM. For example, Simm et al. have utilized AFM to study nucleation and growth of cobalt on boron doped diamond electrode under potentiostatic control[24]. They were able to measure the growth rate of the nuclei by using AFM as a function of time at varying deposition potentials. While offering certain benefits, *in situ* AFM and STM suffer inherent limitations due to sample preparations and to poor temporal resolution. In this context, liquid-cell TEM offers the unique benefits of imaging nanoscale processes at a high temporal and spatial resolution with direct imaging. This aspect being unrivalled by any other *in situ* technique at such scales.

1.3 Flexibility and Limitations of LCTEM Methods

Currently liquid cell electron microscopy is carried out using either a transmission electron microscope (TEM) or a scanning electron microscope (SEM). TEM provides the choice of operating the instrument in two modes i.e. TEM mode where the beam is spread and is parallel to the optical axis or scanning transmission electron microscopy (STEM) mode whereby a finely focused probe is rastered over the sample surface generating signals. Two approaches have been devised for imaging liquids in electron microscopes. Environmental chambers have been designed whereby differential pumping is used to formulate an area in sample chamber where liquid and vapor co-exist usually around 0.2 bar while rest of microscope remains at low pressure[25]. This however entails the problem of maintaining a workable liquid profile. In TEM the sample should be extremely thin otherwise the electrons cannot be transmitted which is not the case for SEM as the signal is generated from the surface and liquid thickness is not an issue. SEM technique for liquid imaging is outside the scope of this thesis. The more common approach is use of liquid cell having very thin and stable electron transparent windows which isolate the liquid as well as maintain a stable liquid profile within reasonable limits. The entire assembly is hermetically sealed in the tip of the sample holder. Using this technique liquid layers of several micrometers were created initially. It has been shown in one of the earliest works performed by Abrams et al. in 1944 that a liquid of 1 μm thickness is virtually opaque to electron beam[26] with spatial resolutions not much better than visible light microscopy. With the unavailability of techniques to form thin membranes which are permeable to electrons yet stiff enough to withstand high pressure differentials there was a relative calm in liquid electron microscopy for a period of time. With recent advances in thin film technologies there is a newfound interest in the development of this technique. Membranes of amorphous carbon can be used to formulate

windows of E-cell to observe *in situ* atomic scale reactions of catalysts and image liquid samples (Sugi et al., 1997; Giorgio et al., 2006)[27, 28]. However the most popular liquid cells nowadays are essentially made up of 30-100nm SiN membranes supported on silicon E-chips (See chapter 2). These are more homogenous and stiffer than other options yet more easily manufactured on a bulk scale. Recently graphene sheets are employed[29, 30] to obtain an unprecedented atomic resolution since it is the thinnest material and is impermeable to liquid. Using SiN based liquid cells the resolution limit of different forms of electron microscopy have been calculated in the work of de Jonge et al[25]. These measurements have been carried out on typical instruments at 200KV using a SiN membrane of 30 nm thickness at varying water thicknesses as shown in figure 1. The resolution of both TEM and STEM imaging drastically improves as the thickness of liquid goes below 1µm. The graph also quantitatively shows that the difference between resolutions of STEM and TEM increases with increasing liquid thickness while at low thicknesses the difference is not huge. SEM resolution is unaffected by the liquid thickness. In TEM mode the resolution is limited mostly by the chromatic aberrations due to inelastic scattering of the electrons causing an energy spread. The best resolution in this mode is obtained on the exit surface of the object i.e. on the lower membrane of the cell. Following equation describes the resolution in liquids in TEM mode[25]:

$$D_{TEM} = 6 \times 10^{12} \frac{\alpha C_c T}{E^2}$$

Here E is the beam energy, T is liquid thickness, C_c is the chromatic aberration constant whereas α is the objective semi-angle [31]. The resolution values obtained through this equation are only true for objects on exit side of the sample but may well decrease for objects positioned further away from the bottom membrane. It is pertinent to mention here that additional factors such as Brownian motion of particles, viscosity of liquid, diffusion constants and density of the liquid may well affect the obtained resolution thus making the overall case of predicting actual values inherently difficult. Still these calculations prove that liquid cell TEM provides a unique combination of temporal and spatial resolutions. For the case of STEM imaging the best resolution is obtained on the entrance side which is the top membrane[32]. For thicker samples STEM has a much better resolution. The resolution in this mode can be thought of as diameter of smallest nanoparticle deducible from the background noise.

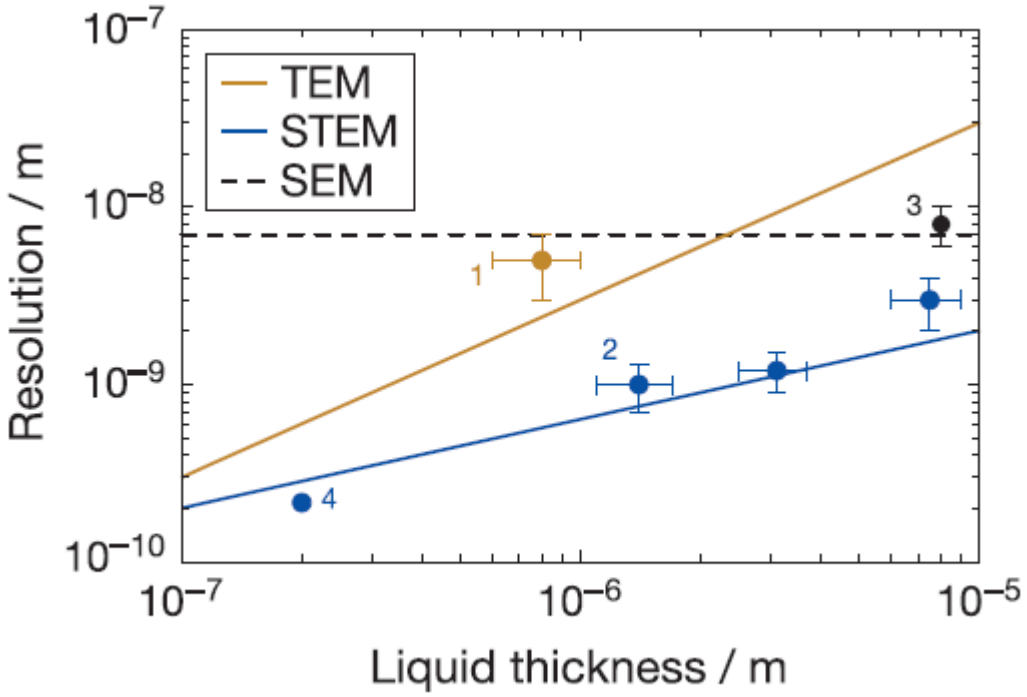

Fig 1: Resolution in liquids using different forms of electron microscopy. Image courtesy: De Jonge et al, nature nanotechnology, 2011[25].

Another advantage of SiN based setup is the capability of flow in holders utilizing this type of liquid cells. This capability is currently not available with graphene based liquid cells which can be operated in static mode only although much thinner liquid layers can be entrapped in those cells permitting much higher resolutions than SiN membrane cells[19]. The ability to use flow is an exciting new prospect for studying more complex chemical reactions where multiple reagents can be introduced within the liquid cell during experiments[33]. It also eliminates the problem of solvent depletion and formation of hydrogen bubbles which is an artifact of beam induced irradiation. Typically at high dose rates the gaseous products from the interaction of electron beam with the solvent result in formation of these bubbles[34]. Flow mitigates these effects up to a great extent. In addition to incorporating flow, electrodes can be added to the system in order to study electrochemical reactions. The additions of these remarkable capabilities have led to an exponential growth in publication of material related to liquid TEM. Figure 2A quantitatively shows this upward trend graphically.

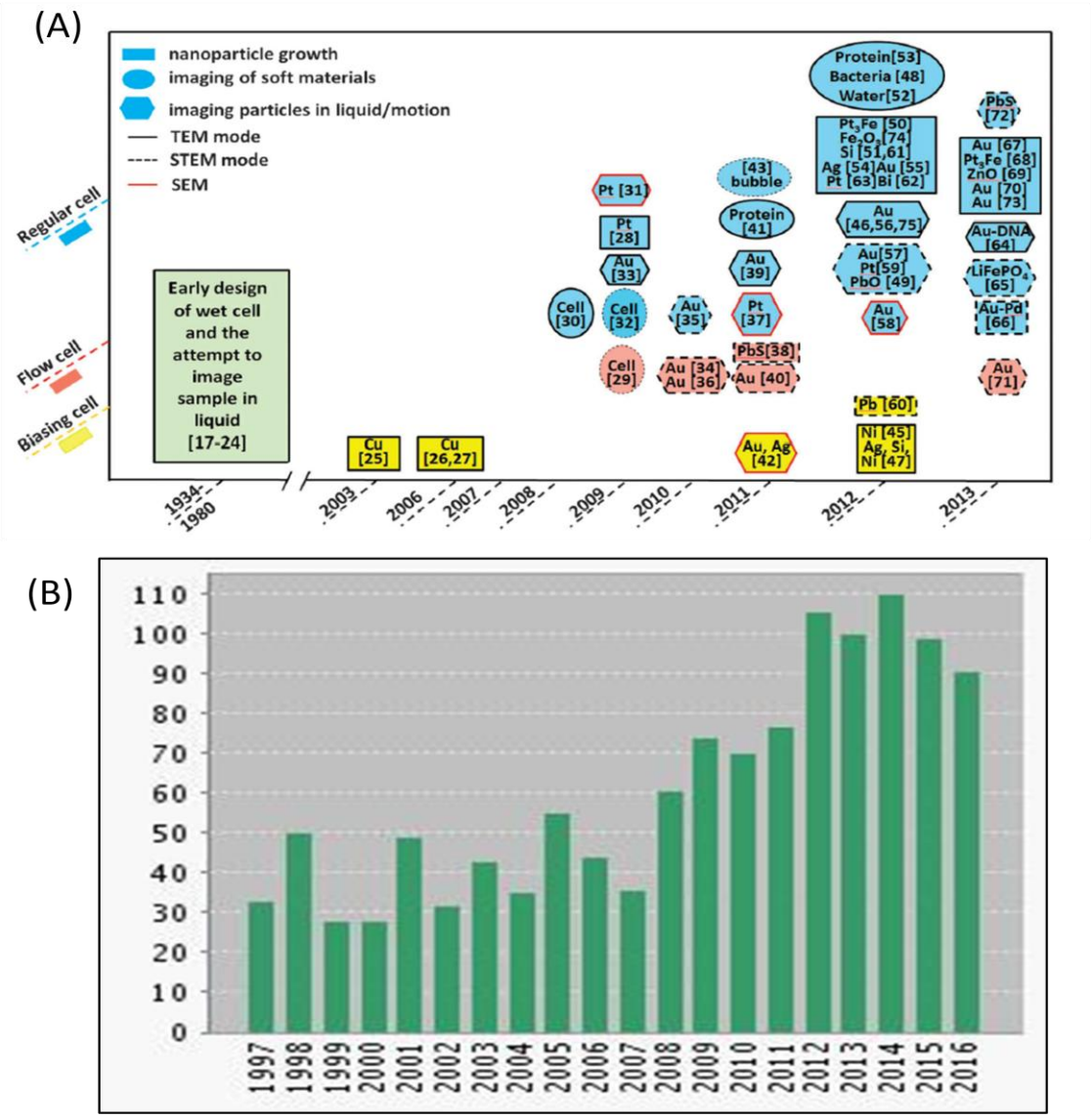

Fig 2: (A) Entire publication history of liquid electron microscopy papers upto 2013. Image courtesy: H.G Liao et al [35]. (B) More recent record of publications till 2016 (Papers incorporating "in situ" and "TEM" in their title).

As seen in this chart from 2009 onwards there is a huge growth in publications within a span of five years. This number is much greater than the number of papers appearing over the entire history of liquid TEM before 2009. Moreover bar chart in figure 2B shows a more recent extension of this publication record till 2016. Many labs nowadays are using commercial as well as customized liquid cell systems. However the success of both as already mentioned can be attributed to quantum leaps in microfabrication technology in this period. Some remarkable

insights have been made in these publications. For the purpose of clarity some of these are briefly reported in the following passages.

1.3.1 Determination of Colloidal Nanocrystal Growth Trajectories

In metallic nanoparticle systems it has been assumed that coalescence of nanoparticles leads to larger particle size distributions. To observe the role of coalescence during growth, liquid cell TEM experiments were conducted by Zheng et al[36]. They were able to observe growth trajectories of colloidal nanoparticles by means of side by side monomer attachment as well as coalescence events in same field of view. Through their observations it was found that during coalescence of nanoparticles, a recrystallization and re-orientation step is involved causing a pause in growth[36]. Thus no significant size differences were found for the two types of growth modes and monodispersity is essentially not a function of growth by means of monomer attachment. This kind of information was only possible with directly observing the growth in real time underlying the significance of this technique. Additionally a lot of studies have also focused on the origins of nanoparticle motion. For example Mueller et al[37]. in their work distinguished the pressure driven and random motion of gold nanorods within the viewing area. Other studies showed their behavior in much thicker liquids showing the Brownian motion has an impact on attainable resolution[32]. De Jonge et al[38]. conducted one such study. They observed the motion of Au nanoparticles in water under a STEM beam. It was found that the motion of nanoparticles was 3 orders of magnitude slower than that observed for Brownian motion in bulk liquids. From their experimental results they deduced that this was presumably due to the presence of highly ordered layer of liquid near the membrane causing a rapid increase in viscosity of the medium. Such kind of data is critical for nanofluidic and self assembly studies. Another interesting study by Woehl et al[39]. have recently proposed that the beam-induced ejection of metallic NPs from the SiN membrane was due to a transfer of the positive charges accumulated in the window to the NPs by contact electrification, followed by a coulombic repulsion of the positively charged NPs which activates their diffusion in the liquid. When the positive charges are released in the buffer, the NPs are attracted again by the membrane and stop diffusing.

1.3.2 Electrochemical studies

Understanding the structural and compositional changes taking place on battery electrodes is imperative for achieving more robust designs[40]. The *in-situ* capabilities of liquid TEM have already enabled researchers to make a great deal of progress. Several important studies have already appeared in last few years. Essentially a miniaturized electrochemical cell is incorporated into the sample holder having reference, working and counter electrodes. Scientists have been able to follow the morphological changes on the growth front and understand the growth instabilities which affect normal battery operations[41, 42]. Figure 3 shows the electrochemical processes taking place on anode during charge/discharge cycles. First series of images in figure 3A shows Li deposited uniformly on Pt electrode surface during charging cycle. However discharge cycle results in incomplete etching thus forming residual Li deposits. Due to these remaining deposits second charging cycle in figure 3B causes an increase in the amount of Li deposited. The growth also becomes more dendritic due to increased surface roughness of the deposits. Such kind of operando studies allows for understanding the evolution of solid electrolyte interface in real time[43].

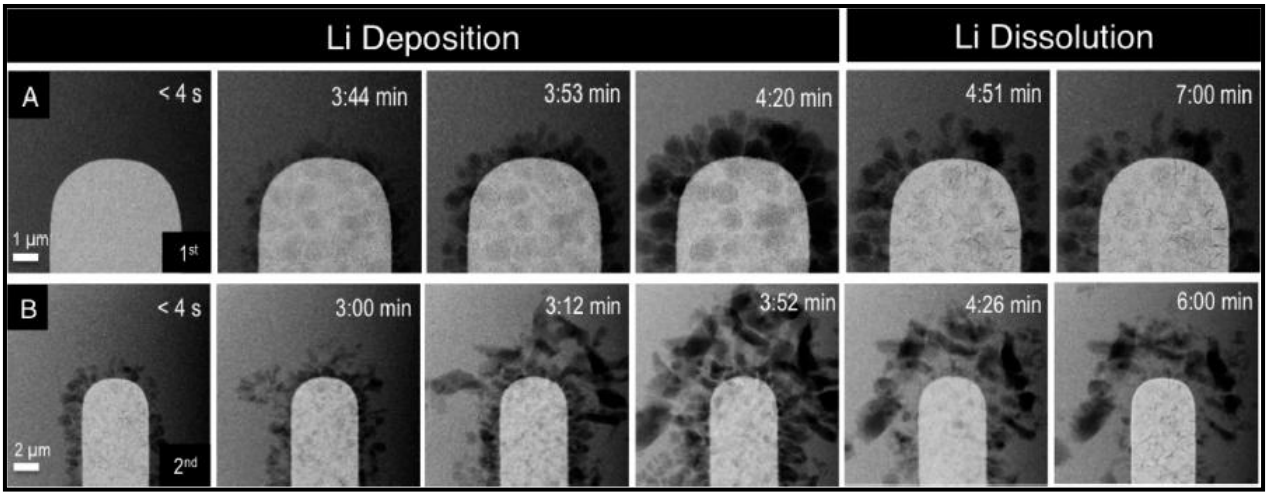

Fig 3: Deposition / dissolution cycle of lithium at Pt electrode. (A) First cycle. (B) Second cycle. Image courtesy: Mehdi et al[43] .

Optimizing the structural and chemical changes taking place during cycling operations is an area of interest and it is in this respect that liquid TEM is proving to be an indispensible tool.

Another subdomain of electrochemical studies which is of paramount importance to industry is the field of corrosion sciences. A great deal of emphasis is placed on reducing the overall impact of this ever present phenomenon which results in losses of billions of euros to the industry

annually. Life span of most structural and electronic components is usually limited by corrosion which is essentially degradation with time due to environmental factors. Even though most materials corrode however metals have higher susceptibility to corrosion phenomenon. Since corrosion is dependent upon microstructure and composition, there is a dearth of techniques that can probe the structural and chemical changes at the interface between metal and its environment. While observing nanoparticle dynamics have been a primary focus of LCTEM experiments, lesser attention until now has been paid to study corrosion dynamics at high resolutions. Fundamental challenge is in understanding localized pitting corrosion due to its stochastic nature.

Chee et al. demonstrated corrosion morphologies on Cu and Al films[44]. Figure 4A shows pits in development in a 50 nm Cu film at various growth stages. From the real time images they insinuate the fact that corrosion occurs by dissolution of individual grains of Cu. Figure 4B shows X-ray energy dispersive (XED) spectrum clearly showing dissolution of MnS due to exposure to H_2O. Dissolution of MnS in low alloy steels is linked to environmentally assisted cracking[45].

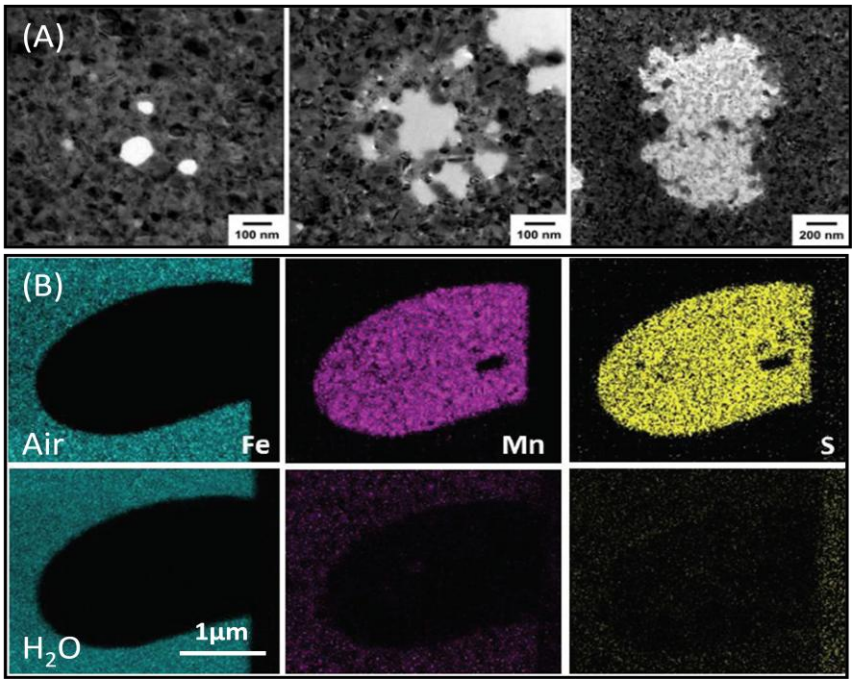

Fig 4: (A) Dynamic evolution of pits in Cu film in 6M Nacl solution after 2 hrs. Chee et al.[44] (B) Dissolution of MnS from type 304 steel after 24 hrs H_2O exposure. Schilling et al.[45]

Furthermore due to its excellent spatial resolution LCTEM is ideal for dealloying reactions that are detrimental to structural integrity of alloys. Noh et al. studied this phenomenon on Cu-Au and Ag-Au films in sulfuric acid. The authors studied microstructural evolution as a function of alloy concentration and potential[46].

Apart from these corrosion studies on thin films, recent LCTEM studies have focused on the oxidative etching of nanomaterials. The mechanisms and kinetics of dissolution of Pt and Pd nanoparticles were investigated as a function of their shape, structure and aggregation state, providing relevant insights into selective-facet etching methods[47, 48]. Interestingly, such nanoscale corrosion can also be used to solve the riddle of the degradation pathways of nanomaterials in oxidative environment, such as cellular media. The groups of D. Alloyeau and F. Gazeau[49] recently demonstrated the possibility to follow at the nanoscale, the degradation of carbon nanotubes induced by reactive oxygen species (ROS) that are produced by the radiolysis of the solvent. Through their original work combining materials and life sciences approaches, they were able to demonstrate that these *in situ* observations recapitulate in a faster way the biological pathway for CNT degradation in macrophages which also implies (ROS) induced degradation. These and other promising findings will undoubtedly lead to further robust studies on corrosion and degradation in near future.

1.3.3 Life Sciences

Until recently fluorescence microscopy and cryo electron microscopy have been the method of choice for observing functional and structural properties of biological specimens such as proteins. The former method suffers from a resolution limit of 10 nm while the later has problems related to sample preparation resulting in freezing of structures. Some innovative research has been carried out in this regard using LCTEM which offers the main advantage of dynamics imaging in native media. Whole cells (Figure 5) have been imaged using STEM in micrometers of liquid thickness and sub-5 nm NPs selectively attached to specific membrane proteins can also be detected [50, 51]. Combined with efficient labelling strategies, LCTEM is an efficient way to membrane protein distribution in wet cell which is a crucial information in cellular biology notably to understand cancer progression[52]. If it is possible to keep the cells alive in the chamber by flowing nutrients for hours, the current dose levels required for imaging, seems to be lethal for the cells[53].

This question of biological-cell viability under low-dose electron irradiation is intensively debated[54-56] and many efforts are well underway for establishing a threshold dose below which imaging live cells may be a possibility in near future. Besides, LCTEM has also been used to study the native structure of other biological specimens, such as liposomes[57], bacteria[58], viruses[59, 60] and nanometric proteins[61]. Given their interactions with the electron-beam, the possibility to visualize and to interpret biomaterials dynamics by LCTEM is still under debate.

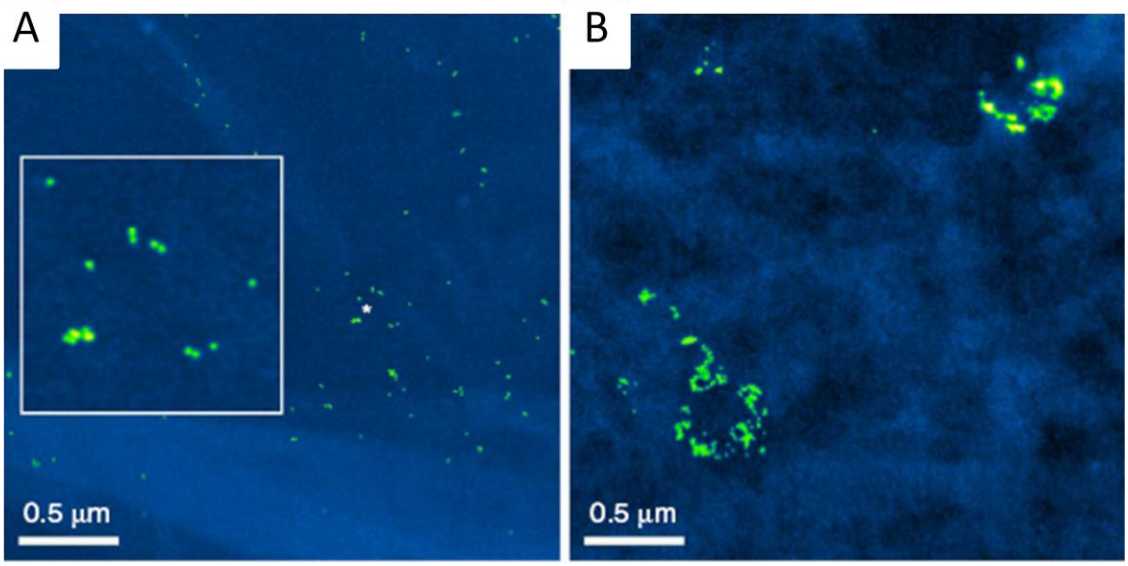

Fig 5: Liquid scanning transmission electron microscopy of whole eukaryotic cells. (A) Gold labeled epidermal growth factor receptor labels visible as yellow spots and cellular material as light blue matter over dark blue background. Inset showing monomers and dimers. (B) Image of cell showing two vesicles with internalized labels. De Jonge et al [53] .

1.3.4 Surface Functionalization and Shape Control of Nanoparticles

As already mentioned unique applications for nanocrystal require precise control over their shape and morphology. Colloidal chemists have been able to produce various non equilibrium morphologies during past decades by modifying growth environment with various types of surfactants and capping strategies[62, 63]. The complex chemistry makes it difficult to understand the mechanisms in an appropriate manner. LCTEM functions as a nanolab mimicking the conventional beaker chemistry with the advantage of simultaneously looking at growth transformations rather than looking at the end product and relying on theoretical models to predict growth mechanisms.

As shown in Figure 6, Liao et al. demonstrated the radical changes taking place on the morphologies of Pt-Fe nanocrystals[64] by changing the concentration of oleylamine. In their study nanowires formation from attachment and re-organization of nanoparticles was achieved at intermediate concentrations of the amine.

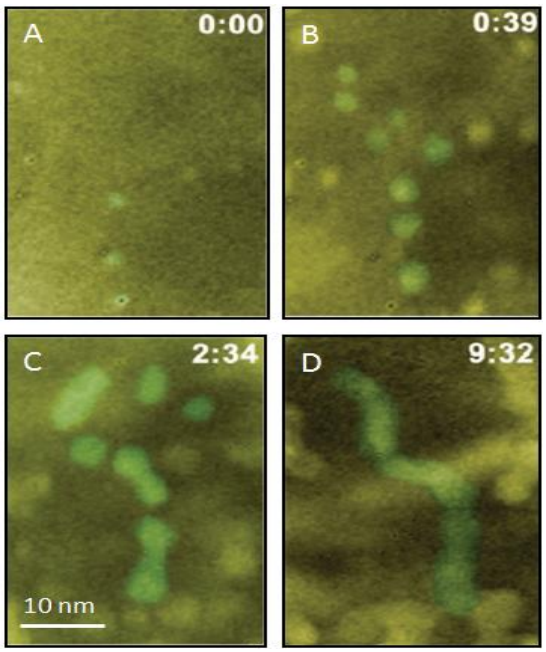

Fig 6: Growth of Pt_3Fe nanorods under exposure of electron beam. H.G Liao et al [65].

At higher concentrations however formation of nanowires was prevented by stabilization of the nanoparticles. Through this study they were able to develop a firsthand view of dipolar interactions between nanoparticles and also the role of steric hindrances between neighboring nanoparticles.

1.3.5 Direct Observation of Nanocrystal Faceting

Graphene liquid cells are devised recently for atomic resolution imaging. Directly imaging nanocrystal growth allows for visualizing structural reshaping and facet development. The liquid is essentially entrapped in the form of pockets of liquid between two graphene sheets[30] (Figure 7A). These types of liquid cells minimize the electron scattering. The only current limitation is the inability to use flow in such types of cells. To counter this problem Liao et al. devised a liquid cell with very thin SiN membranes of around 10 nm and used a direct detector to improve

sensitivity and image resolution[66]. They were able to obtain similar level of atomic resolution while studying facet development during platinum nanocube growth as shown in figure 7C.

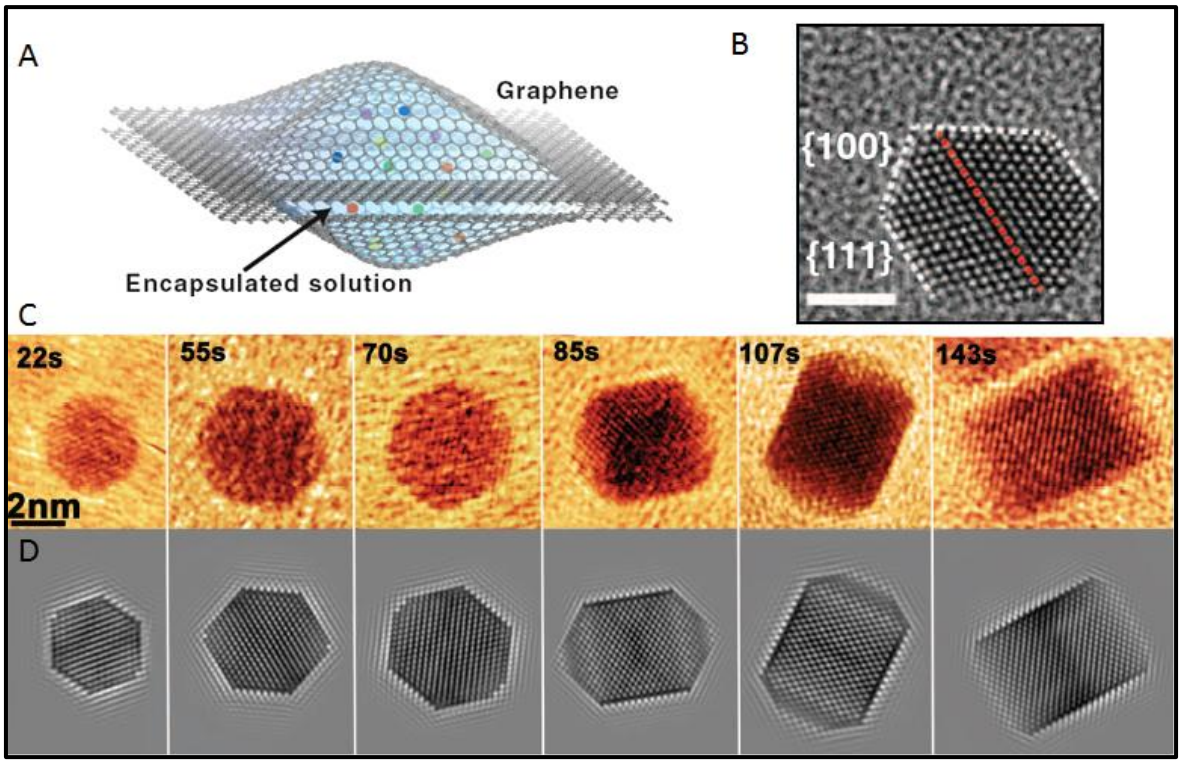

Fig 7: (A) Schematic of graphene liquid cell (B) Pt nanoparticle with twin boundary denoted by red line. Yuk et al.[30]. (C) Sequential images of Pt nanocrystal growth Liao et al. together with simulated TEM images (D)[66].

Another way devised to obtain atomic resolution in liquids is to form hydrogen bubbles which cause thin layers of liquid to be entrapped between bubbles and SiN membrane. Zhu et al[67]. have shown a highly reproducible method to tune hydrogen bubble sizes which are formed by radiolysis of water and are usually an artifact of the beam. They used this method to obtain atomic resolution images as well as motion dynamics of palladium nanoparticles.

1.3.6 Analysis of Heterostructured Nanoparticle Synthesis

As already mentioned that seed mediated growth strategy is most versatile among various nanocrystal fabrication routes therefore quite a few studies on seed mediated nanoparticle synthesis had taken place in short span of time. This route allows for one type of material to be

deposited on seeds of another type of material. Through this route composite heterostructures such as core-shell nanoparticles have successfully been formulated. Recently Sutter et al. formulated Pd@Au core-shell nanoparticles and demonstrated that the size of gold seed affected the morphology of final nanocrystal[68]. Uniform epitaxial growth on smaller gold seeds is reported in their study while in the same solution non uniform growth is observed on larger gold seeds. These observations of competing growth processes are critical for rationalizing pathways for different kinds of morphologies.

Similarly another *in-situ* TEM study was performed by Wu et al. to reveal the growth mode of Au on Pt icosahedral nanoparticles[69]. They were able to quantify the growth kinetics by first studying the deposition of gold on corners of Pt icosahedral nanoparticles then their subsequent diffusion to edges and finally layer by layer growth of gold atoms atop each other as shown in figure 8.

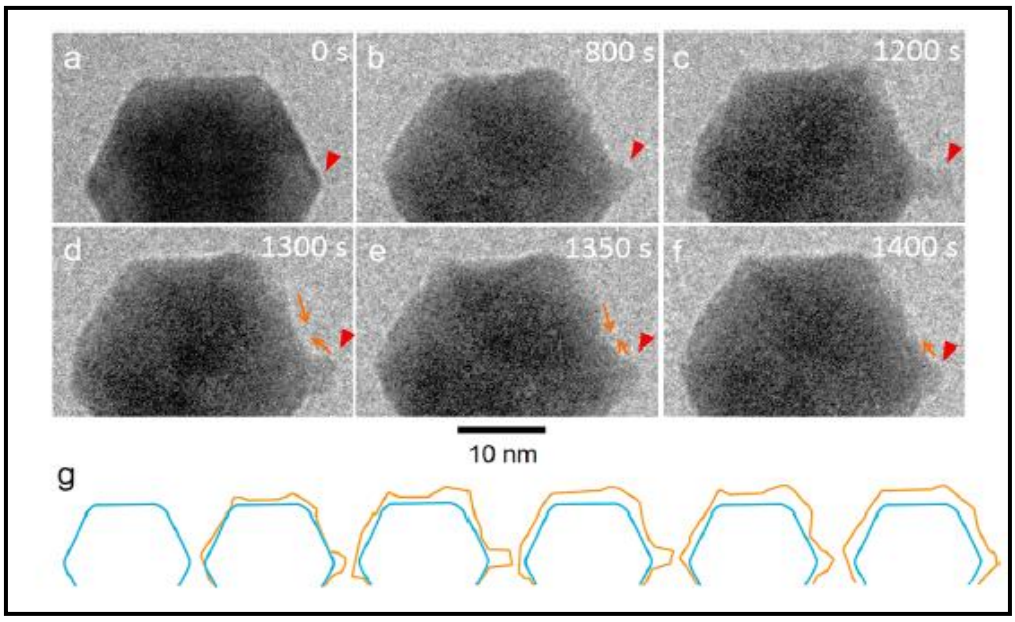

Fig 8: Morphological evolution of Pt @ Au nanoparticles. Wu et al [69] .

1.3.7 Fluid Dynamics at Nanoscale

The behavioral attributes of nanoscale processes in liquids are dependent upon nanoscopic fluid dynamics as the configurational entropies and free energies are quite different[70]. At sub nanometer resolutions LCTEM is proving to be a very useful tool for understanding boundary

layer dynamics of interfacial fluids. Simulation and experimental work in this regard has turned up valuable information.

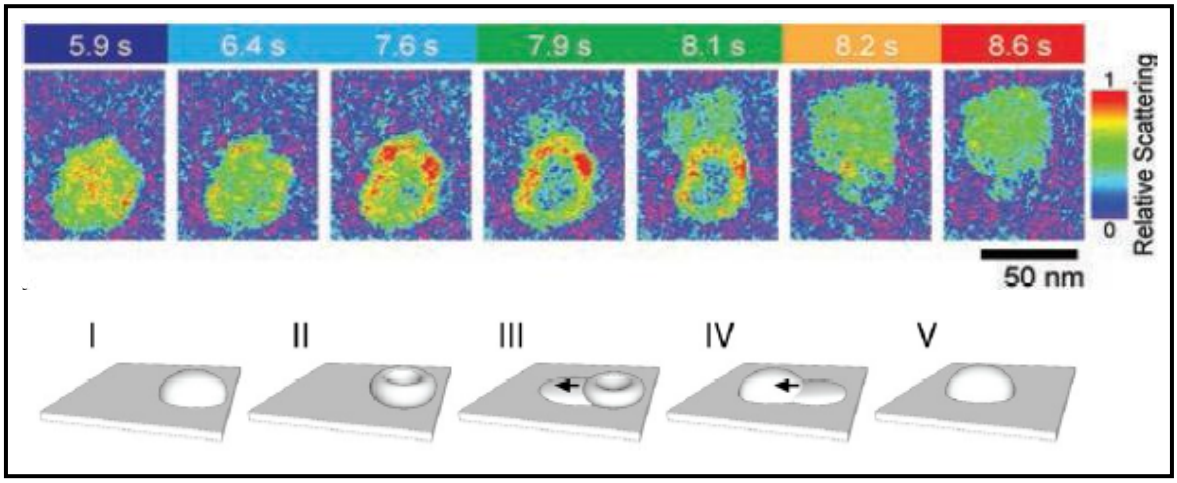

Fig 9: Stick slip translocation of nanodroplet with color coded TEM images and associate schematics of nanodroplet motion. Mirsaidov et al.[71].

Mirsaidov et al. directly studied the stick-slip translocation of water nanodroplets under an electron beam[71] described in Figure 9. It was revealed that nanodroplets formed on substrate move in discreet steps under the effect of charging by e-beam. They first form a torroidal structure of non uniform thickness followed by formation of thin wetting precursor film at the point of highest contact angle. The entire mass of water then shifts into this film causing the receding nanodroplet to shift and regain its convex appearance. The detailed study showed that slip-stick motion is caused by competition between redistribution of water due to beam charging and interfacial forces.

1.4 Growth of Nanoparticles by Radiolysis

There is a need to understand beam effects for useful interpretation of liquid cell TEM results. An electron beam interacting with the liquid results in radiolysis of the solvent. The incoming electrons excite and dislodge the orbital electrons resulting in creation of several radical species as well as aqueous electrons (e^-_{aq}). Some of these species such as e^-_{aq} are reducing in nature and actively reduce precursor ions in solution to monomers which aggregate to form nanocrystals[72]. Others such as ($OH^\bullet$) radicals are strongly oxidizing in nature. During the radiolysis of water following chemical reactions can be summarized.

$$H_2O \xrightarrow{e^- \, beam} e^-_{aq}, H_3O^+, H^\bullet, H_2, OH^\bullet, H_2O_2$$

The metal ions are readily reduced by aqueous electron (e^-_{aq}) and hydrogen radicals ($H^\bullet$) in water

$$M^n + e^-_{aq}, H^\bullet \longrightarrow M^{n-1}$$

On the contrary hydroxide radicals have been known to oxidize metals slowing the growth process.

$$M^n + OH^\bullet \longrightarrow M^{n+1}$$

Such kind of beam induced growth is somewhat similar to formation of nanocrystals by means of chemical reducing agents. Radiochemical synthesis of nanoparticles, which can be performed with other types of ionizing radiations[73] (gamma, x-rays…)[74] is also intensely studied since the production yields can be on commercial scale and radiolysis in itself is a much greener chemical synthesis route due to fewer chemical reagents. These large-scale syntheses of nanoparticles by radiolysis clearly demonstrated that the dose rate is a key parameter to control the concentration of radiolysis species and consequently to control the growth speed of nanomaterials[75]. In a similar manner, the possibility to tune the electron dose rate during LCTEM experiments provides a straightforward control of the growth speed of nanoparticles in the liquid-cell and enable the quantitative study of kinetic effects on the shape of nanoparticles. Thus, Woehl et al[72]. described two growth regimes in their work on the formation of silver nanoparticles driven by electron beam. They cited Lifshitz-Slyzov-Wagner (LSW) growth model[76] which predicts two different growth modes, reaction limited growth and diffusion limited growth. The diffusion limited growth observed for high dose rate results in formation of multiply twinned seed crystals resulting in 3D polyhedral shapes while reaction limited growth observed for low dose rate results in singly or parallel twinned nuclei that form 2D plates as seen in figure 10.

Just before this PhD thesis, the MeANS group at MPQ lab clearly demonstrated the effects of the dose rate on the growth speed and resulting shape of gold nanoparticles[77] formed in water.

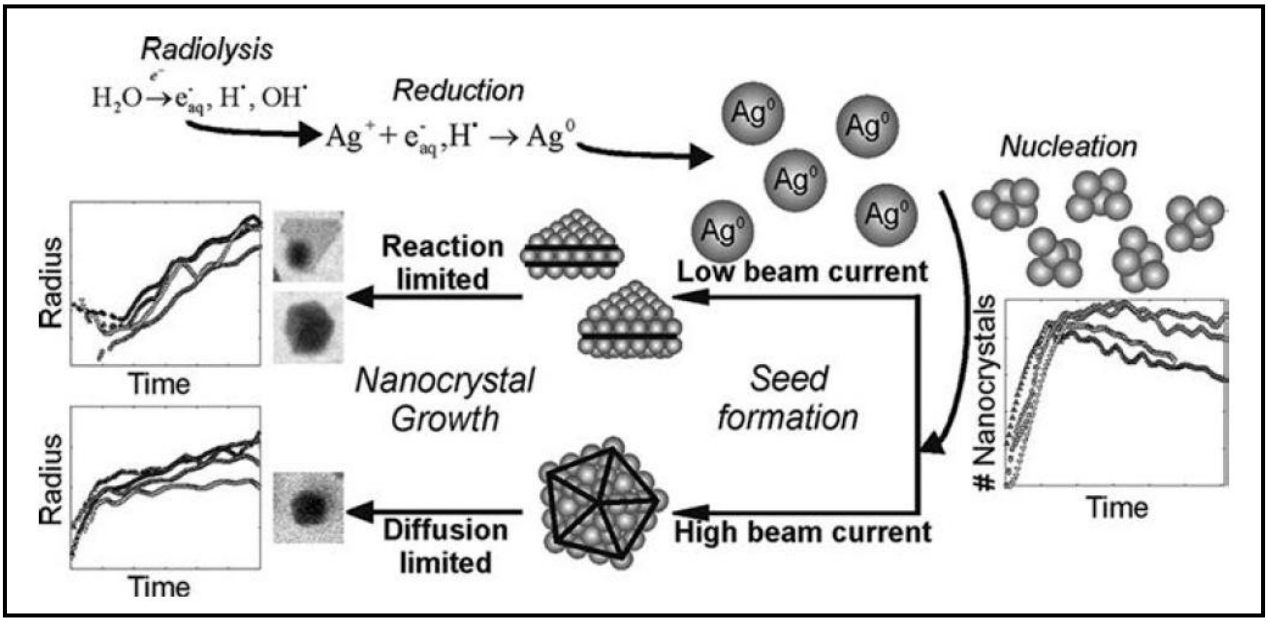

Fig 10: Radiochemical growth of Ag nanostructures as a function of electron dose. The growth radius variation as a function of time is shown on the left where it is $r \sim t^{1/3}$ for diffusion limited growth and $r \sim t^{1/2}$ for reaction limited growth. Image courtesy: Woehl et al. ACS nano, 2012 [72] .

Similarly, low growth processes (observed at low electron dose) lead to the formation of facetted nanoparticles, including nanoplates, while faster growth (observed at high electron dose) induces the formation of branched or even dendritic morphologies. By measuring the 3D volume of these nanoparticles they were able to determine the critical supply rate of gold monomers required to form faceted nanoparticles. Additionally the study provided useful insights into the role of crystal defects on the formation of nanoplates.

1.4.1 Radiation Chemistry of Liquid Environment

Control over synthesis environment is absolutely necessary for shape and size dependent functionalities of nanomaterials. There is a fundamental desire to understand and quantify electron beam and liquid interactions in order to tailor the chemical environment. As the concentration of solutes in LCTEM experiment is very low < 0.1M therefore the solvent radiation chemistry is the main deciding factor[78]. As water is the most widely used solvent for synthesis experiments therefore its radiation chemistry is well understood. A kinetic model for quantifying

water based radiolysis products based on the work of Pastina et al.[79] had been recently adapted for LCTEM by Schneider et al.[80] since the local dose rates in an electron microscope are several orders of magnitude higher than the ones used in radiation chemistry. As shown in figure 11A the temporal evolution of important radiochemically generated species is plotted. Remarkably the steady state concentrations of the species are reached within 1ms after irradiation in figure 11A. In addition to the primary products formed, there is a cascade of chemical reactions involved. For the case of water alone there are more than 70 chemical reactions that needs to be taken into account. In figure 11B we see an increase in steady state concentrations with an increase in electron dose rates. These calculations are in line with the dose-rate-dependency of the growth rate measured for both gold or silver nanoparticles[77].

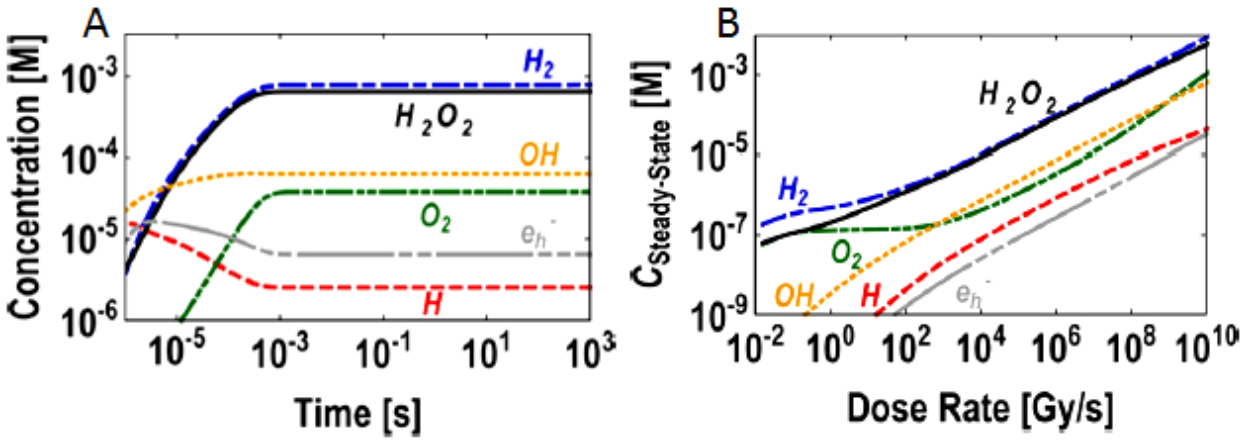

Fig 11: (A) Steady state concentrations of important radiolytic species. (B) Increase in steady state concentrations with an increase in electron dose rates. Image courtesy: Schneider et al[80].

Other useful data from this model is the interactions between different radicals. For example molecular oxygen consumes aqueous electrons (e^-_{aq}) and thus directly has an impact on the concentration of these important reducing species. Currently with regards to the absence of any direct spectroscopic techniques to quantify species concentration such models are of prime importance for evaluating and designing new experiments. However presence of membranes and interfaces can also complicate reaction kinetics as these are additional sources for secondary electrons complicating the model[81]. As different oxidizing and reducing species are produced by radiolysis of water, net reducing and oxidizing environments can be established by adding solutes. Species such as alcohols can selectively scavenge $OH^{\bullet}$ radicals while there is no effective interactions with aqueous electrons e^-_{aq} causing growth conditions favorable to growth.

On the other hand for degradation studies radical scavengers such as N_2O can be added to convert aqueous electrons e^-_{aq} into $OH^\bullet$ radicals by the following reaction regime.

$$e^-_{aq} + N_2O \longrightarrow N_2 + O^-$$

$$O^- + H_2O \longrightarrow OH^\bullet + OH^-$$

Use of organic solvents gives more flexible and broader range of chemical environments as the radiolytic products are more varied and complex. These normally include small molecules, dimeric species and even larger polymeric species. Other options where radiolytic products are extremely undesirable can make use of solvents relatively resistant to beam damage such as aromatic hydrocarbons. Abellan et al. used toluene where the G value of H_2 (primary reducing specie) is 0.14 molecules/100 eV as compared to G value of aqueous electrons e^-_{aq} (2.7 molecules/100 eV) in water. The only problem is the lack of radiation data such as G values and reaction rate constants for many organic solvent systems[82].

Furthermore electron beam has been shown to change pH of the solution which affects growth conditions. The reaction equilibria and reaction pathways of species formed by radiolysis depend on pH of the solution. It is shown in a recent study on gold nanoparticles that based on solution chemistry i.e. pH and chloride ion activity, the nanoparticles change their behaviour under the electron beam by either merging, dissolving and remaining stable[83].

In a nutshell it can be said that complicated interplay between solution composition and radiolysis products makes it challenging to directly compare experimental results with these simulations however it gives a good qualitative comparison which can be very useful in terms of understanding and controlling the beam artefacts.

1.5 Main Aspects of This Work

- Distinguishing kinetic and thermodynamic effects on the growth of nanoparticles.
- Studying the effects of electron irradiation, seed crystal morphology and surface functionalization on the final shape of gold nanoparticles.
- Provide a better understanding of beam driven redox reactions.

1.6 Outline of Thesis

Chapter 2: TEM techniques and general methodology of experiments are described in this chapter.

The three next chapters are extended versions of the three papers published during this PhD thesis.

Chapter 3: **Growth of dendritic nanostructures.** We have exploited liquid-cell TEM to study the effects of the electron-irradiation history on the radiochemical growth of dendritic Au nanostructures. Besides the well-established direct link between the dose rate and the growth rate of the nanostructures, we demonstrate that the cumulative dose in the irradiated area can induce important transitions in the growth mode of the nanostructures. By comparing *in situ* observations with an extended diffusion-limited aggregation model, we reveal how the shape of the nanostructures are severely affected by the local lack of metal precursors and the resulting restricted accessibility of gold atoms to the nanostructures.

[Nabeel Ahmad, Yann Le Bouar, Christian Ricolleau, and Damien Alloyeau, "**Growth of dendritic nanostructures by liquid-cell transmission electron microscopy: a reflection of the electron-irradiation history**" Advanced Structural and Chemical Imaging 2, no. 1 (2017): 9]

In the introduction of this chapter, we also describe the measurements of liquid thickness in 150 nm spacer liquid-cell performed by EFTEM.

Chapter 4: **Synthesis of symmetric gold nanostars.** We report an unprecedented *in situ* study focused on the seed-mediated synthesis of symmetric gold nanostars performed by radiolysis in methanol. We take advantage of the spatial and temporal resolutions of liquid-cell transmission electron microscopy to unravel the key effects of the growth speed, seed-crystal morphology, and dimethylamine functionalization on the formation mechanisms, shape, and stability of stelatted nanostructures enclosed by high-index facets.

[Nabeel Ahmad, Guillaume Wang, Jaysen Nelayah, Christian Ricolleau, Damien Alloyeau. "**Exploring the Formation of Symmetric Gold Nanostars by Liquid-Cell Transmission Electron Microscopy**." Nano Letters (2017)]

Chapter 5: **Driving Reversible Redox Reactions at Solid / Liquid Interfaces with the Electron Beam of a Transmission Electron Microscope** We show that the electron beam can be used to drive reversible deposition / dissolution cycles of copper shells over gold nanoparticles in methanol. Besides revealing the influence of irreversible processes on the kinetic of growth/etching cycles, this study of nanostructure behavior as a function of the dose rate highlights the possibility to switch the oxidizing or reducing nature of liquid environment only with the electron beam. The chemical and electronic processes possibly involved in these tunable redox reactions are qualitatively discussed together with their possible impacts on electrochemical LCTEM experiments.

[Nabeel Ahmad, Guillaume Wang, Jaysen Nelayah, Christian Ricolleau, Damien Alloyeau. "**Driving reversible redox reactions at solid–liquid interfaces with the electron beam of a transmission electron microscope**." Journal of Microscopy (2017)]

Chapter 6: Conclusion and Future Perspectives.

References

1. Cortie, M. B. *Gold Bulletin* **2004,** 37, (1), 12-19.
2. Valden, M.; Lai, X.; Goodman, D. W. *science* **1998,** 281, (5383), 1647-1650.
3. Xia, Y.; Xiong, Y.; Lim, B.; Skrabalak, S. E. *Angewandte Chemie International Edition* **2009,** 48, (1), 60-103.
4. Zhang, H.; Jin, M.; Xiong, Y.; Lim, B.; Xia, Y. *Accounts of chemical research* **2012,** 46, (8), 1783-1794.
5. Grzelczak, M.; Pérez-Juste, J.; Mulvaney, P.; Liz-Marzán, L. M. *Chemical Society Reviews* **2008,** 37, (9), 1783-1791.
6. Kawamura, G.; Nogami, M.; Matsuda, A. *Journal of Nanomaterials* **2013,** 2013, 2.
7. Sun, Y.; Xia, Y. *Science* **2002,** 298, (5601), 2176-2179.
8. Canbek, Z. C.; Cortes-Huerto, R.; Testard, F.; Spalla, O.; Moldovan, S.; Ersen, O.; Wisnet, A.; Wang, G.; Goniakowski, J.; Noguera, C. *Crystal Growth & Design* **2015,** 15, (8), 3637-3644.
9. Xiong, Y.; Xia, Y. *Advanced Materials* **2007,** 19, (20), 3385-3391.
10. Wiley, B. J.; Xiong, Y.; Li, Z.-Y.; Yin, Y.; Xia, Y. *Nano letters* **2006,** 6, (4), 765-768.
11. Wiley, B. J.; Chen, Y.; McLellan, J. M.; Xiong, Y.; Li, Z.-Y.; Ginger, D.; Xia, Y. *Nano letters* **2007,** 7, (4), 1032-1036.
12. Tao, A. R.; Habas, S.; Yang, P. *small* **2008,** 4, (3), 310-325.
13. Sun, Y.; Mayers, B.; Herricks, T.; Xia, Y. *Nano letters* **2003,** 3, (7), 955-960.
14. Wiley, B.; Herricks, T.; Sun, Y.; Xia, Y. *Nano Letters* **2004,** 4, (9), 1733-1739.
15. Mulvihill, M. J.; Ling, X. Y.; Henzie, J.; Yang, P. *Journal of the American Chemical Society* **2009,** 132, (1), 268-274.
16. Wu, J.; Yang, H. *Accounts of chemical research* **2013,** 46, (8), 1848-1857.
17. Lartigue, L.; Alloyeau, D.; Kolosnjaj-Tabi, J.; Javed, Y.; Guardia, P.; Riedinger, A.; Péchoux, C.; Pellegrino, T.; Wilhelm, C.; Gazeau, F. *Acs Nano* **2013,** 7, (5), 3939-3952.
18. Ngo, T.; Yang, H. *The journal of physical chemistry letters* **2015,** 6, (24), 5051-5061.
19. Liao, H.-G.; Zheng, H. *Annual review of physical chemistry* **2016,** 67, 719-747.
20. Abécassis, B.; Testard, F.; Spalla, O.; Barboux, P. *Nano letters* **2007,** 7, (6), 1723-1727.
21. Steinfeldt, N. *Langmuir* **2012,** 28, (36), 13072-13079.
22. Hubert, F.; Testard, F.; Thill, A.; Kong, Q.; Tache, O.; Spalla, O. *Crystal Growth & Design* **2012,** 12, (3), 1548-1555.
23. Lim, J.; Li, Y.; Alsem, D. H.; So, H.; Lee, S. C.; Bai, P.; Cogswell, D. A.; Liu, X.; Jin, N.; Yu, Y.-s. *Science* **2016,** 353, (6299), 566-571.
24. Simm, A. O.; Ji, X.; Banks, C. E.; Hyde, M. E.; Compton, R. G. *ChemPhysChem* **2006,** 7, (3), 704-709.
25. De Jonge, N.; Ross, F. M. *Nature nanotechnology* **2011,** 6, (11), 695-704.
26. Abrams, I.; McBain, J. *Journal of Applied Physics* **1944,** 15, (8), 607-609.
27. Giorgio, S.; Sao Joao, S.; Nitsche, S.; Chaudanson, D.; Sitja, G.; Henry, C. *Ultramicroscopy* **2006,** 106, (6), 503-507.
28. Sugi, H.; Akimoto, T.; Sutoh, K.; Chaen, S.; Oishi, N.; Suzuki, S. *Proceedings of the National Academy of Sciences* **1997,** 94, (9), 4378-4382.
29. Mohanty, N.; Fahrenholtz, M.; Nagaraja, A.; Boyle, D.; Berry, V. *Nano letters* **2011,** 11, (3), 1270-1275.
30. Yuk, J. M.; Park, J.; Ercius, P.; Kim, K.; Hellebusch, D. J.; Crommie, M. F.; Lee, J. Y.; Zettl, A.; Alivisatos, A. P. *Science* **2012,** 336, (6077), 61-64.
31. Hawkes, P. W., *Advances in Imaging and Electron Physics: Time Resolved Electron Diffraction: For Chemistry, Biology And Material Science*. Academic Press: 2014; Vol. 184.

32. de Jonge, N.; Poirier-Demers, N.; Demers, H.; Peckys, D. B.; Drouin, D. *Ultramicroscopy* **2010,** 110, (9), 1114-1119.
33. Klein, K. L.; Anderson, I. M.; De Jonge, N. *Journal of microscopy* **2011,** 242, (2), 117-123.
34. Grogan, J. M.; Schneider, N. M.; Ross, F. M.; Bau, H. H. *Nano letters* **2013,** 14, (1), 359-364.
35. Liao, H.-G.; Niu, K.; Zheng, H. *Chemical Communications* **2013,** 49, (100), 11720-11727.
36. Zheng, H.; Smith, R. K.; Jun, Y.-w.; Kisielowski, C.; Dahmen, U.; Alivisatos, A. P. *Science* **2009,** 324, (5932), 1309-1312.
37. Mueller, C.; Harb, M.; Dwyer, J.; Miller, R. D. *The Journal of Physical Chemistry Letters* **2013,** 4, (14), 2339-2347.
38. Verch, A.; Pfaff, M.; de Jonge, N. *Langmuir* **2015,** 31, (25), 6956-6964.
39. Woehl, T. J.; Prozorov, T. *The Journal of Physical Chemistry C* **2015,** 119, (36), 21261-21269.
40. Ross, F. M. *Science* **2015,** 350, (6267), aaa9886.
41. Leenheer, A. J.; Sullivan, J. P.; Shaw, M. J.; Harris, C. T. *Journal of Microelectromechanical Systems* **2015,** 24, (4), 1061-1068.
42. White, E. R.; Singer, S. B.; Augustyn, V.; Hubbard, W. A.; Mecklenburg, M.; Dunn, B.; Regan, B. C. *ACS nano* **2012,** 6, (7), 6308-6317.
43. Mehdi, B. L.; Qian, J.; Nasybulin, E.; Park, C.; Welch, D. A.; Faller, R.; Mehta, H.; Henderson, W. A.; Xu, W.; Wang, C. M. *Nano letters* **2015,** 15, (3), 2168-2173.
44. Chee, S. W.; Pratt, S. H.; Hattar, K.; Duquette, D.; Ross, F. M.; Hull, R. *Chemical Communications* **2015,** 51, (1), 168-171.
45. Schilling, S.; Janssen, A.; Zhong, X.; Zaluzec, N.; Burke, M. *Microscopy and Microanalysis* **2015,** 21, (S3), 1291-1292.
46. Noh, K. W.; Tai, K.; Mao, S.; Dillon, S. J. *Advanced Engineering Materials* **2015,** 17, (2), 157-161.
47. Jiang, Y.; Zhu, G.; Lin, F.; Zhang, H.; Jin, C.; Yuan, J.; Yang, D.; Zhang, Z. *Nano letters* **2014,** 14, (7), 3761-3765.
48. Wu, J.; Gao, W.; Yang, H.; Zuo, J.-M. *ACS nano* **2017,** 11, (2), 1696-1703.
49. Elgrabli, D.; Dachraoui, W.; Ménard-Moyon, C. c.; Liu, X. J.; Bégin, D.; Bégin-Colin, S.; Bianco, A.; Gazeau, F.; Alloyeau, D. *ACS nano* **2015,** 9, (10), 10113-10124.
50. De Jonge, N.; Peckys, D. B.; Kremers, G.; Piston, D. *Proceedings of the National Academy of Sciences* **2009,** 106, (7), 2159-2164.
51. Peckys, D. B.; de Jonge, N. *Nano letters* **2011,** 11, (4), 1733-1738.
52. Peckys, D. B.; Korf, U.; de Jonge, N. *Science advances* **2015,** 1, (6), e1500165.
53. Peckys, D. B.; De Jonge, N. *Microscopy and microanalysis* **2014,** 20, (02), 346-365.
54. Kennedy, E.; Nelson, E. M.; Tanaka, T.; Damiano, J.; Timp, G. *ACS nano* **2016,** 10, (2), 2669-2677.
55. de Jonge, N.; Peckys, D. B. *ACS nano* **2016,** 10, (10), 9061-9063.
56. Kennedy, E.; Nelson, E. M.; Damiano, J.; Timp, G. *ACS nano* **2017,** 11, (1), 3-7.
57. Hoppe, S. M.; Sasaki, D. Y.; Kinghorn, A. N.; Hattar, K. *Langmuir* **2013,** 29, (32), 9958-9961.
58. Woehl, T. J.; Kashyap, S.; Firlar, E.; Perez-Gonzalez, T.; Faivre, D.; Trubitsyn, D.; Bazylinski, D. A.; Prozorov, T. *Scientific reports* **2014,** 4.
59. Varano, A. C.; Rahimi, A.; Dukes, M. J.; Poelzing, S.; McDonald, S. M.; Kelly, D. F. *Chemical Communications* **2015,** 51, (90), 16176-16179.
60. Park, J.; Park, H.; Ercius, P.; Pegoraro, A. F.; Xu, C.; Kim, J. W.; Han, S. H.; Weitz, D. A. *Nano letters* **2015,** 15, (7), 4737-4744.
61. Wang, C.; Qiao, Q.; Shokuhfar, T.; Klie, R. F. *Advanced Materials* **2014,** 26, (21), 3410-3414.
62. Milliron, D. J.; Hughes, S. M.; Cui, Y.; Manna, L.; Li, J.; Wang, L.-W.; Alivisatos, A. P. *Nature* **2004,** 430, (6996), 190-195.
63. Tian, N.; Zhou, Z.-Y.; Sun, S.-G.; Ding, Y.; Wang, Z. L. *science* **2007,** 316, (5825), 732-735.
64. Liao, H.-G.; Zheng, H. *Journal of the American Chemical Society* **2013,** 135, (13), 5038-5043.
65. Liao, H.-G.; Cui, L.; Whitelam, S.; Zheng, H. *science* **2012,** 336, (6084), 1011-1014.

66. Liao, H.-G.; Zherebetskyy, D.; Xin, H.; Czarnik, C.; Ercius, P.; Elmlund, H.; Pan, M.; Wang, L.-W.; Zheng, H. *Science* **2014,** 345, (6199), 916-919.
67. Zhu, G.; Jiang, Y.; Huang, W.; Zhang, H.; Lin, F.; Jin, C. *Chemical Communications* **2013,** 49, (93), 10944-10946.
68. Jungjohann, K.; Bliznakov, S.; Sutter, P.; Stach, E.; Sutter, E. *Nano letters* **2013,** 13, (6), 2964-2970.
69. Wu, J.; Gao, W.; Wen, J.; Miller, D. J.; Lu, P.; Zuo, J.-M.; Yang, H. *Nano letters* **2015,** 15, (4), 2711-2715.
70. Mirsaidov, U.; Matsudaira, P., Nanoscale Water Imaged by In Situ TEM. In *Liquid Cell Electron Microscopy*, Ross, F. M., Ed. Cambridge University Press: Cambridge, 2016; pp 258-275.
71. Mirsaidov, U. M.; Zheng, H.; Bhattacharya, D.; Casana, Y.; Matsudaira, P. *Proceedings of the National Academy of Sciences* **2012,** 109, (19), 7187-7190.
72. Woehl, T. J.; Evans, J. E.; Arslan, I.; Ristenpart, W. D.; Browning, N. D. *Acs Nano* **2012,** 6, (10), 8599-8610.
73. Abidi, W.; Selvakannan, P.; Guillet, Y.; Lampre, I.; Beaunier, P.; Pansu, B.; Palpant, B.; Remita, H. *The Journal of Physical Chemistry C* **2010,** 114, (35), 14794-14803.
74. Abécassis, B.; Testard, F.; Kong, Q.; Francois, B.; Spalla, O. *Langmuir* **2010,** 26, (17), 13847-13854.
75. Treguer, M.; de Cointet, C.; Remita, H.; Khatouri, J.; Mostafavi, M.; Amblard, J.; Belloni, J.; De Keyzer, R. *The Journal of Physical Chemistry B* **1998,** 102, (22), 4310-4321.
76. Lifshitz, I. M.; Slyozov, V. V. *Journal of physics and chemistry of solids* **1961,** 19, (1-2), 35-50.
77. Alloyeau, D.; Dachraoui, W.; Javed, Y.; Belkahla, H.; Wang, G.; Lecoq, H. l. n.; Ammar, S.; Ersen, O.; Wisnet, A.; Gazeau, F. *Nano letters* **2015,** 15, (4), 2574-2581.
78. Buxton, G. V.; Mulazzani, Q. G. *Electron transfer in chemistry* **2001**, 503-557.
79. Pastina, B.; LaVerne, J. A. *The Journal of Physical Chemistry A* **2001,** 105, (40), 9316-9322.
80. Schneider, N. M.; Norton, M. M.; Mendel, B. J.; Grogan, J. M.; Ross, F. M.; Bau, H. H. *The Journal of Physical Chemistry C* **2014,** 118, (38), 22373-22382.
81. Abellan, P.; Parent, L. R.; Al Hasan, N.; Park, C.; Arslan, I.; Karim, A. M.; Evans, J. E.; Browning, N. D. *Langmuir* **2016,** 32, (6), 1468-1477.
82. Woehl, T.; Abellan, P. *Journal of microscopy* **2017,** 265, (2), 135-147.
83. áde Jonge, N. *Chemical Communications* **2015,** 51, (91), 16393-16396.

Chapter 2

Methodology

2.1 Brief History of Transmission Electron Microscopy (TEM)

Transmission electron microscopy techniques lie at the forefront of characterization of materials and nanoscale processes. Ernst Ruska and Max Knoll have been credited for making the first operational electron microscope in 1932. This incidentally marked the start of an era whereby the science community was for the very first time able to surpass the natural barrier to higher resolution imposed by limitations of natural light.

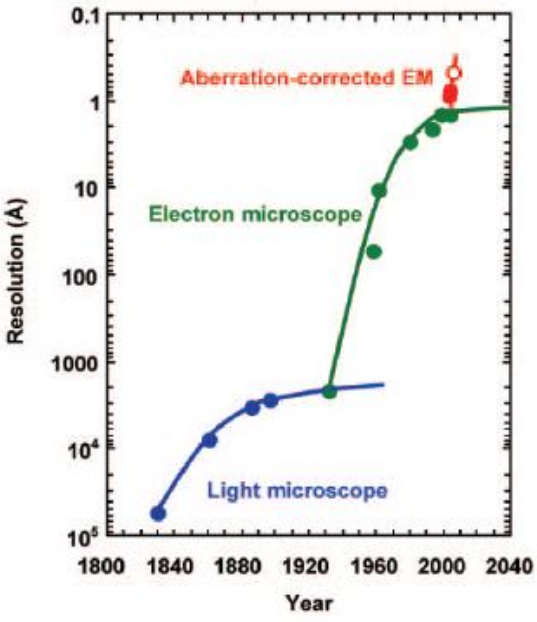

Fig 1: Improvement in resolution of microscopes over a period of time. Open red circle is the predicted resolution for fifth order aberration correctors in development. (Adapted from H.Rose et al.[1])

One of the earliest goals was to attain atomic resolution. This was barely possible in the late 1930's. Increasing the acceleration voltage of the electron beam and improvement in lens design

over the years helped realize this critical goal. The plot in figure 1 demonstrates the remarkable improvement in resolution over a period of time for light and electron microscopes[1, 2]. The attainment of high resolution was achieved initially with development of Ultra High Voltage (UHV) TEM's upto 3MeV's, however this created the problem of electron irradiation damage to specimens. Improvements in electron gun design lead to further improvement in resolution. However the ultimate improvement came with the development of spherical aberration correctors exactly 50 years after the first operation of a TEM device[3]. This era is depicted by red bump at the end of resolution profile in figure 1. This made the instrument highly practical and cost effective as well as enabled the imaging of soft materials at relatively low acceleration voltages. Over the span of several decades quite a few available instruments are currently able to achieve sub-angstrom resolutions.

2.2 Electron-Matter Interactions

Electrons are ionizing radiations. An incoming electron beam accelerated in a TEM column interacts with the electron shells and nuclei of irradiated matter. Electrons are strongly absorbed by matter as electron-matter interactions are about 10^4 to 10^5 times higher as compared to X-ray and neutrons interaction with matter[4, 5].

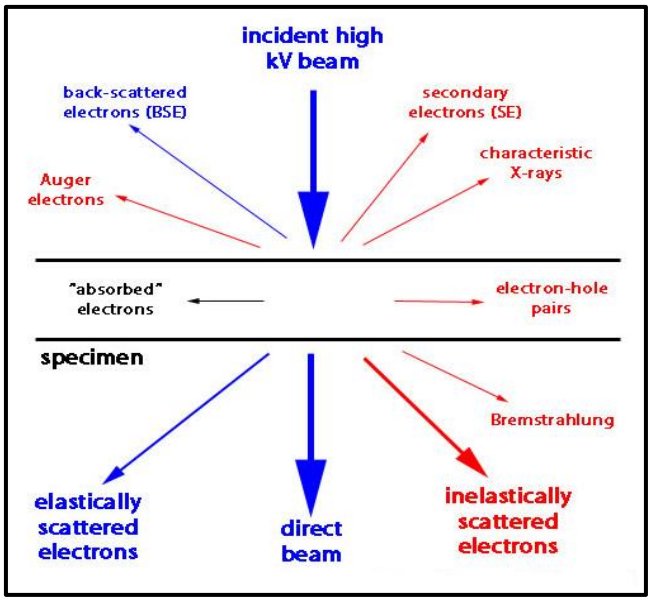

Fig 2: Generation of signals through the specimen surface by the impact of electron beam. Image courtesy: William & Carter (1996)[8].

Due to this aspect of these interactions electrons have a low penetrating power and sample requirements are skewed towards very thin samples. Electron-matter interactions are subdivided into two categories i.e. elastic scattering and inelastic scattering. Figure 2 shows a schematic depicting various kinds of signals generated when an electron probe strikes specimen surface.

2.2.1 Elastic Scattering and Electron Diffraction

An incoming electron from the primary electron beam can be scattered or remain unscattered (i.e. remain parallel to primary beam) upon interacting with the specimen. If the scattered electron does not lose any kinetic energy then the scattering is classified as elastic in nature. The driving force behind these elastic scattering are columbic interactions between beam electrons and atoms of specimen. In a crystalline material, the elastic scattering results in strong interference patterns giving rise to diffraction patterns (DP's). This phenomenon is defined as Bragg's diffraction. The angle between primary beam and scattered beam is $\mathbf{2\theta_B}$, where $\mathbf{\theta_B}$ is the Bragg angle. The equation $\boldsymbol{2dsin\theta_B = n\lambda}$ relates the angle $2\theta_B$ between a Bragg diffraction spot and the incident beam to lattice spacing **d** and the wavelength **λ**. According to kinematical theory of electron diffraction, the amplitude of Bragg diffracted wave is small relative to primary beam. This is true for extremely thin specimens but the actual samples are much thicker and diffraction is explained in terms of dynamical theory. According to this theory, multiple scattering is imminent for thick samples, thus simplified kinematical or *two-beam* theory is no more sufficient to understand diffraction processes[6, 7]. Usually more than 20 diffracted beams are to be used for properly explaining the observed phenomenon. It is necessary to compare the diffraction results with computer generated simulation to correctly assess the crystallographic information.

2.2.2 Inelastic Scattering and X-ray Emission

Most of the signals generated for Analytical Electron Microscopy (AEM) are through inelastic scattering. When an electron beam strikes a cluster of atoms, it is able to remove tightly bound inner-shell electrons from the nucleus. In addition to this a wide variety of resultant signals are generated which can be used for various spectroscopic analyses in conjunction with imaging the material at high resolution. These signals are used typically for analyses such as energy dispersive X-ray spectroscopy (EDX) and electron energy loss spectroscopy (EELS). By

utilizing these techniques chemical mapping of the material can be done. Modern instruments are well designed to produce small probes to localize these signals[8].

A whole lot of information can be generated from electron energy losses. The total energies and momentum of colliding particles is conserved but the electron excitations of specimen atoms are stimulated at the expense of incident beam energy losses ΔE. In EELS this loss in energy (ΔE) is used to create an energy loss spectrum for identifying chemical elements and bonding states. The low loss region of EELS spectrum is an eye catching feature of this technique[9].

Another important analytical signal obtained in an electron microscope is X-rays. Basically when an incoming primary electron from the electron beam knocks out a core shell electron it leaves a vacancy. This is quickly filled by an electron from the outer shells. By doing so quanta of energy or an X-photon is released with an energy equivalent to the differences in the energies between the two levels. Two types of these electromagnetic radiations are present namely bremsstrahlung X-rays and characteristic X-rays. From materials characterization point of view former are not very useful but the characteristic X-ray peaks are utilized for localized chemical composition analysis as well as quantification of a particular element within the specimen. In the TEM this is usually done by measuring the energy and intensity of these X-rays[8].

2.2.3 Beam Irradiation Damage

An electron microscope focuses tremendous amount of electron energy/probe current into a small area of specimen. This could cause damage to the specimen due to overheating resulting in change in crystal structure or properties of various materials. Knock-on damage can also induce point defects such as vacancies in most materials. As higher resolution normally requires high acceleration voltages, the problem exacerbates. The advent of aberration correctors and field emission guns resulting in finer probe sizes also increases beam damage. The problem of beam induced damage also depends upon the type of material investigated. Poorly conducting specimens such as biological samples and carbon based materials are much more sensitive than compared to inorganic materials hence requiring the use of low electron doses[10, 11]. In the case of liquid samples investigating inorganic nanomaterial behavior, this knock-on damage is however not a big issue since the thermal conductivity of water is very high. Studies on water based samples have shown that this only results in few degrees rise in water temperature[12]. Additionally if the experiment is conducted in dynamic flow mode the generated heat is effectively dissipated.

However liquid samples are also susceptible to radiolysis or ionization induced damage. Interestingly radiolytic damage is somewhat reduced at high accelerating voltages since the cross-section for inelastic scattering responsible for ionization events is minimized[13]. Both types of damages are an area of concern for beam sensitive materials.

2.3 TEM Imaging Techniques Used for LCTEM Experiments

Liquid cell TEM experiments were performed on a JEOL ARM 200F microscope installed at University Paris Diderot. The microscope operates across voltage ranging from 80-200KV and is equipped with a CEOS hexapole type spherical aberration (C_s) image corrector. The combination of a Cold FEG electron source coupled with the aberration corrector gives it a point resolution of 0.075 nm at 200kV. Additionally the integration of an extremely fast camera operating at 25 fps at full 4Kx4K resolution formulates an ideal environment to carry out in-situ dynamical studies. Following experimental modes were used for all LCTEM experiments.

2.3.1 Conventional TEM Imaging

In a basic TEM an image is formed due to contrast arising out of interaction of the electron beam with the specimen. As the beam passes through a specimen it results in a change of amplitude and phase of the electron wave. This gives rise to image contrast which can be further categorized into amplitude contrast and phase contrast. Both types of contrast are usually present in an image but one tends to dominate the other under certain conditions. The contrast in an image is actually the difference in intensities between adjacent areas denoted by the following equation[8]

$$C = \frac{(I2-I1)}{I2} = \frac{\Delta I}{I2}$$

Amplitude contrast can be classified as mass-thickness contrast and diffraction contrast. This kind of contrast is observable in bright-field (BF) and dark-field (DF) images. BF images are acquired by selecting the unscattered or weakly scattered beam while eliminating the high angle scatterings with the aid of objective aperture resulting in appearance of nanoparticles or thicker areas as dark and thin areas or amorphous carbon as bright[14]. By adjusting the position of the objective aperture the contrast can be reversed by collecting the scattered electrons only. In DF imaging the NPs on a carbon grid appear as bright spots. Figure 3 shows the schematic setup of BF and DF modes. It is pertinent here to mention that both kinds of contrasts exist in TEM

images as well as STEM images. Figure 3 also shows the contrast reversal created in the images. The nanoparticles in A are darker than the support in bright-field when unscattered beam is part of image. Upon removing the unscattered beam from the image and selecting the scattered beam marked by red circle in B we form a dark-field image.

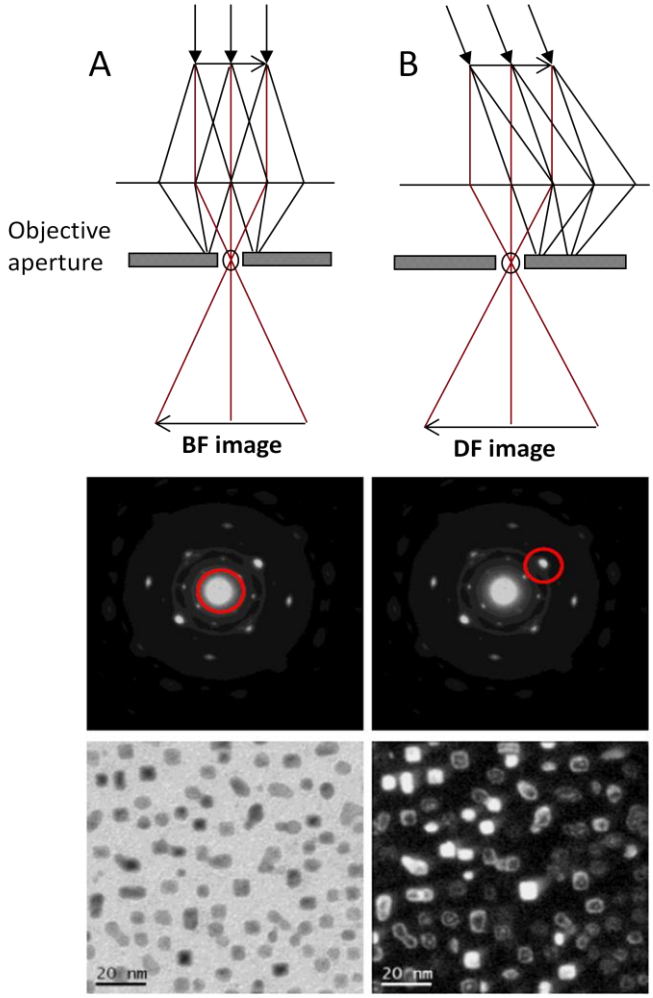

Fig 3: Conventional TEM imaging. (A) Bright-field schematic and image on bottom left. The red circle in A shows the primary beam is selected for this image. (B) Dark-field schematic and image of same nanoparticles by selecting the scattered beam and removing unscattered beam by the objective lens diaphragm.

2.3.2 Aberration-corrected High Resolution transmission Electron Microscopy (AC-HRTEM)

Compared to conventional TEM imaging HRTEM utilizes a larger or no objective aperture at all. This will cause interferences of transmitted beam with one or more diffracted beams and the contrast across the image will depend on relative phases of the various beams. This is called phase contrast imaging in which multiple beams selected with the aid of an objective aperture in the back focal plane of the objective lens contribute to an image. The relative phase shifts of various beams after interaction with the specimen leads to interference phenomenon which is highly sensitive to thickness, orientation of the sample and scattering factor of the constituting atoms. The main difference between conventional imaging (BF and DF) is the use of multiple beams rather than a single beam to create contrast as shown in figure 4.

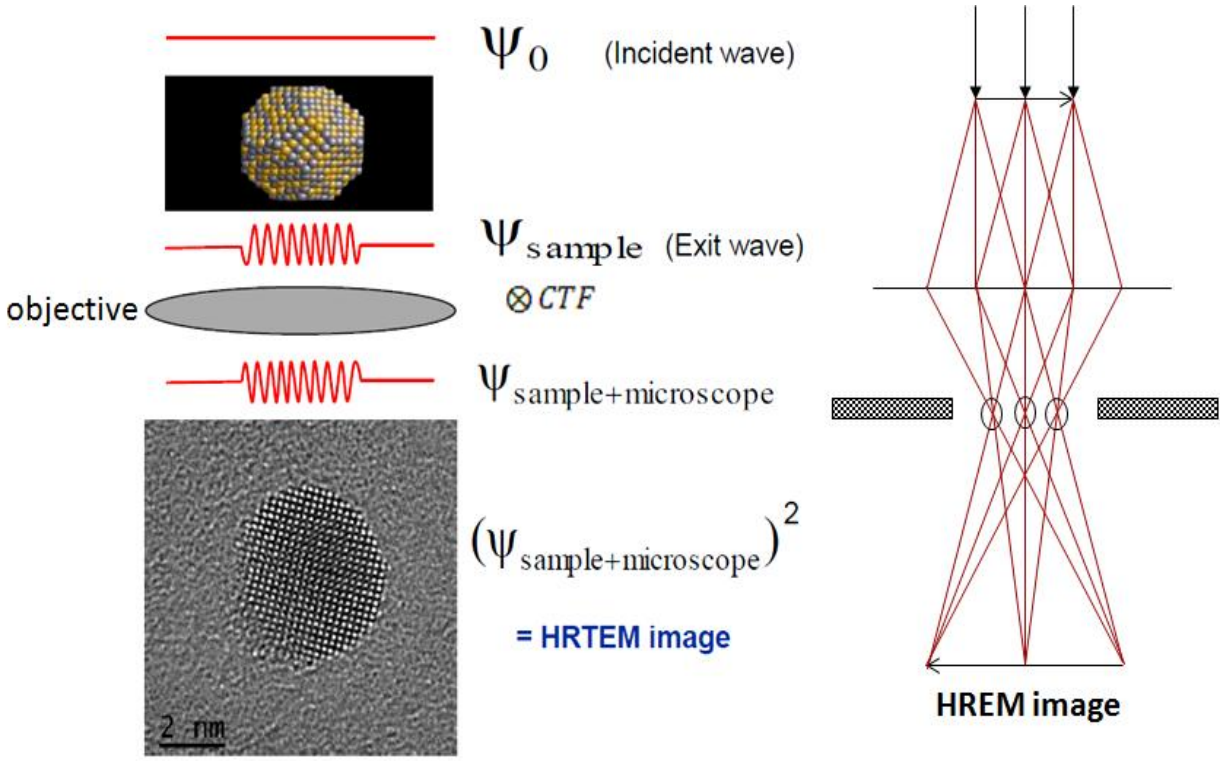

Fig 4: Image formation process and associated ray-diagram in HRTEM[5].

As described in figure 4, the process of image formation occurs in two steps. The electron wave function is initially modified by the electrostatic potential of atoms in the specimen. On the exit surface this wavefunction is further convoluted with the contrast transfer function (CTF) of the

objective lens. The final HRTEM images corresponds to the square modules of resulting wavefunction and it is magnified on the camera by the projector system[5 15]. Taking into account the origin of contrast, the distribution of the minima and maxima of intensity observed on HRTEM images does not represent in general the position of the atoms, but rather the periodic modulation of the phase of the wave front at the exit of the objective lens. A simulation of the interference is necessary to interpret contrasts quantitatively. However, as the periodicity of the contrasts is directly linked to the crystal lattice, HRTEM images and their fast Fourier transforms (FFT), make it possible to derive information on crystal structure and defects. As shown in figure 5, HRTEM images and their digital diffractograms make it possible to evidence the face-centered cubic (FCC) structure of gold nanoparticles and the symmetry and defects of multi-twinned nanostructures.

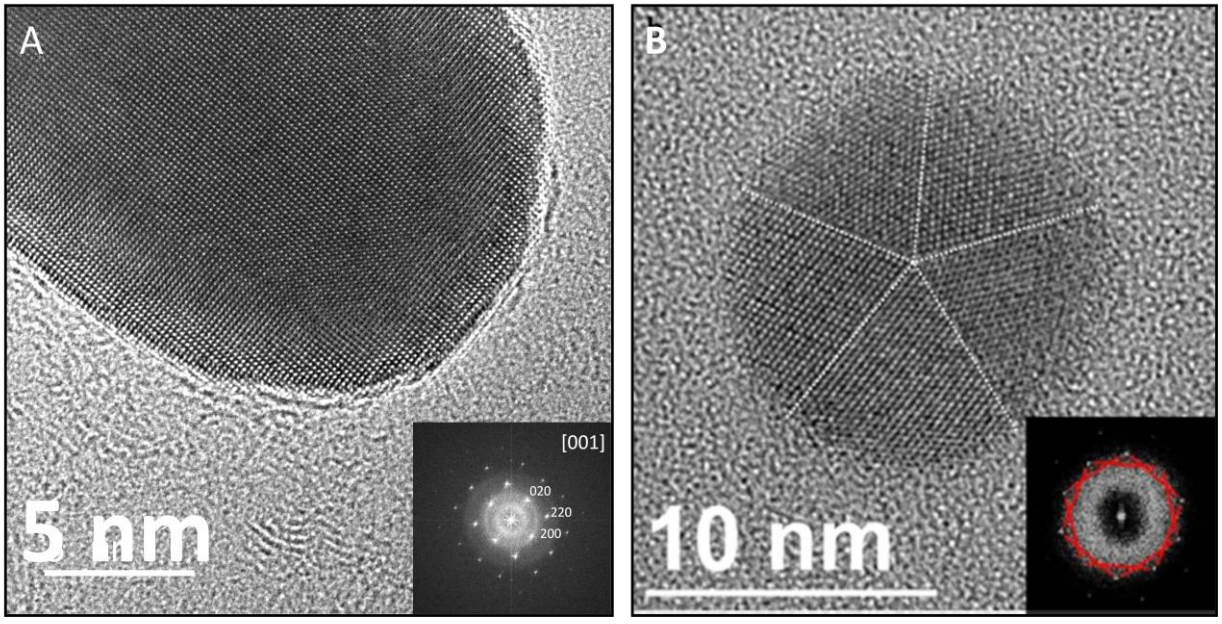

Fig 5: (A) HRTEM image of a gold nanorod. Inset showing FFT of the nanorod. The FFT is indexed with the FCC strcture of gold along [001] zone axis. (B) Decahedral nanoparticle (5-fold symmetry of [200] reflections highlighted on the FFT in inset). Image courtesy Alloyeau et al. Nanoletters[5].

As compared to light optic lenses, magnetic electron lenses are very poor. They have inherent aberrations much worse than the simple convex glass lens. A couple of decades ago, the resolution of microscopes reached the physical limit imposed by lens aberration and energy dispersion. For 200kV microscopes, the best resolutions were in the range of 0.18-0.17 nm and

high voltage TEMs reached resolutions of around 0.1 nm. This however entailed the problem of beam damage. Therefore focus was shifted towards correction of lens aberrations of objective lens for HRTEM[16]. Until the late 90's, it was impossible to correct for geometric aberrations, except for the defocus and the two-fold astigmatisms which can be directly measured on the FFT of a single image of amorphous materials. Consequently, HRTEM images resolution was limited by higher order aberrations, and specially by the spherical aberration. The only method to improve resolution was based on numerical correction of spherical aberration effects a posteriori on the basis of a series of images taken at variable focuses[17]. However latest high end microscopes come equipped with corrector technology for negating the effects of spherical aberration. The ARM 200F microscope used for high resolution imaging comes equipped with a CEOS hexapole type aberration corrector. Besides compensating for the spherical aberration of the objective lens, the CEOS corrector also corrects other high-order aberration (axial coma, three-fold astigmatism, star aberration and four-fold astigmatism). Coupled with cold FEG source, this aberration-corrected optics is able to achieve a point resolution of 0.75 Å under vacuum at 200 kV[18]. Moreover, corrected HRTEM images offer a clear visualization of nanocrystal interfaces (without delocalization of atomic contrast), which is significant advantage for studying nanocrystal faceting.

2.3.3 Scanning Transmission Electron Microscopy (STEM)

Scanning transmission electron microscopy (STEM) combines the principles of transmission electron microscopy as well as scanning electron microscopy (SEM). In STEM mode a very finely focused beam is rastered across the sample. Basically a series of lenses form a fine probe. These pre-sample lenses called condenser lenses demagnify the electron source to form a sub-nm probe at the sample surface (Figure 6). Scan coils are arranged to scan this beam in a square grid fashion on the sample surface. The signal generated at any point on the sample is captured by the detectors placed above the phosphorescent screen. This serial signal stream is correlated with beam position to build a virtual image in real time with the aid of computer systems. STEM imaging mode has certain advantages compared to broad beam illumination of TEM. The position of detectors and camera length can be varied providing enhanced flexibility of operation. An image in this mode can be acquired using only transmitted beam (Bright-field imaging) or scattered beams (Dark-field imaging). Commonly collected signals for imaging are either recorded in a BF or DF mode.

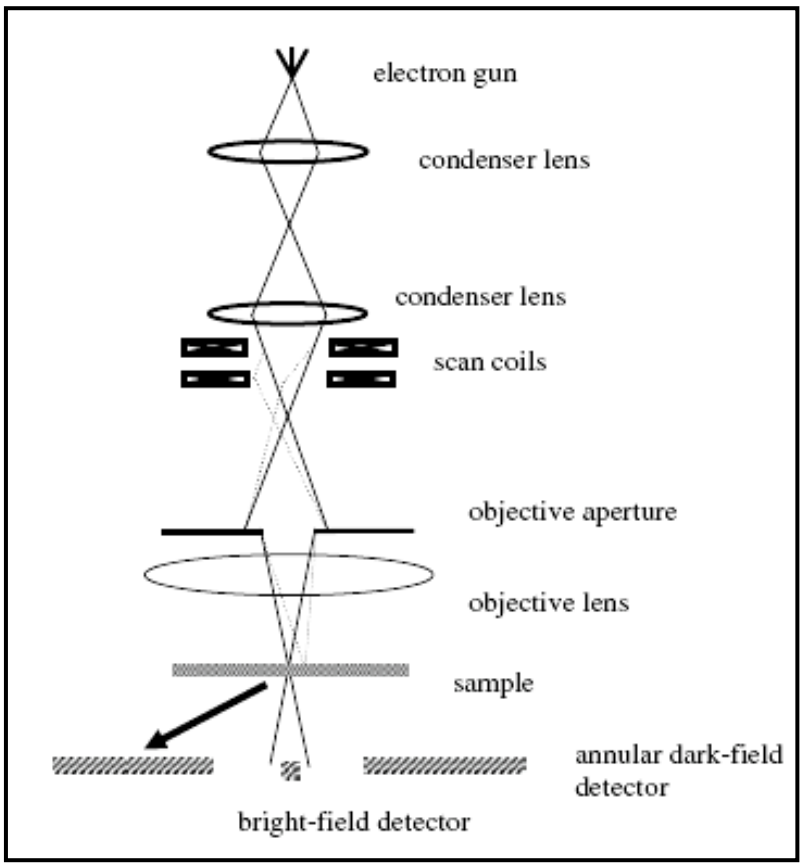

Fig 6: Ray diagram of image formation in a STEM showing smaller on-axis bright field detector and larger off-axis dark field detector. Image courtesy: P.D.Nellist[19] (Scanning transmission electron microscopy).

Transmitted electrons leaving sample at low angles or at an angle smaller than the convergence beam angle are used for BF mode, while those that leave the sample at relatively high angles with respect to the optic axis are used for DF mode. In case if scattering angles of collection are very high then imaging is known as high angle annular dark field imaging (HAADF). Although post-specimen optics is also present to control angles subtended by the detectors but these optics play no significant role in image formation processes[19].

The LCTEM work performed in STEM mode in this thesis was realized using HAADF detector. The detector is an annular disk with an electron sensitive region with inner radius in a range of few tens of milliradians to an outer radius of few hundred milliradians. STEM HAADF imaging is a far more popular mode. Especially at high scattering angles the coherent effects of elastic scattering could be neglected as it is entirely thermally diffuse.

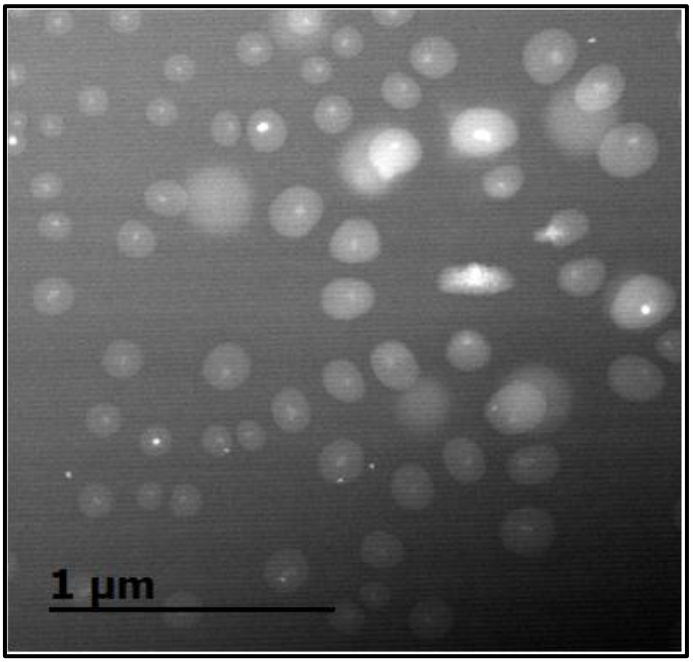

Fig 7: HAADF-STEM image of Au@Cu core-shell nanoparticles in a liquid cell. The variation in contrast of copper shell over gold nanoparticles is clearly visible.

The images acquired using HAADF detectors are very sensitive to chemical composition of the sample which is correlated with different levels of contrast in the image[20]as shown in figure 7. The intensity in images acquired is directly proportional to $\boldsymbol{\rho.t.Z^{\alpha}}$ where **α** is a constant between 1.5 and 2 while **ρ**, **t** and **Z** are respectively density, thickness and atomic number of matter[8]. This is the reason why HAADF is also called Z contrast imaging (Figure 7). It is worth mentioning that when mono-element nanoparticles are studied, STEM-HAADF intensities are then directly proportional to nanoparticle thicknesses. Additionally the contrast for relatively thicker samples is much better than other available imaging techniques. This is one of the reasons for using this particular mode for liquid cell experiments as the liquid thickness is greater than 150 nm. The ARM 200F microscope used for this work is only equipped with C_s image corrector which means the probe is uncorrected for aberrations. While this puts us in a disadvantage with regards to obtaining atomic resolution but the presence of cold FEG still makes up for a highly coherent electron source[18].

2.4 Analytical Microscopy

2.4.1 Energy Filtered Transmission Electron Microscopy (EFTEM)

EFTEM is a powerful tool to study the chemistry of nanoscale objects. It is actually based on EELS which measures the inelastic energy loss of electrons after interacting with the sample. In this technique basically the parallel beam imaging mode in TEM is coupled with principles of EELS to yield a filtered image or an elemental map. As in a very thin specimen most of the electrons pass unhindered while others are inelastically scattered, these ionization losses are characteristic of a particular element. Therefore a series of energy filtered images is acquired near the ionization edge of interest[21]. EFTEM is principally used in two ways. By zero loss filtering we remove all inelastically scattered electrons leading to increased contrast in TEM images. On the other hand by using electrons with well defined energy loss (ionization edge) elemental distribution maps can be created[22]. The working principle of EFTEM in a TEM is shown in figure 8.

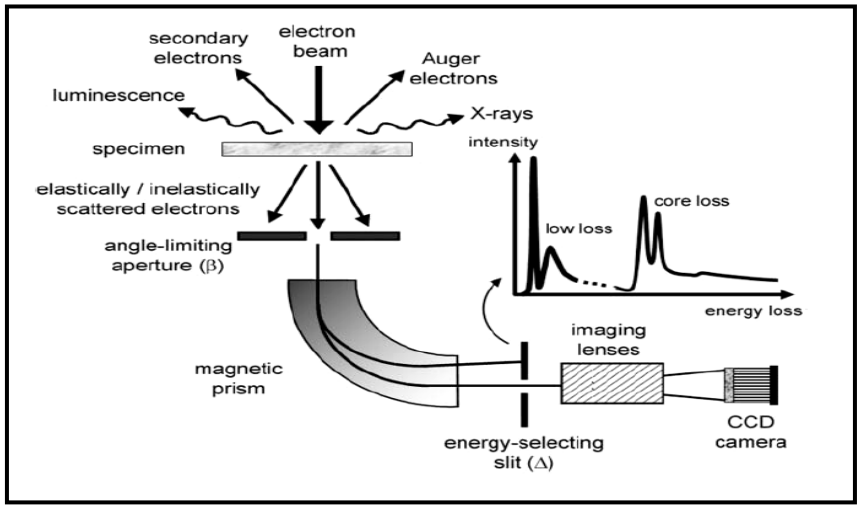

Fig 8: Acquisition process of EFTEM. Energy selecting slit at end of magnetic prism filters electrons of specific energies and sends them to a CCD device via optical lenses to form a filtred image. The graph on right side represents energy spectrum showing zero loss peak, low loss peak and core loss peak respectively. Image courtesy: P.J. Thomas and M. Weyland[22].

As seen in figure 8 a magnetic prism generates curved magnetic field which disperses electrons with different energies. The energy range is selected by means of a slit. This slit allows for

selecting electrons of certain energies to pass through the optical system at the end of which is a CCD device for recording images.

One of the advanced uses of EFTEM is to measure sample thickness using Log-Ratio method. This is done by recording the energy-loss spectrum and using integration to compare filtered image with unfiltered image. The thickness **t** is derived from the following equation[23]:

$$\frac{t}{\lambda} = \ln\frac{I_t}{I_o}$$

where λ is the total mean free path for ineleastic scattering, $\mathbf{I_t}$ is the unfiltered image comprising of elastic and inelastic scatterings while $\mathbf{I_o}$ is the elastic signal only. As the energy spectrum in figure 8 shows there is a low loss region and core loss region. Usually the core loss region is more sensitive to the thickness of liquid layer. In the case of thicker liquid layers low loss region gives us more information due to multiple scattering events masking the core loss signal while in thinner liquids core-loss signal is the primary source of information[24]. This method is employed by us for measuring the liquid thickness which is an important parameter for liquid cell experiments.

2.5 Sample Preparation for LCTEM Experiments

All liquid cell TEM experiments were realized on a Protochips Inc. provided in-situ Poseidon 210 liquid flow TEM holder. It has a three port system for flowing chemicals during the experiment allowing us to modify sample chemistry while at the same time dynamically imaging the changes made to the sample. The setup and apparatus for the liquid cell experiment is depicted in figure 9. The core components of liquid cell setup are two micromachined Si chips called e-chips. The dimensions of the smaller one are 2 x 2 mm while the larger one is 4.5 x 6 mm.

A SiN film of thickness around 50 nm constitutes two electron transparent windows in the centre of the two e-chips. The dimensions of both the windows are around 550 x 50 µm. Gold spacers on smaller e-chips control liquid thickness profile in the cell. Several sizes are available but we solely used 150 nm spacer e-chips for optimum imaging and flow conditions.

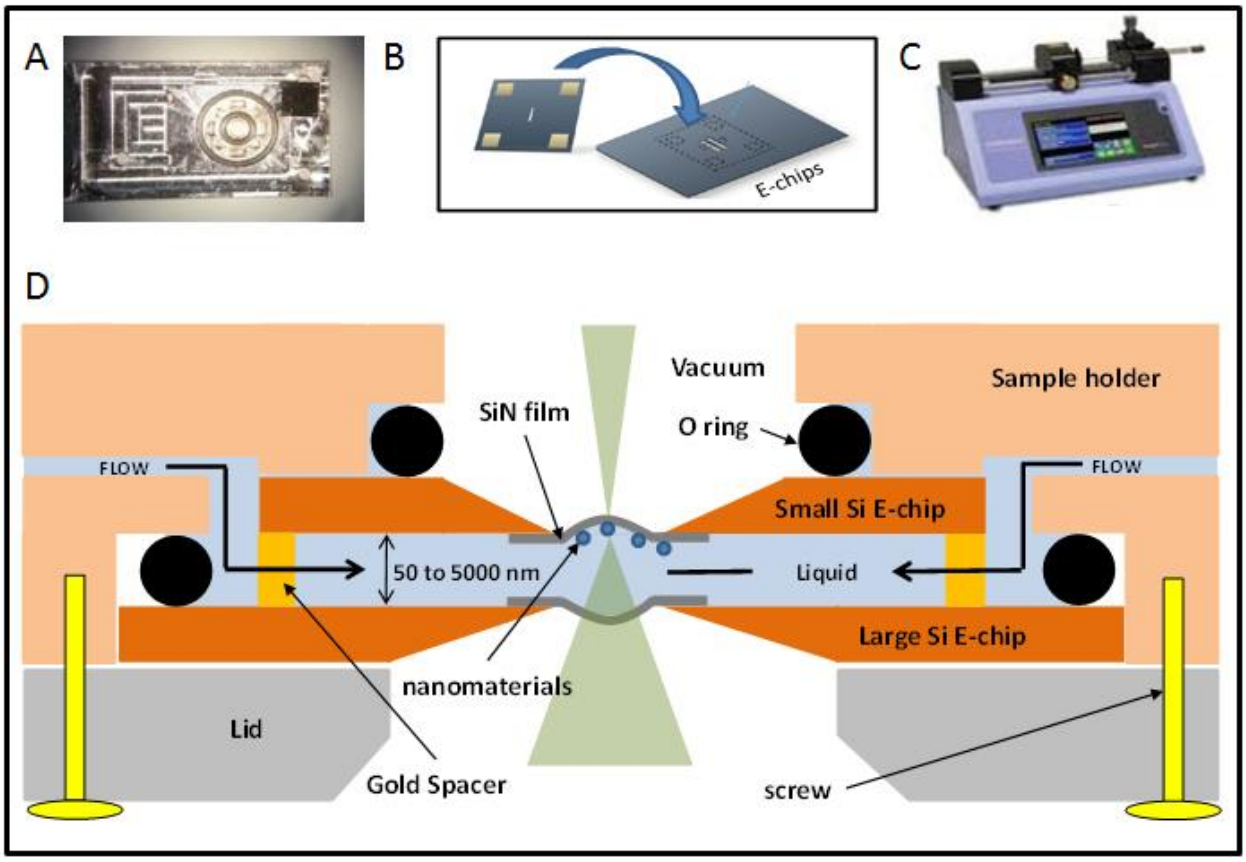

Fig 9: In-situ liquid cell setup (A) Tip of liquid cell holder with provisions for o-rings and e-chips.(B) Small e-chip with gold spacers along with larger e-chip which goes over the top of smaller e-chip. SiN membrane is etched in the centre of the two echips. (C) Syringe pump for precise liquid flow during the experiment. (D) Schematic cross section of the liquid cell. In Jeol microscope small e-chip at top due to rotation during insertion of sample holder.

While preparing the liquid cell at the tip of the holder a pair of O-rings is placed in the provided space as shown in figure 9A. The smaller e-chip is then placed on top of the smaller O-ring while the well inside the tip of the holder is surrounded by a bigger second O-ring. A 2.5 µl droplet of precursor loaded liquid is placed on top of the smaller e-chip membrane. Afterwards the bigger e-chip is placed over the smaller e-chip and second O-ring in a cross configuration. This leads to an exposed window having dimensions of 50 x 30 µm. The purpose is to reduce bowing of the membranes within the high vaccum of the TEM column. The whole assembly was then closed shut by screwing the lid of the sample holder making the liquid cell vacuum tight. Prior to inserting the holder in TEM, the holder was tested in a pumping station for a possible leak in vacuum of the system.

2.6 Calculation of Electron Dose Rates

It is imperative to have an idea of electron dose rates while performing LCTEM. As the interacting electrons are radiolysing the solvent causing a cascade of chemical reactions, thus varying electron dose rates ($\dot{d}$) have a profound effect on reaction kinetics. $\dot{d}$ is calculated usually in units of electrons/Å^{2}s by electron microscopists using following equation.

$$\text{Dose rate (electron / sA}^2\text{)} = \frac{\text{Beam current } (^{C}/_{s})}{\text{Elementary charge}(^{C}/_{\text{electron}}) * \text{irradiated area}}$$

Note that C/s corresponds to Ampere. Here we explained the methods used to measure and control the dose rate both in TEM and STEM mode:

For both TEM and STEM mode, liquid cell experiments were performed with a fixed condenser aperture and spot size. This was done to maintain a constant beam current.

In order to measure dose rate in TEM mode, an image of the beam on CCD device without any detail through a vacuum is taken as shown in figure 10C. On this image, we can measure the number of counts per Å^2. Knowing the conversion efficiency of detector (number of photons generated per electron) which is 52.37 counts/electron at 200kV in our case and the exposure time of the image, we can directly calculate the dose rate in electrons/Å^{2}s. TEM homogenously delivers a constant dose rate except at the edges of the beam where the Fresnel fringes alter the electron distribution. Changing the brightness of the beam results in changing the $\dot{d}$, because it modifies the irradiated area. However changing magnification has no effect whatsoever over $\dot{d}$ (figure 10D) as this simply changes the lens current of the projection lenses[25]. This means that in TEM mode increasing the magnification consists in magnifying the image formed by the objective lens. Keeping track of the dose rates used during experiments is very important. For this purpose two strategies can be actively employed: the constant $\dot{d}$ approach and the magnification dependent $\dot{d}$ approach. In the first method, the brightness is maintained constant during the whole LCTEM experiment. The main drawback of this constant $\dot{d}$ method is the limited range of usable magnification, as the brightness cannot be readjusted for countering the inherent decrease in luminosity when increasing the magnification. This drawback is reduced if a low magnification image with a finely focused beam (i.e. with high brightness) is used as a reference during the calibration step. The second approach is to maintain the size of the beam on the phosphorescent

screen constant during the whole *in situ* experiments. This method implies to readjust the brightness as soon as one modifies the magnification. Thus, as compared to the reference image acquired during the calibration step, the dose rate is inversely proportional to the square of the magnification.

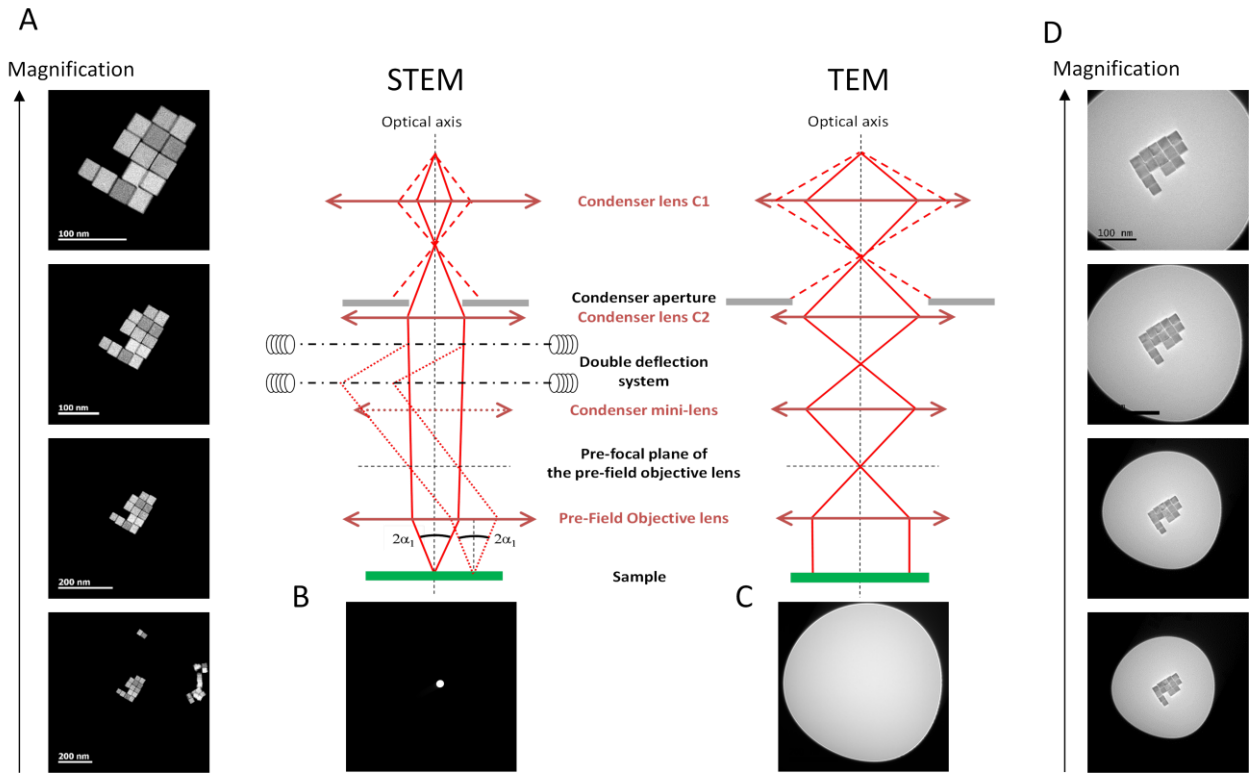

Fig 10: Impact of optical parameters on electron dose rate. (A) Increasing magnification drastically increases dose rate in STEM mode by reducing the scanned area. (B) Image of STEM probe on CCD device. (C) Image of TEM beam on CCD camera. (D) Increased magnification has no impact on the irradiated area of sample in TEM mode thus keeping constant electron dose.

STEM mode does not offer the possibility to maintain the dose rate constant with magnification. Indeed, as shown in figure 10A, as the magnification is increased the scanned area (i.e. the imaged area) is inevitably reduced and $\dot{d}$ is always inversely proportional to square of the magnification[26]. To calibrate the dose-rate in STEM mode, the image of the probe is acquired on the CCD camera (Figue 10B). This image allows calculating the beam current in (e^-/s). Therefore, the dose rate in electrons/Å^{2}s can be calculated for any magnification by dividing the beam current by the scanned area. Furthermore, $\dot{d}$ in units of electrons/Å^{2}s can be converted to Gys^{-1} (J

kg^{-1} s^{-1}) which is the unit of choice for radiation chemistry by multiplying $\dot{d}$ in electrons/m^2s by density normalized stopping power of solvent at the applied acceleration voltage and finally by the electron charge (1.6 x 10^{-19} C) in order to convert electron-volts to joules. Table 1 shows calculated dose rates for STEM imaging and its variation with the magnification, aperture sizes and probe sizes.

Electron Dose measurement	5C 3rd aperture	8C 3rd aperture	5C 4th aperture	8C 4th aperture
I_e beam current (e^-/s)	5.1×10^7	9.07×10^6	1.1×10^7	1.96×10^6
I_e beam current (pA)	8.32	1.45	1.89	0.314
50K $(\dot{d})$ electrons/Å^{2}s	0.023	4×10^{-3}	5.2×10^{-3}	8.7×10^{-4}
80K $(\dot{d})$ electrons/Å^{2}s	0.06	0.01	0.013	2.2×10^{-3}
100K $(\dot{d})$ electrons/Å^{2}s	0.09	0.016	0.021	3.4×10^{-3}
150K $(\dot{d})$ electrons/Å^{2}s	0.20	0.03	0.04	7.8×10^{-3}
200K $(\dot{d})$ electrons/Å^{2}s	0.36	0.06	0.08	0.013
250K $(\dot{d})$ electrons/Å^{2}s	0.57	0.10	0.13	0.02
300K $(\dot{d})$ electrons/Å^{2}s	0.83	0.14	0.18	0.03
400K $(\dot{d})$ electrons/Å^{2}s	1.47	0.25	0.33	0.055
500K $(\dot{d})$ electrons/Å^{2}s	2.31	0.40	0.52	0.087
600K $(\dot{d})$ electrons/Å^{2}s	3.26	0.56	0.74	0.12
800K $(\dot{d})$ electrons/Å^{2}s	6.18	1.077	1.40	0.23

Table 1: Dose rates calculated as a function of magnification, aperture size and probe size.

2.6.1 Miscellaneous Microscope Parameters Affecting Radiochemical Growth

Radiochemical growth is affected by several microscope parameters. Microscope parameters such as beam current and magnification can be used to increase or decrease the amount of reducing species as already discussed in the above passages. In addition to the parameters of

magnification and beam current, changing the acceleration voltage of microscope leads to a change in growth dynamics. This is due to the fact that changing acceleration voltage results in a corresponding change in cross sections for elastic and inelastic scattering. Normally increasing kinetic energies of electrons reduces radiolytic interactions as well as reduces beam broadening thus enhancing resolution. However there is inherent risk of knock on damage at high acceleration voltages for some materials. The type of imaging mode also affects growth dynamics and beam effects[13]. In TEM mode a more uniform and continuous dose is delivered to the sample while in STEM mode a periodic local dose is delivered to the sample. This has a remarkable effect on the distribution of ionized species in the liquid as well as changes in secondary reactions within imaged area. Precise control over reproducibility of results pertaining to radiochemical growth experiments requires a good understanding of these parameters.

References:

1. Rose, H. *Ultramicroscopy* **1994,** 56, (1-3), 11-25.
2. Pennycook, S. J.; Varela, M.; Hetherington, C. J.; Kirkland, A. I. *MRS bulletin* **2006,** 31, (1), 36-43.
3. Haider, M.; Hartel, P.; Müller, H.; Uhlemann, S.; Zach, J. *Philosophical Transactions of the Royal Society of London A: Mathematical, Physical and Engineering Sciences* **2009,** 367, (1903), 3665-3682.
4. Knoll, G. F., *Radiation detection and measurement*. John Wiley & Sons: 2010.
5. Alloyeau, D.; Mottet, C.; Ricolleau, C., *Nanoalloys: Synthesis, Structure and Properties*. Springer Science & Business Media: 2012.
6. Reimer, L., *Transmission electron microscopy: physics of image formation and microanalysis*. Springer: 2013; Vol. 36.
7. Shen, Q. *Characterization of Materials* **2000**.
8. Williams, D. B.; Carter, C. B., The transmission electron microscope. In *Transmission electron microscopy*, Springer: 1996; pp 3-17.
9. Krumeich, F. *Laboratory of Inorganic Chemistry, disponível em http://www. microscopy. ethz. ch/downloads/Interactions. pdf, consultado em* **2011**, 3-08.
10. Howie, A. *Revue de Physique Appliquée* **1980,** 15, (2), 291-295.
11. Egerton, R. *Microscopy research and technique* **2012,** 75, (11), 1550-1556.
12. Dillon, S. J.; Chen, X., Temperature Control in Liquid Cells for TEM. In *Liquid Cell Electron Microscopy*, Ross, F. M., Ed. Cambridge University Press: Cambridge, 2016; pp 106-126.
13. Abellan, P.; Woehl, T. J.; Parent, L. R.; Browning, N. D.; Evans, J. E.; Arslan, I. *Chemical Communications* **2014,** 50, (38), 4873-4880.
14. Fultz, B.; Howe, J. M., *Transmission electron microscopy and diffractometry of materials*. Springer Science & Business Media: 2012.
15. Mulvey, T.; Wallington, M. *Reports on Progress in Physics* **1973,** 36, (4), 347.
16. Tsuno, K. *Ultramicroscopy* **1993,** 50, (3), 245-253.
17. O'keefe, M.; Hetherington, C.; Wang, Y.; Nelson, E.; Turner, J.; Kisielowski, C.; Malm, J.-O.; Mueller, R.; Ringnalda, J.; Pan, M. *Ultramicroscopy* **2001,** 89, (4), 215-241.
18. Ricolleau, C.; Nelayah, J.; Oikawa, T.; Kohno, Y.; Braidy, N.; Wang, G.; Hue, F.; Florea, L.; Pierron Bohnes, V.; Alloyeau, D. *Microscopy* **2012,** 62, (2), 283-293.
19. Nellist, P. D., The principles of STEM imaging. In *Scanning Transmission Electron Microscopy*, Springer: 2011; pp 91-115.
20. Ponce, A.; Mejía-Rosales, S.; José-Yacamán, M., Scanning Transmission Electron Microscopy Methods for the Analysis of Nanoparticles. In *Nanoparticles in Biology and Medicine: Methods and Protocols*, Soloviev, M., Ed. Humana Press: Totowa, NJ, 2012; pp 453-471.
21. Verbeeck, J.; Van Dyck, D.; Van Tendeloo, G. *Spectrochimica Acta Part B: Atomic Spectroscopy* **2004,** 59, (10–11), 1529-1534.
22. Midgley, P. A.; Ward, E. P. W.; Hungria, A. B.; Thomas, J. M. *Chemical Society Reviews* **2007,** 36, (9), 1477-1494.
23. Egerton, R. F., *Electron energy-loss spectroscopy in the electron microscope*. Springer Science & Business Media: 2011.
24. Holtz, M. E.; Yu, Y.; Abruña, H.; Muller, D. *Microscopy and Microanalysis* **2012,** 18, (S2), 1094-1095.
25. Ahmad, N.; Le Bouar, Y.; Ricolleau, C.; Alloyeau, D. *Advanced Structural and Chemical Imaging* **2016,** 2, (1), 9.
26. Alloyeau, D.; Dachraoui, W.; Javed, Y.; Belkahla, H.; Wang, G.; Lecoq, H.; Ammar, S.; Ersen, O.; Wisnet, A.; Gazeau, F.; Ricolleau, C. *Nano Letters* **2015,** 15, (4), 2574-2581.

Chapter: 3

Growth Transitions in Dendritic Gold Nanostructures Driven by Electron Dose Irradiation History

Consideration of electron irradiation history is of prime importance while studying dynamical processes by transmission electron microscopy (TEM). This includes not only the instantaneous dose rate but also the cumulative dose delivered to the sample. Liquid-cell TEM was used to study the effects of the electron-irradiation history on the radiochemical growth of dendritic Au nanostructures. Besides the well-established direct link between the dose rate and the growth rate of the nanostructures, the cumulative dose in the irradiated area can also induce important transitions in the growth mode of the nanostructures. Comparing *in situ* observations with an extended diffusion-limited aggregation model revealed how the shape of the nanostructures are severely affected by the local lack of metal precursors and the resulting restricted accessibility of gold atoms to the nanostructures. The effects of electron irradiation on solution chemistry in the irradiated area as well as whole of liquid cell are emphasized in this chapter. The main purpose here is to explicitly reveal the molecular and atomic diffusion processes that impact the shape of dendritic nanostructures grown in water based solvent.

3.1 Experimental Details

3.1.1 Methods

A very high electron dose was used to carry out these dynamical studies in TEM mode of the microscope. The electron dose was calculated as described in the methodology section. Remarkably, if the illumination system remains constant during TEM experiments (i.e. if one does not touch the brightness knob), increasing the magnification does not affect $\dot{d}$. Indeed, magnifying a TEM image consist in enlarging the image given by objective lens with the projector system, which neither does modify the beam current (i_e) nor the irradiated area (S_b). All

the TEM experiments were conducted with the same illumination condition corresponding to $\dot{d}$ = 155 electrons/Å^{2}s (S_b = 0.85 µm^2 and i_e = 2 nA). We measured i_e on both the phosphorescent screen and the dynamic-calibrated CCD camera of the microscope prior to inserting the sample. Note that in some areas, the burst of nucleation could be initiated by slightly focusing the beam (i.e. increasing $\dot{d}$) but $\dot{d}$ was immediately reduced to 155 electrons/Å^{2}s after the growth start.

As we did not use the sample holder in flow mode and we used relatively high $\dot{d}$, the formation of hydrogen bubbles affected the distribution of the water inside the liquid-cell. As previously described and illustrated in figure 1, the formation of a large bubble on the middle of the liquid-cell tends to minimize the thickness of the liquid film at the surface of both windows (See appendix). With this liquid-cell configuration, we estimate the liquid thickness to vary from 150 nm (at the corners) down to a few tens of nm in the middle of the windows where HRTEM contrasts can be observed[1]. Note that the continuous growth of gold nanostructures demonstrates that the liquid-cell never completely dried out.

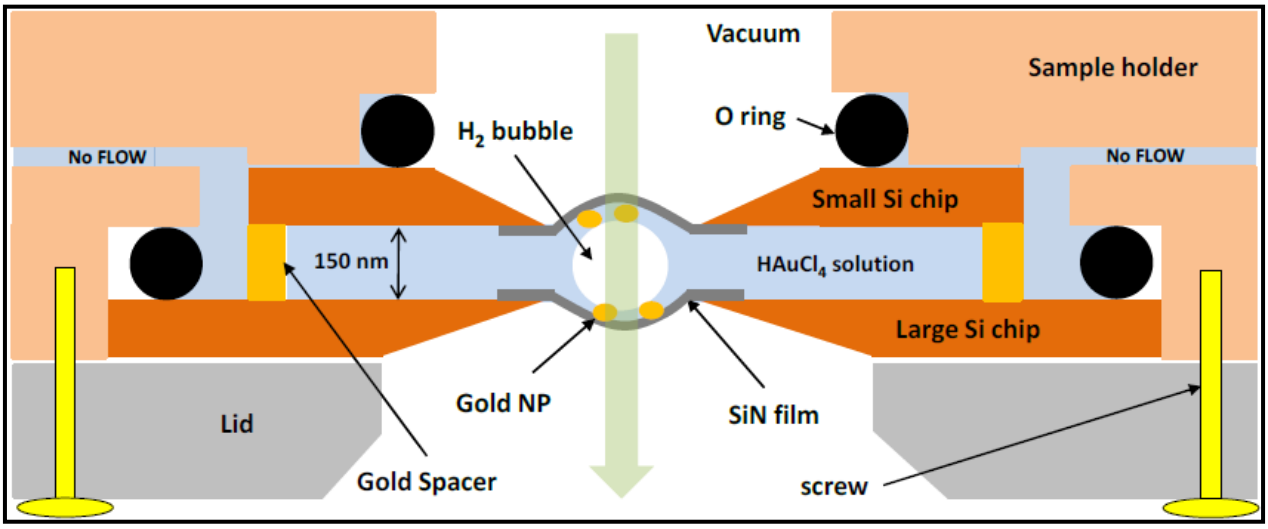

Fig 1: Schematic cross section of the sealed liquid cell in the JEOL ARM microscope under high dose rate.

3.2 Experimental Growth of Dendritic Gold Nanostructures

LCTEM experiments were conducted in TEM mode with a constant $\dot{d}$ = 155 electrons/Å^{2}s on an aqueous solution of $HAuCl_4$. When a new area of the sample is irradiated by the electron beam,

radiologically-produced e_{aq}^- reduce gold precursors and the nucleation of gold nanoparticles is quasi-instantaneously observed. Then, nanostructures of several hundred nanometers grow very rapidly along the window plane because of the thin film geometry of the liquid layer (figures 2A-B). Previous reports have demonstrated that the growth rate of metal NPs formed under high $\dot{d}$ is limited by the diffusion of metal precursor to the nanostructures[2, 3].

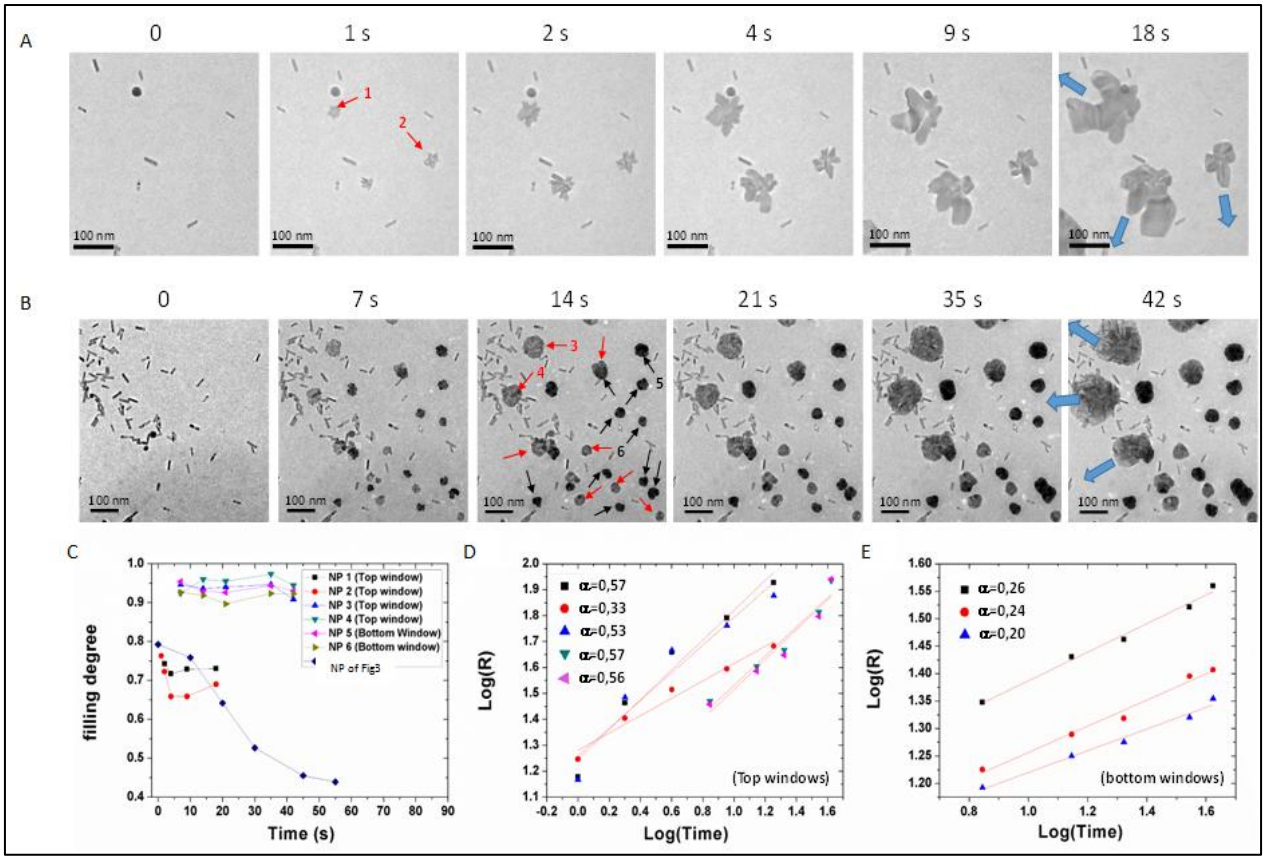

Fig 2: (A) and (B) Growth of gold nanostructures with high F_d followed by LCTEM in a pristine area (total dose at t = 0 is quasi null) with a $\dot{d}$ = 155 electrons/Å^{2}s. Gold nanorods deposited on the top window during sample preparation are seen on the images at t = 0. Red arrows indicate the NPs growing on the top window (same focus than the nanorods) whereas black arrows show the NPs growing on the bottom window. Blue arrows highlight the in-plane growth directions of the NPs. Acquisition time is indicated over each image. (C) Filling degree as a function of time for the NPs labelled from 1 to 6 on figure 2A and 2B and the NP of figure 3. (D) and (E) Logarithmic relationship between the radius of nanostructure-circumscribed circle and time for NPs on the top and bottom windows, respectively. The red curves show the linear fits of the data points and the slope α is indicated.

However many diffusion-related effects on the shape of the whole nanostructure remains to be clarified. In-focus imaging of this fast NP formation was facilitated by polymer-coated gold nanorods deposited on the small E-chip (top membrane in the microscope) prior to sealing the liquid-cell (Figure 2A-B, t = 0).

These nanorods also allow differentiating the NPs growing on the top or on the bottom window. Surprisingly, although the electron dose certainly increases at the vicinity of those nanorods because these latter generate many secondary electrons, gold NPs systematically nucleate and grow on the SiN membrane and seem unaffected by the nanorods. The PEG functionalization could possibly affect the surface chemistry of the nanorods and prevent the adsorption of additional gold atoms.

3.2.1 Quantitative Aspects of High Electron Dose on Growth kinetics

We quantify the degree to which a nanostructure fills its spatial domain by calculating its filling degree (F_d), corresponding to the ratio between its surface area and the one of its circumscribed circle. In pristine areas, where the total dose is quasi null at t = 0, we observe the formation of very dense nanostructures with high F_d. The shape of the NPs may differ from a pristine area to another. F_d varies from 65% for rounded NPs with very large excrescences (figure 2A) to 95% for spherical NPs (figure 2B). This shape-dependant value of F_d is reached a few seconds after nucleation and remains constant during the subsequent growth. Figure 2C shows that apart from the very first seconds of growth, the variation of F_d never exceeds 5 % in pristine area. Furthermore, this *in situ* study reveals that NPs observed in the same video may present very different growth dynamics The time-dependence of the NP growth can be approximated with a power law, $R \sim t^{\alpha}$, with R corresponding here to the radius of the nanostructure-circumscribed circle. Consistently with the very large size dispersion of the NPs, α varies greatly from a particle to another. Remarkably, our observations clearly show the influence of the nucleation location on the growth kinetic. Indeed, figure 2D-E reveals the boosted growth (α ranges from 0.2 to 0.55) and the broader size dispersion ($\bar{R}$ = 104 ± 64 nm at t = 42s) of the NPs on the top window as compared to the NPs formed on the bottom window (on which α remains below 0.26 and $\bar{R}$ = 63 ± 13 nm at t = 42s). This result highlights the disparity in $\dot{d}$ within the liquid-cell which is known to decrease with the depth in the liquid film due to electron absorption[4].

This disparity in the NP growth rate makes it difficult to compare these experimental data with the Lifshitz−Slyozov−Wagner growth model[5]. Although the growth speed is affected by the $\dot{d}$ -dependant concentration of reducing agent, F_d remains similarly constant and high on both membranes (Figure 2C).

3.2.2 Impact of Electron Irradiation History on Growth Morphology

Interestingly, the growth mechanisms in areas where the total dose is non-null before observation lead to the formation of dendritic nanostructures with much lower F_d. Figure 3 shows the growth of sharp dendrites over a nearly spherical nanoparticle formed during the 45 seconds of pre-exposure (d_{tot} before dendritic growth ~ 6975 electrons/A^2). This result highlights a transition in the growth mechanisms of the NPs. In view of the time dependency of R (figure 2D-E), after 45 seconds of pre-exposure the growth of spherical nanoparticles is very slow. The burst of nucleation of the dendrites was initiated by slightly focusing the beam (i.e. increasing $\dot{d}$) but $\dot{d}$ was immediately reduced to 155 electrons/$Å^2$s after growth start. Then, F_d of the whole nanostructure drastically drops from 79% to 43% in 55 seconds (figure 2C).

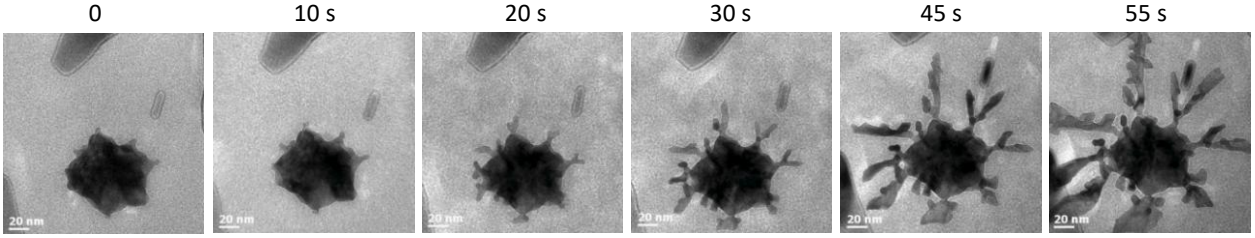

Fig 3: Growth of dendritic nanostructures followed by LCTEM with a $\dot{d}$ = 155 electrons/$Å^2$s in pre-exposed area. After irradiating a large area for 45 seconds (total dose at t = 0 is 6975 electron/A^2), TEM imaging was magnified to follow the growth of sharp dendrites on nearly spherical NPs. The filling degree of the whole NP is reduced from 79% at t = 0 to 43 % at t = 55 s (see figure 1(C)). Acquisition time is indicated over each image.

3.3 Diffusion Limited Aggregation (DLA) Model

DLA growth models are of primary interest because of intriguing aspects of non equilibrium growth. Typical DLA models involve addition of particles one at a time to a growing aggregate of similar particles via random walk or Brownian motion. The Diffusion Limited Aggregation

(DLA) was first proposed by Witten and Sander[6]. A simple version of such a model is presented in figure 4.

In this model two random walk trajectories are depicted originating at the launch circle with a radius of r_{max} + 5 lattice units whereby r_{max} is the maximum cluster radius as measured from the growth site. Trajectory t_1 starts from point S_1 and reaches the adjacent unoccupied site of the cluster shown by dashed boundary. The other trajectory of the random walker starts from S_2 and reaches the killing radius of limiting circle denoted $3r_{max}$. This killing radius is used to identify a disposal event when random walker crosses it and another particle is released from the launch circle point. The initial models contained less than 3000 particles however current models incorporate large number of particles. This was necessitated due to the fact that lattice anisotropy effects are minimal for small DLA clusters however they come to dominate for large cluster sizes. Attention has also been focused on off lattice DLA models in which the added particles follow Brownian paths[7]. DLA model has been used in many physical context, such as electrodepositon phenomena[8], neuron growth[9], bubbles of helium moving into a liquid media[10]. Several extension of the initial DLA model have been proposed, for example using a sticking probability[11], a size distribution of diffusing monomers[12] or including restructuring processes after collision[13].

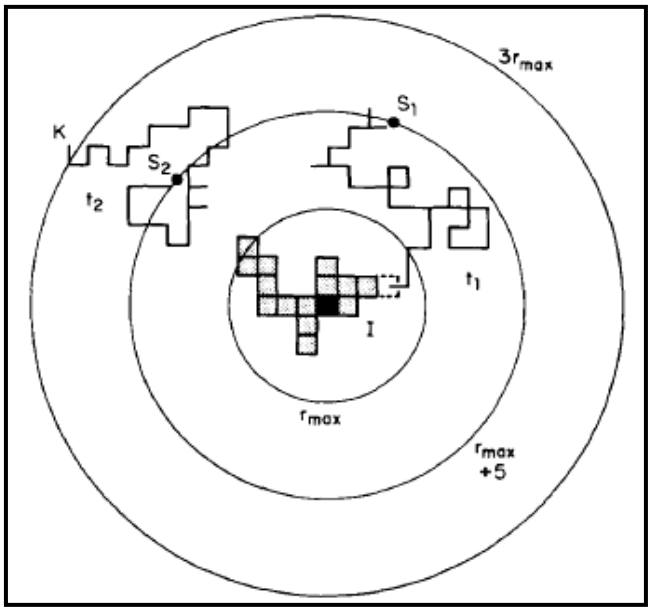

Fig 4: Simple square lattice growth model. The initial growth site is shown as black while the added sites to the cluster are denoted by shaded area[7].

3.3.1 DLA Model Used for Studying Dendritic Growth

The model considered in this work is an extension of the original model where monomers diffuse on a two-dimensional square lattice of 256*256 sites. We start with a nucleation seed at the centre of the lattice. This seed can either be a single monomer or an aggregate of monomers. Another monomer is allowed to walk at random, by first nearest neighbour jumps until it arrives at one of the sites adjacent to occupied sites. Then, the random walk is stopped and several attempts of surface diffusion jumps are performed. In our model, surface diffusion is mimicked by trying N_s times first or second nearest neighbour jumps along the surface. The local coordination number of the monomer (i.e. the number of occupied nearest neighbour sites) is computed in the initial and final surface positions, and the surface jump is accepted if the final coordination number is higher. In the case of equal coordination numbers, the jump is accepted with a probability equal to 1/2.

In this work we have tested two different ways of inserting a new diffusing monomer on the lattice. The first choice, which corresponds to the classical DLA algorithm, is to randomly select the position of the new monomer on a circle of radius $R + d_R$ where R is the radius of the aggregate and d_R is a positive radius increment. If d_R is chosen large enough this represents the process of a diffusing monomer from far away. The second choice is a random insertion of a monomer inside a given circular region of radius R_h (homogenous concentration condition). This nucleation process is inspired from the precipitation process occurring under the electron beam studied in this work. Finally, to increase the efficiency of the algorithm, a walking monomer is removed from the simulation if it diffuses too far away from the aggregate, i.e. when the distance to the aggregate is larger than $R+D_R$ where $D_R >> d_R$. This simple modification saves a significant computational time[14, 15].

3.4 Interpretation of Morphological Changes with Extended DLA Model

We have exploited an extended DLA model to describe in a didactic way the mechanisms affecting the shape of gold nanostructures during growth. In these simulations of aggregate growth, the flux of matter is ensured by inserting random walkers (i.e. monomers) on a 2D square lattice with a single nucleation seed at the centre of the square. As soon as a monomer visits a site adjacent to this nucleation seed, it becomes part of the growing aggregate. Although this model

does not account for the energy landscape of the nanoparticles, it allows considering the effect of monomer-diffusion pathway on the shape of the aggregate.

Figure 5A shows the general appearance of the 2D structures obtained when the monomers are randomly inserted inside a circular area around the nucleation seed. These conditions simulate the growth of a NP by adsorption of single atoms with a homogeneous local concentration of precursors. The circular area around the nucleation seed corresponds then to the electron beam irradiating a pristine area during LCTEM experiments. Growth in homogenous concentration always generates dense structures, with F_d of almost 50% when R of the aggregates reaches 100 lattice spacings (figure 5).

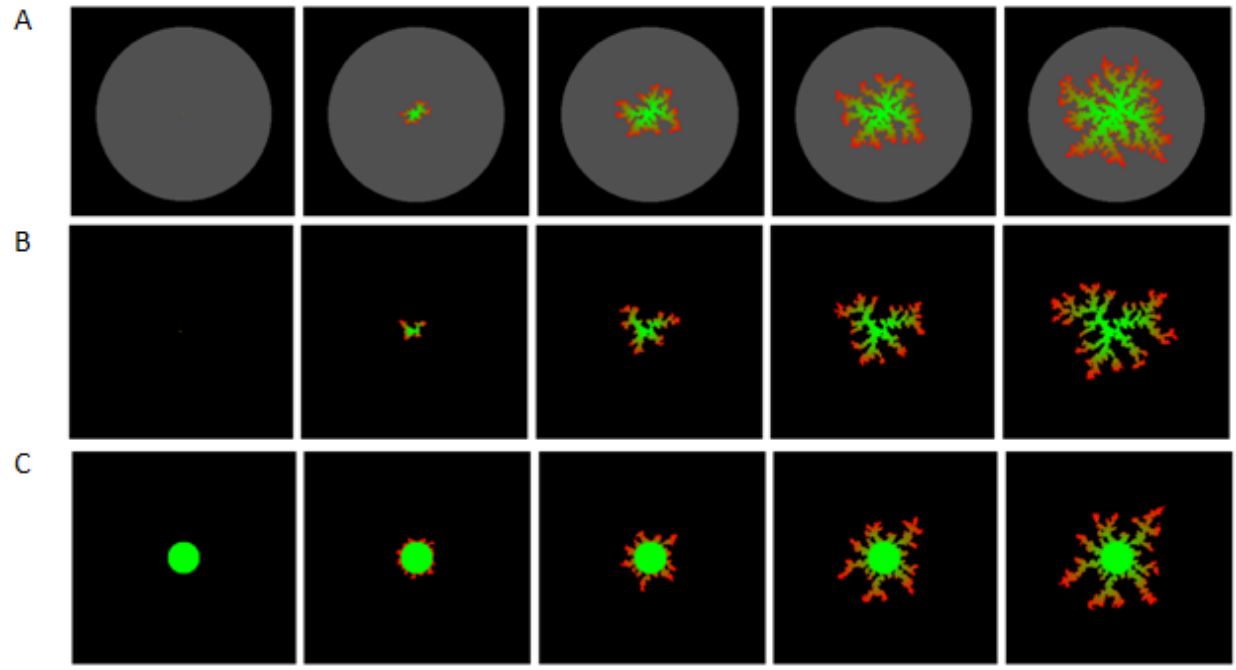

Fig 5: Aggregate growth calculated with the extended DLA model. The square lattice is made of 256*256 sites and the number of surface diffusion steps is 20. (A) The diffusing monomers randomly appear inside the bright area with a radius of 110 lattice spacings. (B) The monomers are inserted far away from the growing structure. This latter is a single site at the beginning of the simulation (C) The monomers are inserted far away from the growing structure. This latter is a circular particle of 20 lattice-spacing radius at the beginning of the simulation. The green-to-red color scale indicates the time at which aggregation occurred: the oldest aggregation events appear in green and the most recent in red.

Note that larger F_d are obtained at longer time (i.e. larger R) since monomers keep appearing in empty sites of the lattice. The growth model was used to display the effect of a depletion of monomer at the vicinity of a nucleation seed. Indeed, when random walkers are inserted far away from the nucleation seed (classical DLA conditions), the extended diffusion pathway of the monomers induces the growth of dendritic structures (figue 5B), with F_d below 25 % when R of the aggregates reach 100 lattice spacings (figure 5). Figure 5C shows that similar dendritic growth is observed when the central nucleation seed is a spherical aggregate. The dendrites are then homogenously distributed over the surface of seed and F_d drops from 100 % to 25%, while R increases from 20 to 100 lattice spacings (figure 6).

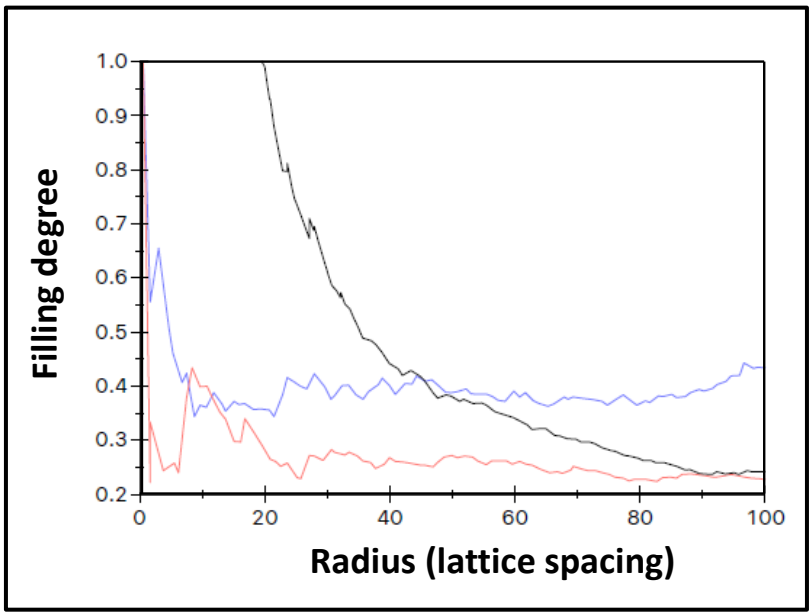

Fig 6: Filling degree as a function of the radius of the structures measured on the DLA simulations. Blue curve: NP of figure 5A. Red curve: NP of figure 5B. Black curve: NP of Figure 5C.

These simulations allow recapitulating the effects of the history of dose delivery on the growth processes of gold nanostructures. When following the growth in pristine areas, the abundance of Au precursors under the beam induces the growth of dense nanostructures with high F_d. The growth velocity then depends on both the local $\dot{d}$ (which depends on the observed window) and the concentration of precursors. When following the growth in a pre-exposed area, the formation of nanostructures during the pre-exposure time creates a depletion of precursors in the irradiated area. The subsequent growth is then kinetically limited by the diffusion of precursors from

unexposed regions to the electron beam and the diffusion of the monomer to the nanostructures. This inward flow of matter favours the formation of dendrites and reduces F_d, because the probability for gold atoms to reach the central NP drastically decreases with the spreading of the tree-like structure.

If the dendritic structures of NPs in pre-exposed area are the signature of DLA growth, one may wonder whether monomer/precursor diffusion also affects the shape of the NPs in pristine areas. This relevant question can be first tackled by estimating the consumption rate of gold precursors within the volume of interaction. Considering the precursor concentration of 1mM, the beam surface of 0.85 μm^2 and constant liquid thickness of 150 nm, we can estimate that the irradiated volume contains 7.7 10^4 $HAuCl_4$ molecules before irradiation. During LCTEM observations this volume is irradiated with a dose rate of 1.3 10^{10} electrons/s. By studying the growth of gold nanoplates of known thickness with similar illumination conditions and $\dot{d}$, Park and co-workers have estimated that the reduction of one Au^{3+} ion to Au atom requires 6000 primary electrons with an energy of 300kV[16]. As reducing the kinetic energy of primary electrons from 300kV to 200kV increases the energy density-normalized stopping power of water by 18%, we can estimate that in our LCTEM study 4920 primary electrons are necessary to reduce one Au^{3+} ions. Therefore, the electron beam can potentially consume 2.6 10^6 $HAuCl_4$ molecules per second. All these estimations directly depend on the local liquid thickness of liquid that is roughly estimated here. Nevertheless, we can conclude that the consumption of all the gold precursors in the irradiated volume before irradiation takes in fact much less than a second. In addition, 7.7 10^4 precursors could only generate a total volume of Au nanocrystals of 2.6 10^3 nm^3 (equivalent to a 14 nm nanocube) which is obviously much less than the total volume of gold NPs formed experimentally. Therefore, precursors coming from external areas of the beam are necessary to supply the growth of nanostructures of several hundred nanometers observed in pristine areas. This flow of matter is ensured by the diffusion of $HAuCl_4$ molecules. The diffusion coefficient of molecular species in water is known to vary linearly with their formula weight and the temperature. This linear relationship reviewed by Hobbie et al. [17] allows estimating the diffusion coefficient of $HAuCl_4$ in aqueous solution at 20°C to be around 0.5 10^{-9} m^2/s, meaning that in 1 second a molecule of $HAuCl_4$ can spread over 500 μm^2. This very efficient homogenisation of the solution concentration is in competition with the local beam-induced consumption of gold precursors and delays the creation of a concentration depletion zone around the NPs. This explains the fast formation of dense nanostructures in pristine areas. Nevertheless, after

approximately 15 seconds of observation, the first effects of the lack of precursors around the NPs can be identified. Figure 2A-B shows that the isotropic NPs at the early stage of the growth transform into anisotropic nanoparticles with anisotropy axes pointing to different directions (indicated by blue arrows).

3.4.1 Growth Anisotropy Due to Screening Effect

The growth anisotropy of the nanostructures is even more pronounced at longer time (see figure 7). As exemplified in the simulation shown in figure 8, this transition in the growth mechanisms arise from a screening effect that is characteristic of an extended diffusion pathway for the monomers.

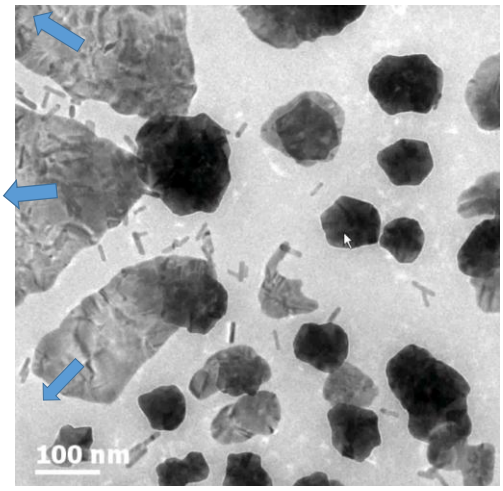

Fig 7: Anisotropic nanostructures formed after 2 mins observation in pristine area. Blue arrows highlight the different growth directions of the NP due to the screening effect.

We ran DLA simulations with three nucleation seeds on the square lattice. In homogenous concentration condition the three aggregates grow isotopically and finally coalesce (Figure 8B).

On the contrary, when the monomers are inserted far away from the nucleation seeds, the three aggregates grow along opposite outward directions (figure 8A) because the probability for a monomer to reach the region in between the three NPs decrease as the size of anisotropic nanostructure increases. This screening effect has a tremendous impact on the shape of the nanostructures because it governs the directionality of the growth, it prevents coalescence events and it also drives the tree-like structure of dendritic nanostructures.

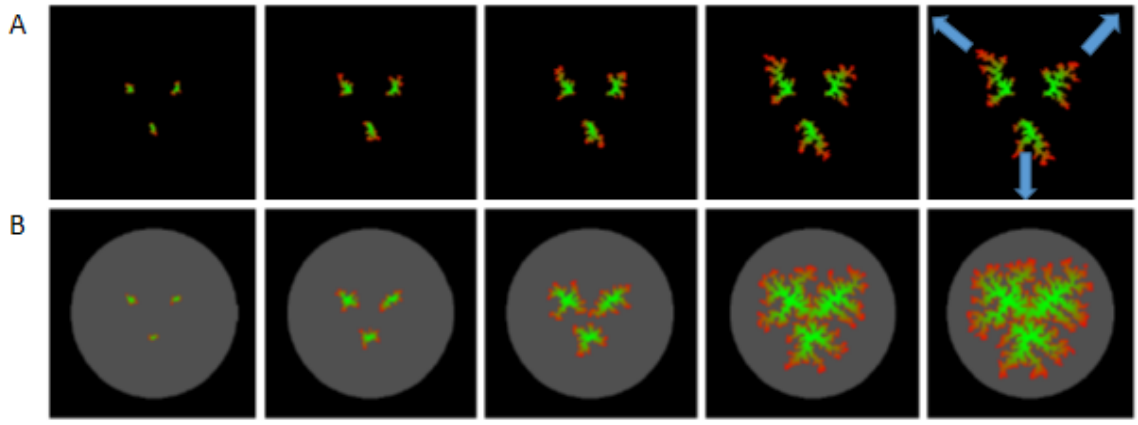

Fig 8: Aggregate growth calculated with the extended DLA model. The square lattice is made of 256*256 sites and contains 3 nucleation seeds (single sites at the beginning of the simulation). The number of surface diffusion steps is 20. (A) The monomers are inserted far away from the growing structures. Blue arrows highlight the growth directions of the NPs. (B) The monomers randomly appear inside the bright area with a radius of 110 lattice spacings. There is no preferential growth direction. The green-to-red color scale indicates the time at which aggregation occurred: The oldest aggregation events appear in green and the most recent in red.

It is worth noticing that given the potential consumption rate of gold precursors and the density of molecule per μm^2, the 15 seconds necessary to start observing the effects of monomer diffusion correspond to the time necessary for the beam to potentially consume all the precursors over an area of 428 μm^2. This large lack of precursors cannot be counter-balanced by molecular diffusion anymore and the growth directions of the NPs are then dictated by external-concentration gradients. Such characteristic transitions in the growth processes of nanomaterials could serve to evaluate the very dynamic and heterogeneous nature of local molecular concentrations during LCTEM observations. This also allows realizing that when the flow capabilities of the *in situ* sample holder are not used, precursor supply in the liquid cell irradiated with high $\dot{d}$ is far from inexhaustible. The fast depletion of the mean concentration of metal precursors within the whole liquid-cell explains the slowdown of the NPs growth rate over time when many pristine areas are consecutively analysed[18].

3.4.2 Crystal Reshaping Effects on Morphology

Finally, atomic scale monitoring of nanostructure growth reveals that crystal reshaping also affects the final morphology of the nanostructure. The tendency of nanocrystals to form energetically stable shapes is always in competition with the flux of atoms adsorbing on their surface. When the growth is fast (Figure 2A-B), crystal shape is dominated by kinetic effects leading to the disappearance of highly concave surface structure because the chemical potential of surfaces is inversely proportional to their curvature. This surface-diffusion mechanism tends to smooth NP surface and to form rounded and large excrescences. This effect can be simulated in our growth model by tuning the ability of adsorbed monomer to diffuse over the aggregate surface to reach sites of higher coordination. Figure 9 shows that increasing surface diffusion leads to the formation of larger dendrites and increases F_d of the nanostructure. When NP growth is slowed down by the weak availability of precursors in the local environment, the growth is then significantly impacted by thermodynamic effects and faceting of the dendrites is observed (Figure 10).

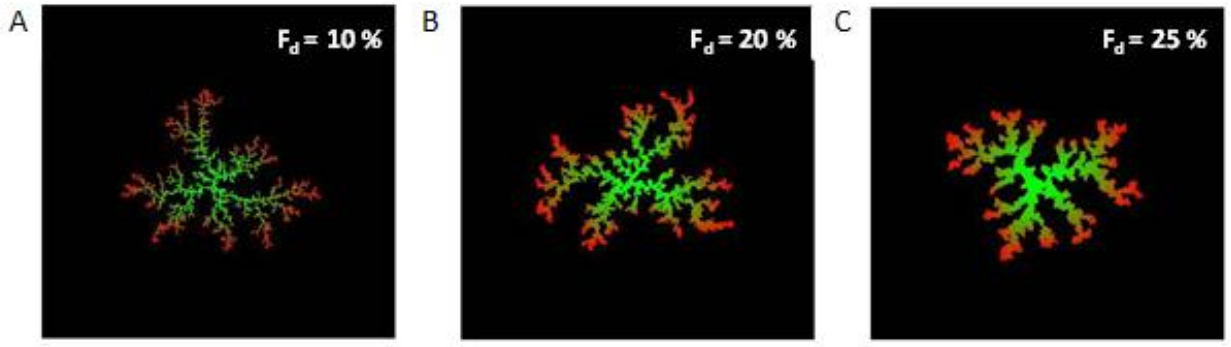

Fig 9: Effect of surface diffusion on the shape of aggregates obtained with the DLA growth model. The square lattice is made of 256*256 sites. The monomers are inserted far away from the growing structure that is a single site at the beginning of the simulation. The number of surface diffusion step is 1 (A), 10 (B) and 20 (C). The filling degree of the aggregates is indicated on each image. The green-to-red color scale indicates the time at which aggregation occurred: the oldest aggregation events appear in green and the most recent in red.

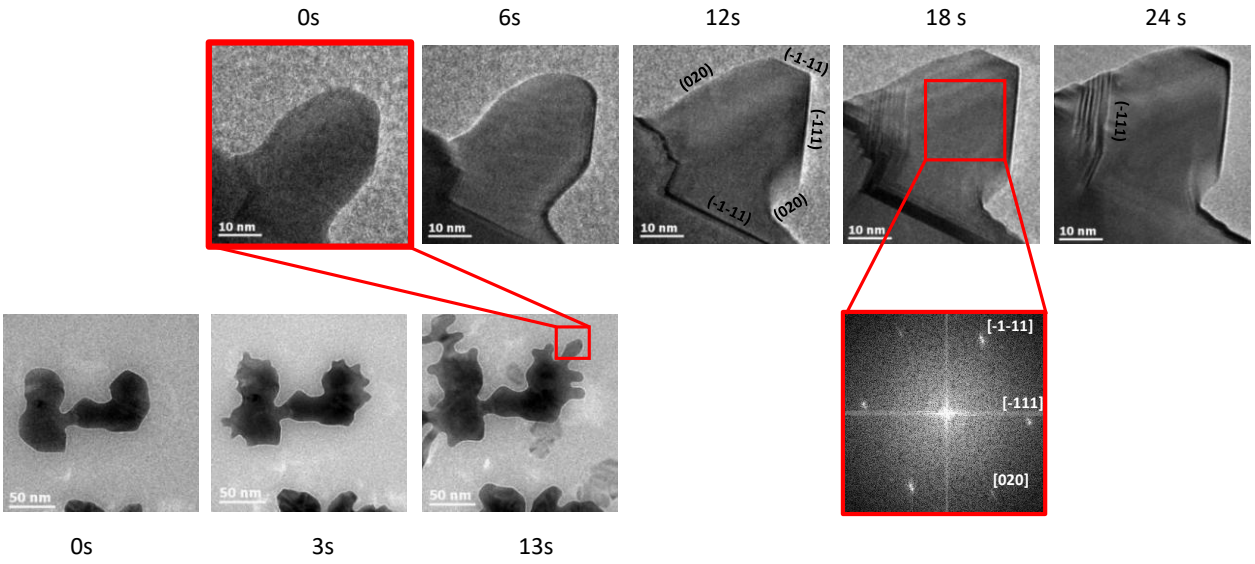

Fig 10: Reshaping of dendrites by surface diffusion and crystal faceting. Bottom images: growth of sharp dendrites on a large aggregate of NP. Top images: TEM imaging was then magnified to follow the reshaping of a dendrite at high resolution (time scale is reset to zero). Surface diffusion mechanisms tends to form (111) and (002) type facets. These phenomena tend to enlarge the dendrite. Facet indexes are deduced from the FFT of the image acquired at t = 18 s (bottom right) showing the FCC structure of gold oriented along the [101] zone axis.

HRTEM imaging reveals that low index crystal facets, such as (111) and (002) are preferentially formed, together with (111) planar defects most likely to relax the elastic strength accumulated during crystal growth and reshaping[19].

3.5 Conclusion

By comparing d_{tot} (total electron dose) - dependant LCTEM observations with an extended DLA growth model, we have demonstrated that the cumulative aspect of the electron dose can severely impact the growth mechanisms of gold nanostructures, because it affects both the availability of metal precursors and the accessibility of gold atoms to the NPs. High $\dot{d}$ irradiation of a pristine area of the liquid cell generates the growth of high F_d nanostructures and consequently creates a depletion of gold precursors in and around the irradiated area. In subsequent observations, this heterogeneous distribution of the precursors drives transformations in the nanostructure shape from isotropic to anisotropic or dendritic morphologies. This transition in the growth mode is imposed by the extended diffusion time of precursors to the irradiated area and a resulting

screening effect that imposes directional growth and tree-like structures with low F_d. As thermodynamic and kinetic effects are always in competition during NP formation, nanocrystal faceting can also reshape the dendrites when the growth is slow. More generally, these results illustrate that the history of the electron dose, combining the instantaneous $\dot{d}$ and the cumulative dose delivered to the sample, is a key parameter that cannot be ignored when analysing or designing *in situ* experiments.

References

1. Zhu, G.; Jiang, Y.; Huang, W.; Zhang, H.; Lin, F.; Jin, C. *Chemical Communications* **2013,** 49, (93), 10944-10946.
2. Kraus, T.; de Jonge, N. *Langmuir* **2013,** 29, (26), 8427-8432.
3. Zhu, G.; Jiang, Y.; Lin, F.; Zhang, H.; Jin, C.; Yuan, J.; Yang, D.; Zhang, Z. *Chemical Communications* **2014,** 50, (67), 9447-9450.
4. Liu, Y.; Lin, X.-M.; Sun, Y.; Rajh, T. *Journal of the American Chemical Society* **2013,** 135, (10), 3764-3767.
5. Lifshitz, I. M.; Slyozov, V. V. *Journal of physics and chemistry of solids* **1961,** 19, (1-2), 35-50.
6. Witten Jr, T.; Sander, L. M. *Physical review letters* **1981,** 47, (19), 1400.
7. Meakin, P. *Physica D: Nonlinear Phenomena* **1995,** 86, (1), 104-112.
8. Argoul, F.; Arneodo, A.; Grasseau, G.; Swinney, H. L. *Physical review letters* **1988,** 61, (22), 2558.
9. Caserta, F.; Stanley, H.; Eldred, W.; Daccord, G.; Hausman, R.; Nittmann, J. *Physical Review Letters* **1990,** 64, (1), 95.
10. Haard, T.; Gervais, G.; Nomura, R.; Halperin, W. *Physica B: Condensed Matter* **2000,** 284, 289-290.
11. Meakin, P. *Physical Review A* **1983,** 27, (3), 1495.
12. Braga, F.; Mattos, O.; Amorin, V.; Souza, A. *Physica A: Statistical Mechanics and its Applications* **2015,** 429, 28-34.
13. Jullien, R.; Meakin, P. *Journal of Colloid and Interface science* **1989,** 127, (1), 265-272.
14. Lee, S.-L.; Luo, Y.-L. *Chemical physics letters* **1992,** 195, (4), 405-411.
15. Braga, F.; Ribeiro, M. S. *Computer Physics Communications* **2011,** 182, (8), 1602-1605.
16. Park, J. H.; Schneider, N. M.; Grogan, J. M.; Reuter, M. C.; Bau, H. H.; Kodambaka, S.; Ross, F. M. *Nano letters* **2015,** 15, (8), 5314-5320.
17. Hobbie, R. K.; Roth, B. J., Transport in an Infinite Medium. In *Intermediate Physics for Medicine and Biology* Russell K. Hobbie; Roth, B. J., Eds. Springer New york, 2007; pp 81-109.
18. Abellan, P.; Woehl, T. J.; Parent, L. R.; Browning, N. D.; Evans, J. E.; Arslan, I. *Chemical Communications* **2014,** 50, (38), 4873-4880.
19. Klapper, H., Generation and propagation of defects during crystal growth. In *Springer handbook of crystal growth*, Springer: 2010; pp 93-132.

Chapter 4

Exploring the Seed-mediated Synthesis of Au Nanostars by LCTEM

The shape-dependent properties of gold nanostars (NSs) have motivated massive research efforts in the field of colloidal chemistry to gain a better control over the morphology of these promising nanostructures. Nevertheless, this challenge requires a better understanding of the atomic-scale processes leading to the formation of stellated nanoparticles. In this chapter an unprecedented *in situ* study focused on the seed-mediated synthesis of symmetric gold nanostars (NSs) performed by radiolysis in methanol is presented. We take advantage of the spatial and temporal resolutions of liquid-cell transmission electron microscopy (LCTEM) to unravel the key effects of the growth speed, seed-crystal morphology and dimethylamine functionalization on the formation mechanisms, shape and stability of NSs enclosed by high-index facets. Surprisingly, the stellation processes transforming icosahedral nanoparticles into NSs with 20 sharp arms entails a continuous restructuring of NS facets driven by surface diffusion, which provide a fresh look at faceting mechanisms.

4.1 Significance of 3D Au Nanostars

The last two decades have witnessed a remarkable increase in research activities related to the synthesis and characterization of gold nanocrystals. This increased interest can be attributed to the promising size and shape dependent physicochemical properties of Au nanoparticles, which can be exploited for various interdisciplinary research areas including but not limited to plasmonics, biomedicine and catalysis just to name a few[1-5]. Although Au nanoparticles with very various shapes have been fabricated, recent attention has shifted towards the synthesis of Au nanostars (NSs), as these multi-branched nanostructures with a central core, provide an opportunity to expand the broadening horizon of applications of gold nano-objects[6]. The distinguishing feature of Au NSs over other morphologies is the presence of arms with sharp tips

that give rise to narrow and tuneable surface plasmon resonance (SPR) throughout the entire visible and near IR spectrum holding much promise for biomedical applications[7-9]. Also, the local field strength near the apexes of the arms is enhanced significantly compared to incident light thus making a strong case for exploiting surface enhanced Raman spectroscopy (SERS) applications[10-13]. Although some one-pot methods have been reported, most wet-chemical syntheses of Au NSs combine both seed and functionalization-mediated growth[14, 15]. All these protocols involved the reduction of chloroauric acid ($HAuCl_4$) by strong or mild reducing agent (ascorbic acid, dimethylformamide, HEPES, hydrazine…) in presence of one or several capping agents (CTAB, CTAC, PVP, citrate…) to induce anisotropic growth of branches on preformed seed. Although these NSs have been studied for various applications, it remains challenging to exploit the full potential of these nano-objects because of their random shape. Indeed, the variation in the number and length of branches together with the rounded shape of the tips has detrimental effect on the optical properties of the Au NSs[16]. The poor control over NS symmetry raises awareness about the need to understand the atomic-scale mechanisms driving nanocrystal shape. The sophistication of nanostructure morphology and the complexity of experimental protocols combining several strategies to control the shape of nanomaterials make this task inherently difficult and favor the use of empirical approaches to improve bottom-up synthesis methods. Liquid-cell transmission electron microscopy (LCTEM) has opened up a new way to overcome this critical issue of nanomaterials synthesis by making possible *in situ* observation of nanocrystal formation in controlled-liquid environment[17-19]. For a few years, this MEMS-based TEM technique has allowed studying both kinetic and thermodynamic effects on the growth of nanomaterials that are dictated by the flows of matter and the stability of nanomaterials within their formation medium, respectively[20-22]. Therefore, many strategies to control the shape of nanomaterials have been studied *in situ*, including the seed-mediated[23, 24] and the face-blocking methods[25]. Here, we have performed TEM imaging in methanol to reveal the effects of growth speed, seed structure and alkylamine functionalization on the formation processes and stabilization of NSs enclosed by high-index facets. This work provides valuable *in situ* insights on the synthesis of symmetric NSs with tunable and controlled shape in a simple alcohol solvent.

4.2 Experimental Details

Like large-scale syntheses, the fabrication of gold NSs within the liquid-cell is based on two-step approach, consisting in the formation of seeds and the subsequent growth of NSs.

4.2.1 Methodology

A droplet of gold precursor ($HAuCL_4$, 1 mM) diluted in methanol was sandwiched between two silicon E-chips separated by 150 nm gold spacers as a first step. Accelerating voltage in all experiments was maintained at 200 kV. The sealed liquid-cell provides a 50 µm by 30 µm field of view in which the liquid is encapsulated between two electron-transparent SiN films (Figure 1).

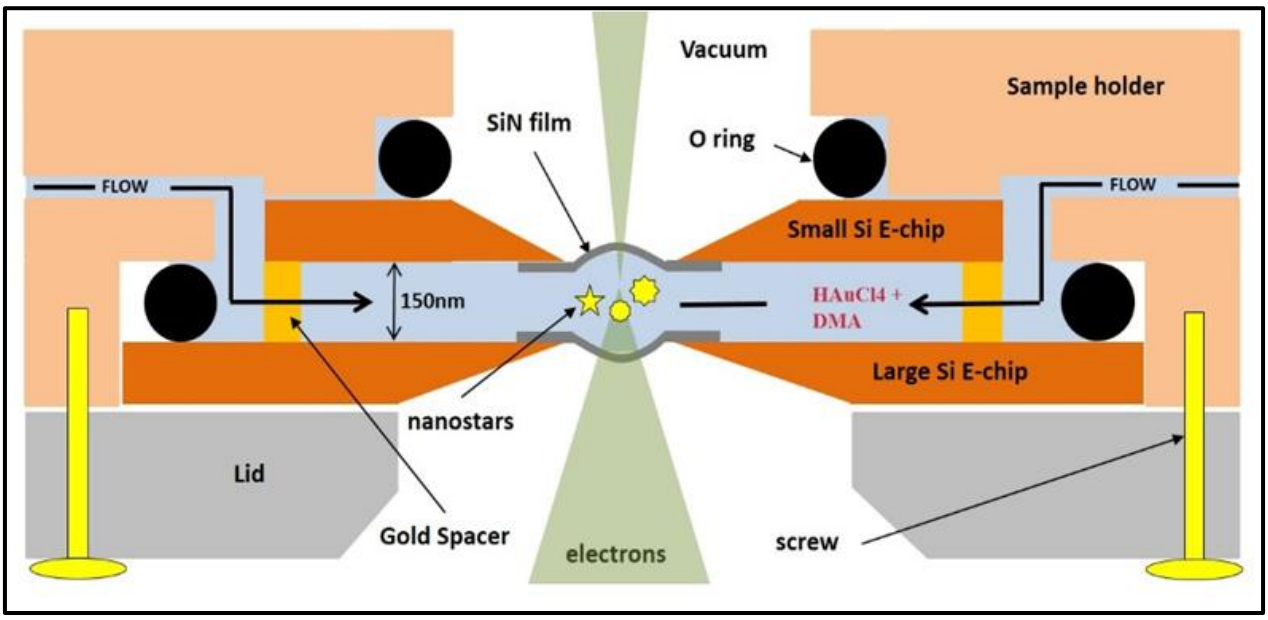

Fig 1: Schematic cross-section view of the liquid cell in the JEOL ARM microscope.

In situ experiments were performed in scanning mode using a high angle annular dark field detector (STEM-HAADF). Dose rate ($\dot{d}$) in this setup is dependent upon magnification, probe size, and condenser aperture. We varied $\dot{d}$ by changing the magnification and probe size (from 8c to 5c) while small condenser aperture (50µm) and 20 µs pixel dwell time was fixed in all experiments. $\dot{d}$ was calculated by dividing the beam current measured in electron per second prior inserting the sample by the image area in units of angstrom square ($Å^2$). To optimize image contrast, all the experiments were performed near the corners of the observation area, where the liquid layer is the thinnest due to an outward bowing of the SiN membranes under vacuum. Additionally we confirmed that the contrast of the observation window on low-magnification TEM images was characteristic of a fully filled liquid-cell before and after growth experiment. This roughly corresponds to thickness ranging from 150-380 nm (See appendix). 1 mM $HAuCL_4$ diluted methanol was continuously injected through the two inlets tubing of the sample holder

with a flow rate of 2.5 µL/min to refill the liquid-cell with gold precursors and to evacuate radiolysis products, especially H_2. Dimethylamine (DMA) with various concentrations was added to this injected solution during the second step of the NSs synthesis. All chemicals were purchased from Sigma Aldrich.

Ex situ HRTEM imaging was also performed after unsealing the liquid cell at the end of the first step (seed formation) and second step (NS formation) of the synthesis. Despite many attempts, acquiring *ex situ* images of NSs turns out to be impossible because, unlike nanoplates, stellated nanostructures never stay attached to the SiN membranes when unsealing the liquid-cell.

4.2.2 Formation of Seed Crystals

Seed crystals were grown radiolytically in several areas of the liquid cell in a solution that contain only gold precursors ($HAuCl_4$) in methanol. The radiolysis of this polar solvent presents many similarities with the radiolysis of water[26, 27], notably the production of solvated electrons (e_s^-) that are primarily responsible for the reduction of gold ions to gold monomers which cluster together to form nanoparticles. This solution as a first step was exposed to an electron dose rate of around $4.1*10^{-3}$ electrons/$Å^2$s at a low magnification of 50K. The beam current was significantly lowered to 1.5 pA by using the smallest probe size and small condenser aperture of around 50 µm diameter.

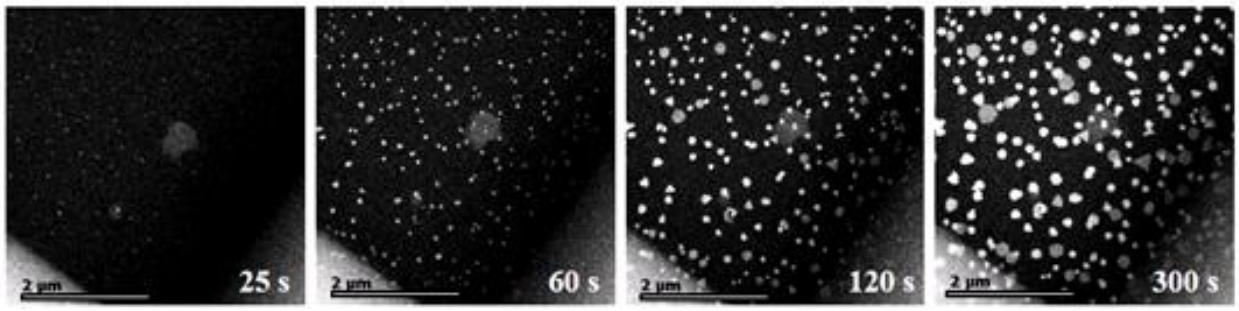

Fig 2: Time series of STEM HAADF image series acquired with $\dot{d} = 4.1 \times 10^{-3}$ electrons/$Å^2$s in the corner of the liquid-cell showing the nucleation and growth of 2D and 3D nanostructures in methanol.

As seen in first image of figure 2 nuclei first appear in an unirradiated region near the corner of the liquid cell after 25 s of irradiation. In the later images these nuclei grow to form different morphologies.

4.3 Morphological Aspects of Seed Crystals for Au Nanostars Formation

As in water[21, 22], the morphology of the nanostructures synthesized in methanol depends on the electron dose rate ($\dot{d}$) and low $\dot{d}$ regime (< 10^{-2} electrons/sÅ^2) favours the formation of highly faceted seeds. The beam-driven growth is then dominated by thermodynamic effects because the low adsorption rate of gold atoms on surface provides enough time for nanoparticles to reach energetically-stable shapes, corresponding to local minima in the Gibbs free energy of formation that are known to vary with temperature and nanoparticle size[28]. As shown in figure 3, three types of nanocrystals are mainly formed under such conditions: 2D plates and 3D icosahedral and decahedral particles.

The shape of the 3D nanostructures can be ambiguous on low-magnification images acquired in liquid due to poor resolution and the misorientation of the nanocrystals with respect to their main symmetry axes. Nevertheless, high resolution imaging (HRTEM) performed *ex situ* after this seed-growth step, clearly revealed that 2D plates, icosahedral and decahedral particles are formed. For example, the projected shapes and the characteristic atomic contrasts observed in figures 3B and C allow identifying an icosahedral and a decahedral nanoparticle along their three-fold and five-fold rotational-symmetry axes, respectively[24, 29, 30]. While the Au platelets have a large size dispersion, icosahedral and decahedral particles have a mean size of 33 ± 9 nm and 51 ± 11 nm, respectively.

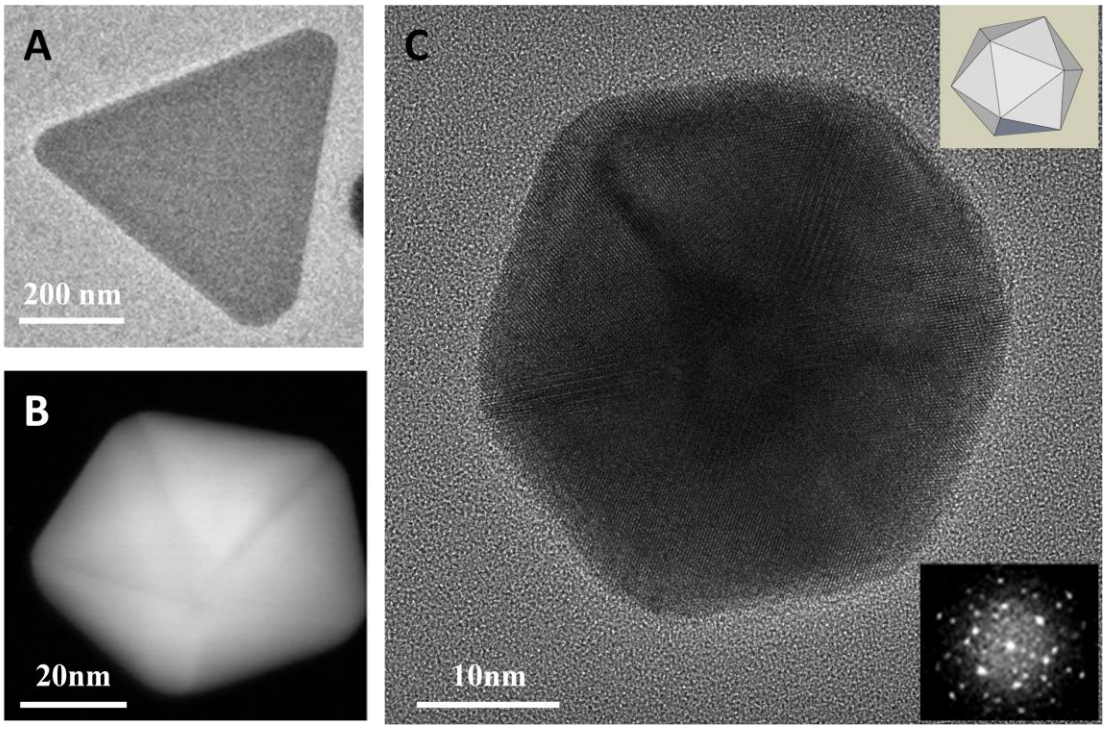

Fig 3. Nucleation and growth of Au seeds in methanol. (A) Ex situ TEM image of a nanoprism formed in the liquid-cell. (B) Ex situ STEM-HAADF image of a decahedral particle with its (111) triangular facet parallel to the substrate. (C) Ex situ HRTEM of an icosahedral particle along the three fold rotational axis. The FFT of the HRTEM image and a 3D model of the icosahedral particle are in the bottom and top right inserts, respectively. Such icosahedral particles served as seeds for the formation of symmetric NSs.

4.3.1 Distribution of Various Particle Morphologies in Liquid Cell

Ex situ HRTEM and STEM imaging were utilized to statistically calculate the distribution of particular type of crystal shape. 2D morphologies can be easily separated from 3D growth due to differences arising out of STEM-HAADF contrast. The particle morphologies are color coded in figure 4A. In figure 4B we can see that plate like morphologies account for approximately 21% of the overall growth. Among 3D nanocrystals the most abundant ones are the icosahedral nanoparticles (36%) followed by decahedral morphologies (13.77%). Around 20% of grown seeds are irregular in shape with no particular morphology. There are also trace amount of nanorods and bi-pyramidal nanoparticles. This richness in particle morphologies is characteristic of liquid phase synthesis in the microscope with precursor loaded solvent.

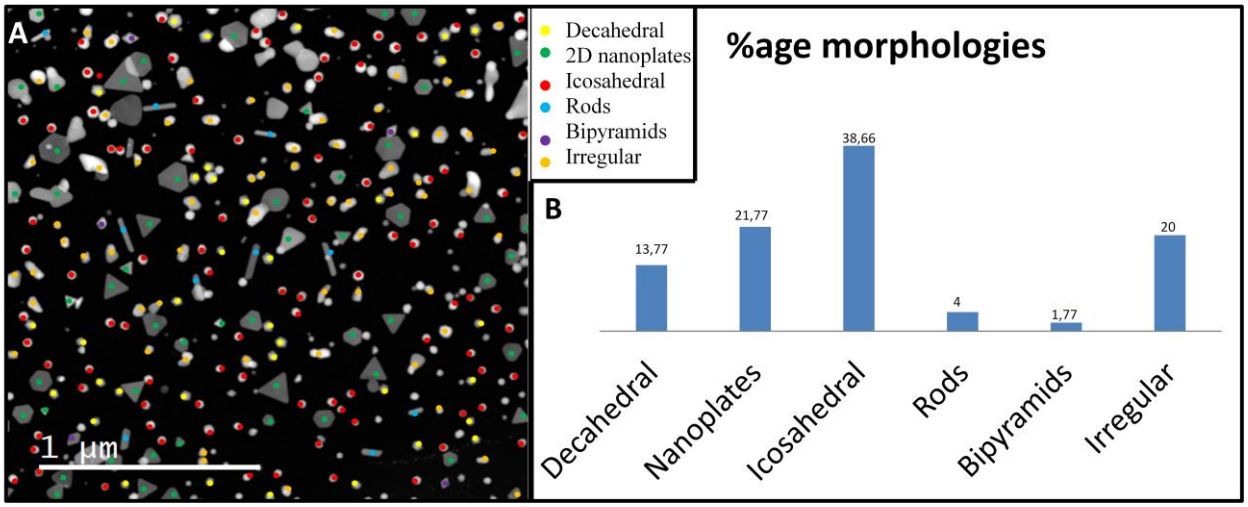

Fig 4: Shape analysis of the Au seeds formed. (A) Ex situ STEM-HAADF image of the nanoparticles formed during in situ synthesis in methanol (image acquired on the small E-chip, after unsealing and drying the liquid-cell). The nanoparticles are classified by shape with colored dots (the color code is indicated on the right). 2D plates are easily distinguished from 3D particles because nanoparticle contrast directly depends on their thickness on STEM-HAADF images. (B) Statistical distribution of the nanoparticle shapes.

4.3.2 Growth Kinetics in Water *vs* Methanol

Results obtained from experiments performed by Alloyeau et al[21] in de-ionized water (inorganic solvent of choice for most *in situ* experiments) were compared to growth experiments performed in methanol (organic solvent). It is interesting to note that same type of morphologies were observed for both solvents despite unique radiolytic chemistry of solvent, further strengthening the argument that in the absence of surfactants and capping agents, growth morphology is predominantly dictated by internal crystal structure of seeds.

It is also important to mention here that the number and distribution of each type of particle morphology does not change by a big margin in both solvents. Bar chart in figure 5A makes the comparison of growth in these two mediums. We see that the ratio of nanoplates in methanol is a little bit higher than in water.

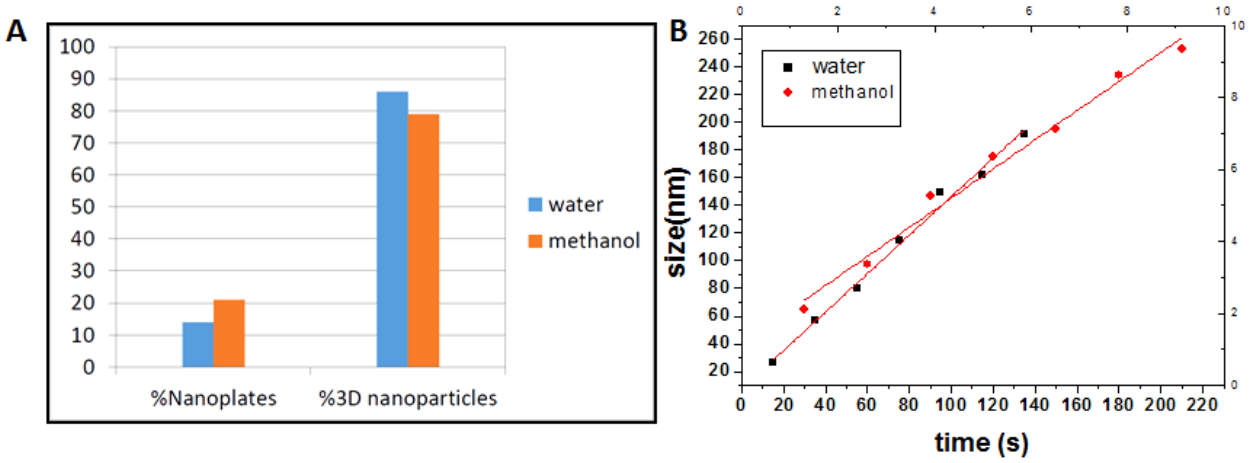

Fig 5: (A) Histograms showing the percentage of 2D nanoplates and 3D nanoparticles formed in water and in methanol by low-dose LCTEM (in STEM mode). Results obtained in water were extracted from [Alloyeau et al. Nanoletters 15, 2574 (2015)]. (B) Comparison of growth rates of nanoparticles in water and methanol with low electron dose rates of around $\dot{d}$ = 3.4*10^{-3} & 4.1*10^{-3}electrons/Å^{2}s respectively.

Furthermore as the growth kinetics of radiolytically produced Au nanoplates is a direct function of the electron dose rate $\dot{d}$**,** we compared the growth speed of Au nanoplates for mean equivalent $\dot{d}$ radiation in water and methanol. It was observed that the growth of nanoplates in water was 1.2 times faster than in methanol as observed in plot 5B. Nevertheless this is not a huge difference establishing the fact that both solvents contain competing oxidizing and reducing species[26, 27].

4.3.3 Defect Structure in Seed Crystals

The diversity in nanocrystal shapes is dictated by the formation of planar defects that break the cubic symmetry of the gold atomic lattice. As illustrated in Figure 6C, we systematically observed theoretically forbidden reflections on the Fourier transform of the HRTEM images of 2D nanoplates. The presence of this theoretically forbidden reflections arises from the stacking of planar defects (stacking faults or twin planes) all parallel to the top and bottom (111) faces[31-33]. The d-spacing for forbidden reflections was found to be 2.4 Å which correspond to Bragg diffraction from $\frac{1}{3}${422} planes. Additionally the six fold symmetry of {220} reflections can be observed. The large surfaces exposed on the top and bottom correspond to {111} planes which grow laterally along the SiN membrane. This is true for most FCC crystals as the structures want

to minimize their surface energies by growing densest atomic planes which is {111} for Au and Ag. Typically in these structures the stacking fault energy (SFE) is very low thus favorably causing the formation of planar defects.

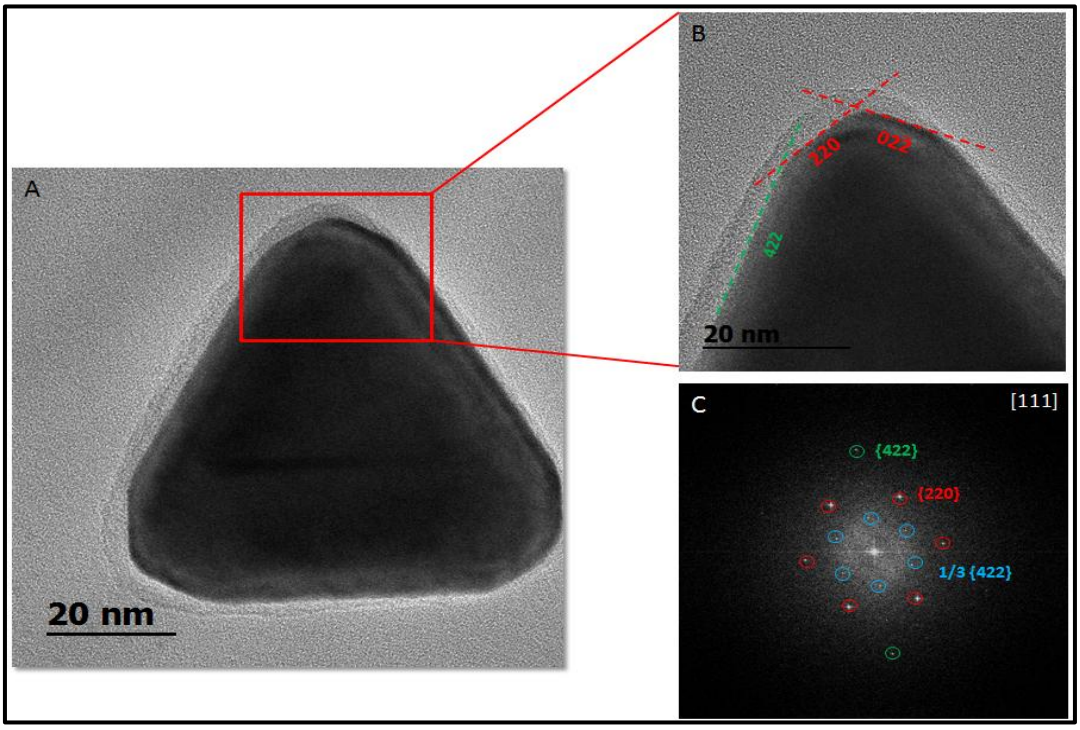

Fig 6: (A) HRTEM ex-situ image of Au nanoplate. (B) Zoomed-in image of the corner of nanoplate. (C) Fast fourier transform (FFT) of the nanoplates showing the presence of $\frac{1}{3}${422} forbidden reflections in addition to regular {220} and {422} spots along [111] zone axis. The growth solution was methanol in this case.

As previously reported, this peculiar configuration of crystal defects creates preferential adsorption sites on the side face of the nanostructures and promotes their 2D growth along the (111) plane[34-36]. On the contrary, the growth of facetted 3D nanoparticles arises from multiple twinning processes along different directions. Interestingly, the two large facets of the 2D plates, the 20 triangular facets of the icosahedral particles and the 10 triangular facets of decahedral particles are all (111) planes, which are known to be stable because of their low surface energy. The low magnification used to form these facetted nanostructures does not allow studying dynamical twining processes to distinguish, for example, if 3D multi-twined particles are formed

through nucleation-based layer-by-layer growth or successive growth twinning[37]. In the following, icosahedral nanoparticles are used as seeds for the formation of 3D NSs.

4.4 Functionalization & Growth Mechanism of Au Nanostars

The seed-mediated synthesis of Au NS was carried out with the assistance of dimethylamine (DMA), because alkylamines have recently been identified as an efficient stabilizing agent of high-index facets leading to the formation of symmetric NSs[16]. After forming seeds in several areas of the top SiN membrane, the beam was shut off and DMA was continuously injected in the liquid cell together with gold precursors.

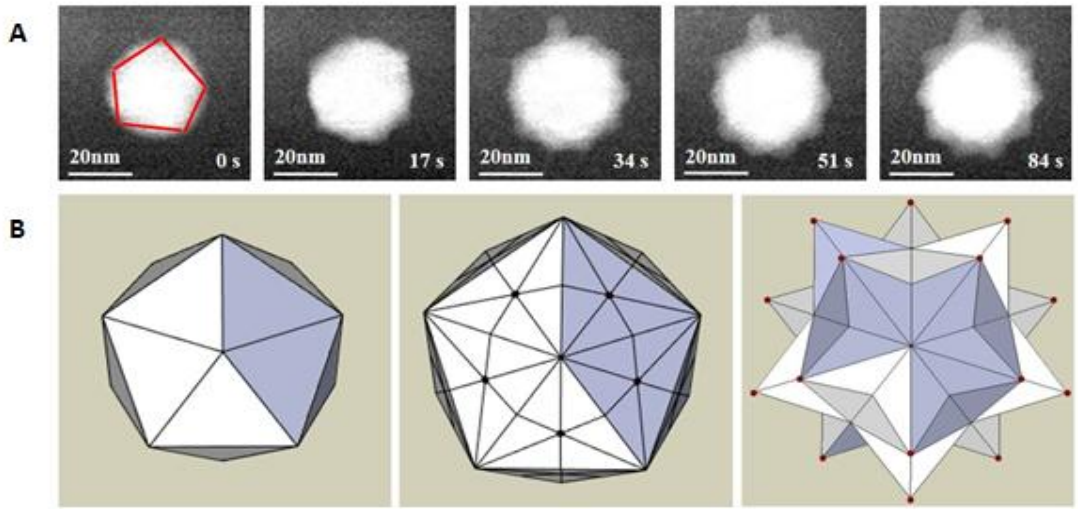

Fig 7: DMA-assisted transformation of an icosahedral seeds into a symmetric NS. (A) Time series of STEM-HAADF images acquired in methanol with DMA concentration of 0.06 mM and $\dot{d}$ = 3.4 electrons/Å^{2}s The irradiation time of the observed area is indicated in the bottom right corner of each image (B) Geometric model elucidating the transformation process via the growth of hexagonal pyramids on each triangular facet of the icosahedral seed.

After a homogenization time of 30 minutes, scanning mode imaging with a high angle annular dark field detector (STEM-HAADF) was used to activate and monitor the growth of NSs. Much higher magnifications were used for this second step to clearly reveal the formation processes. Figure 7A shows a series of STEM-HAADF images depicting the transformation of an icosahedral nanocrystal into a symmetric NS under a constant $\dot{d}$ of 3.4 electrons/Å^{2}s. Apart from a rounded protuberance, the projected NS displays 10 sharp arms that are uniformly distributed

over the seed. As described in figure 7B, the transformation mechanisms involve the growth of a pyramidal arm on each of the 20 triangular facets of the icosahedral seeds. These first *in situ* insights on NS formation confirm the stellation processes deduced from both theoretical and *ex-situ* investigations[16, 38]. Although it is challenging to unambiguously determine the faceting of the arms on *in situ* images, we considered that each of the triangular facet of icosahedron is split into six equal facets and the centre is then pulled outward in the form of hexagonal pyramid to give rise to NSs with 20 arms. This hexagonal symmetry is assumed according to the works of Niu *et al* in which DMA was also used to transform icosahedral nanoparticles into NSs[16]. The projection of this 3D structures along its 5-fold rotational axis corresponds to a star with 10 arms equidistant from each other that perfectly match the shape observed on STEM-HAADF images.

20 arms NSs were also observed along other rotational axis (Figure 8) but none of them provides a clear view of the growth process because of the proximity and overlapping of the projected arms.

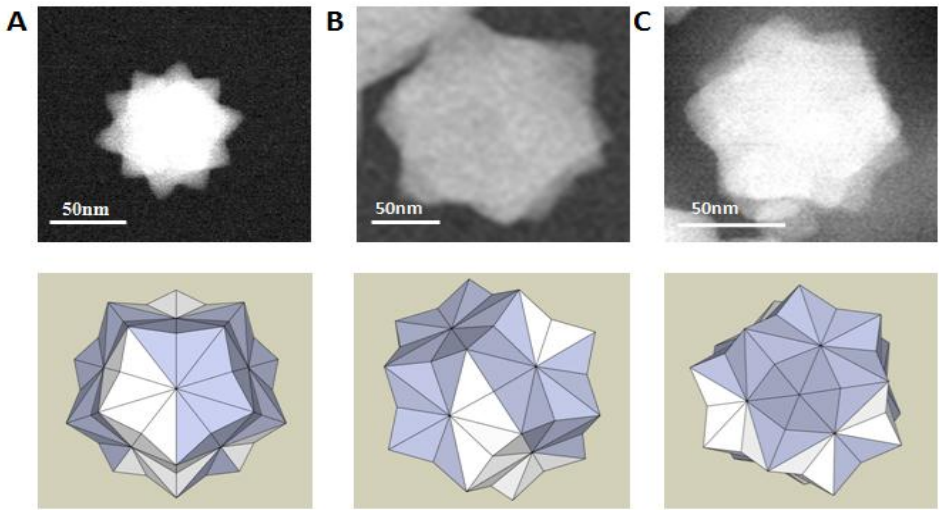

Fig 8: NSs observed along other rotational axis. Models (left) and in situ STEM-HAADF images of Au NSs along their (A) 5-fold, (B) 2-fold and (C) 3 fold rotational axes.

4.5 Effect of Seed Crystal Morphology on Final Nanostar Shape

In situ observations also reveal that seeds with rough faceting systematically lead to irregular NSs with missing or disoriented arms where seed surface is deformed (Figure 9). In line with the

concept of seed-mediated synthesis[39], these results confirm that NSs derive their excellent symmetry from the faceted morphology of the icosahedral seeds.

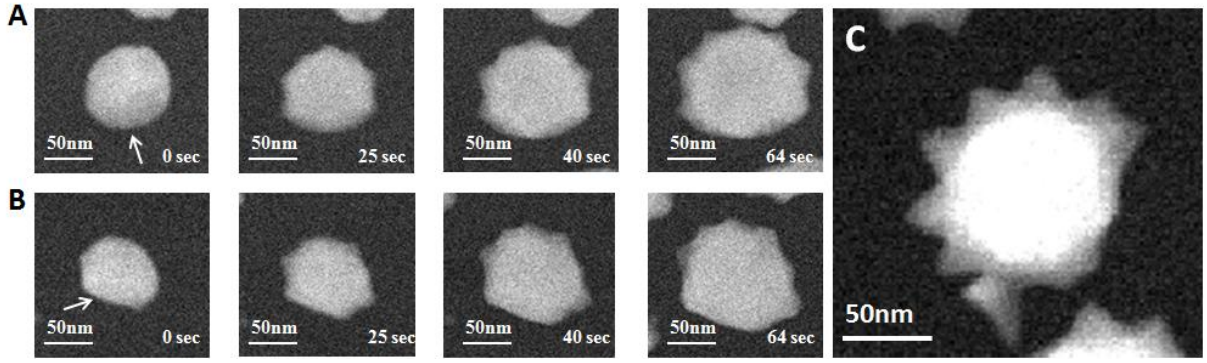

Fig 9: Formation of asymmetric NSs on seeds with deformed morphologies (A & B) Time series of STEM-HAADF images acquired in methanol with a DMA concentration of 0.06 mM and $\dot{d}$ = 0.85 electrons/Å^{2}s. The irradiation time of the observed area is indicated in the bottom right corner of each image. White arrows highlight initial defects in the faceting of the seeds that break the symmetry of the resulting NS arms. (C) In situ STEM-HAADF image of an asymmetric NS on which uniformly-distributed arms have grown on one side only.

Interestingly, decahedral seeds follow a very different growth path, since they maintain their pentagonal shape rather than transforming into stellated nanostructures (Figure 10). Given the structural differences between icosahedral and decahedral seeds,[40, 41] the influence of strain and twinned planes could possibly be a starting point of theoretical investigations to understand these different behaviours.

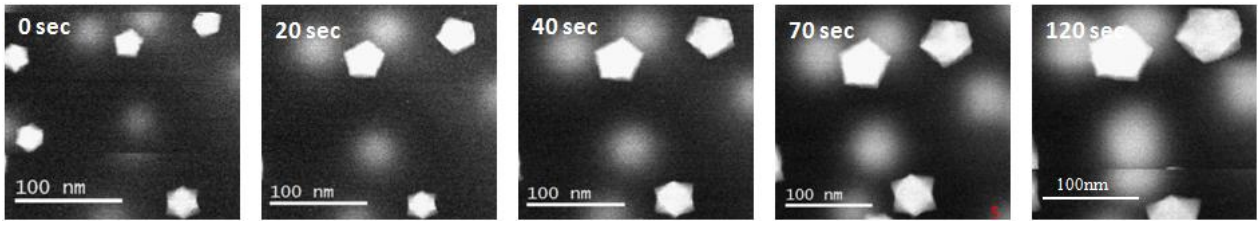

Fig 10: Growth of decahedral seeds without shape transformation. Time series of STEM-HAADF images acquired in methanol with a DMA concentration of 0.06 mM and $\dot{d}$ = 3.4 electrons/Å^{2}s. The irradiation time of the observed area is indicated in the bottom right corner of each image.

4.6 Capping Agent Concentration Impact on Nanostar Growth Kinetics & Shape Evolution

The formation of hexagonal pyramids on the top of (111) facets leads towards growth of high index facets that are normally unstable[42]. Through the entire process, alkylamines play a crucial role in modifying the surface energies of the nanostructures, hence impacting their final shapes.

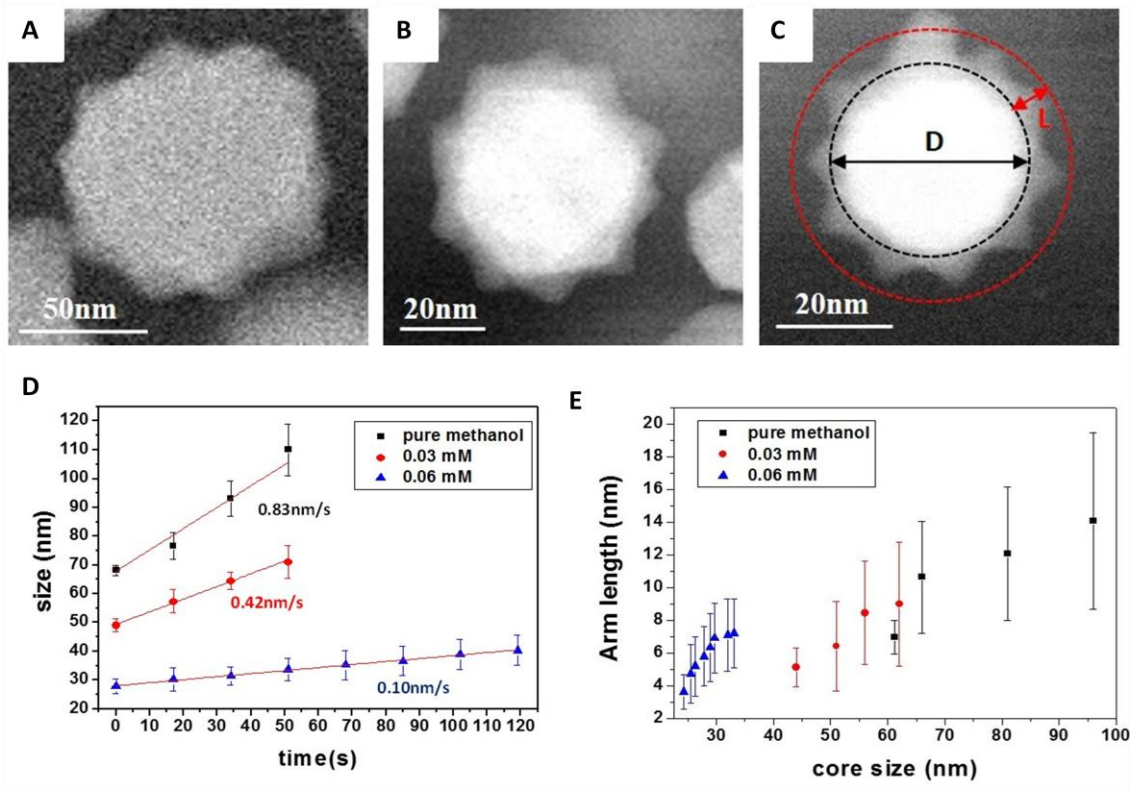

Fig 11: Effect of DMA on the growth mechanisms and final morphology of the Au NSs. In situ STEM-HAADF images showing the shape of NSs formed in the liquid-cell with a DMA concentration of (A) 0 mM (pure methanol), (B) 0.03 mM and (C) 0.06 mM. (D) Mean size of the NSs as the function of time for various DMA concentrations. The mean-growth speeds deduced from the linear fits of the data are indicated below each curve. (E) Averaged length of the NS arms (L) as a function of the averaged NS core (D) for various DMA concentrations. An example of L and D measurements is shown in (C). $\dot{d}$ = 3.4 electrons/Å^{2}s in all experiments.

To quantify the effect of DMA on the growth of gold NSs, we compared LCTEM experiments performed with similar $\dot{d}$, but with DMA concentrations of 0.06 mM, 0.03 mM and without DMA. At first, DMA concentration drastically affects the growth speed of the NSs. As observed

in figure 11D, the average growth rate of 0.83 nm/s measured without DMA is reduced by two and by eight by adding 0.03 and 0.06 mM of DMA in the reaction media, respectively. Note that these three experiments were performed on icosahedral seeds of same size. The initial size difference between the NSs at various DMA concentrations is due to the fact that significant DMA-dependent growth of the seeds had already taken place by the time the first image of the series was taken. Besides reducing the adsorption rate of gold atoms, DMA functionalization has a profound impact on the NS shape (Figure 11A-C). In particular, the tip sharpness is very sensitive to DMA concentration. This crucial feature of NS shape depends on the size of the central core (D) and the length of the arms (L) that both increases during the growth of the nanostructure. Indeed, the higher the L/D ratio, the sharper the tips. The evolution of L as a function of D observed in figure 11E reveals that DMA slow-downs much more the growth of the core than the expansion of the arms, leading to shaper and smaller NSs. Furthermore, DMA also improves shape uniformity since the relative dispersion of arm lengths is halved when DMA concentration is doubled.

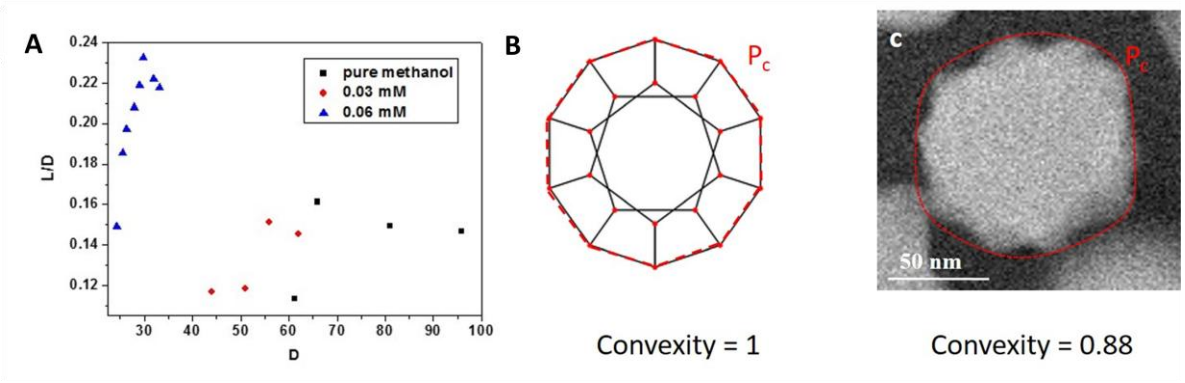

Fig 12: Effect of DMA on the growth mechanisms and final morphology of the Au NSs. (A) Ratio between the mean length of the NS arms (L) and the mean size of the NS core (D) as a function of D for various DMA concentrations. Comparing the shape of NSs obtained in pure methanol with regular dodecahedron. The convexity is defined as the ratio of the convex hull perimeter (P_c) (i.e. convex envelope) by the actual perimeter (P). Therefore, P_c and P differ when the projected image of a particle presents concave sections. (B) Regular dodecahedron with its orthogonal projection centered on a pentagonal facet, Pc = P and convexity = 1. (C) NS obtained in pure methanol with a convexity of 0.88.

These *in situ* analyses also reveal that in all synthesis conditions, the L/D ratio (i.e. the nanostar sharpness) reaches a maximum and then slightly decreases in subsequent growth periods (Figure

12A), highlighting a size effect on the ability of DMA to favor the expansion of the arms with respect to the growth of the core.

Although these results clearly demonstrate the role of DMA in stabilizing sharp NSs, the formation of large NSs with very short arms in absence of DMA in the liquid-cell remains unexpected. Indeed, according to Niu et al[16], without alkylamines icosahedral nanoparticles should transform into dodecahedral particles. With its orthogonal projection centered on a pentagonal facet, the projected shape of an octahedron has a 5 fold symmetry that is rather similar to the projected shape of a NSs with very short arms (Figure 12B). Nevertheless, NSs obtained without any DMA have a convexity (i.e. convex hull perimeter divided by the actual perimeter) 12 % lower than the one expected for regular dodecahedron, on account of the presence of arms creating concave surface sections (Figure 12C). We assume that the formation of these arms is due to the presence of traces of DMA within the liquid cell. Indeed, this secondary amine is usually produced by reaction of ammonia and methanol. Thus, during our experiments, methanol could possibly react with amine groups present on the SiN windows or with traces of ammonia since this chemical product is used during the fabrication process of the liquid-cell.

4.6.1 Stability of Au Nanostars in Solution

High index facets are essentially low coordinated surfaces with a high density of kinks, steps and edges[42]. Such surface structures are desired traits for catalytic applications because they provide highly reactive sites[43]. However it also makes the long-term stabilisation of gold NSs challenging because of their poor stability. Besides revealing the growth process of nanomaterials, LCTEM also provides the unique opportunity to know the full fate of nanostructures in their formation media. We observed that shutting down the electron beam for a few minutes results in a complete reshaping of the NSs due to the surface diffusion of gold atoms from the tips to the concave surfaces (Figure 13A). This common diffusion process is also observed during sintering phenomena[44] in which the migration of atoms is driven by the differences in chemical potential of surfaces with varying degree of curvatures[39]. By shutting down the electron beam we effectively cut off the supply of Au monomers to the growing NSs and also change the pH of the solution. The reshaping process is then driven by the need to reduce the overall surface energy *via* the reduction of surface area.

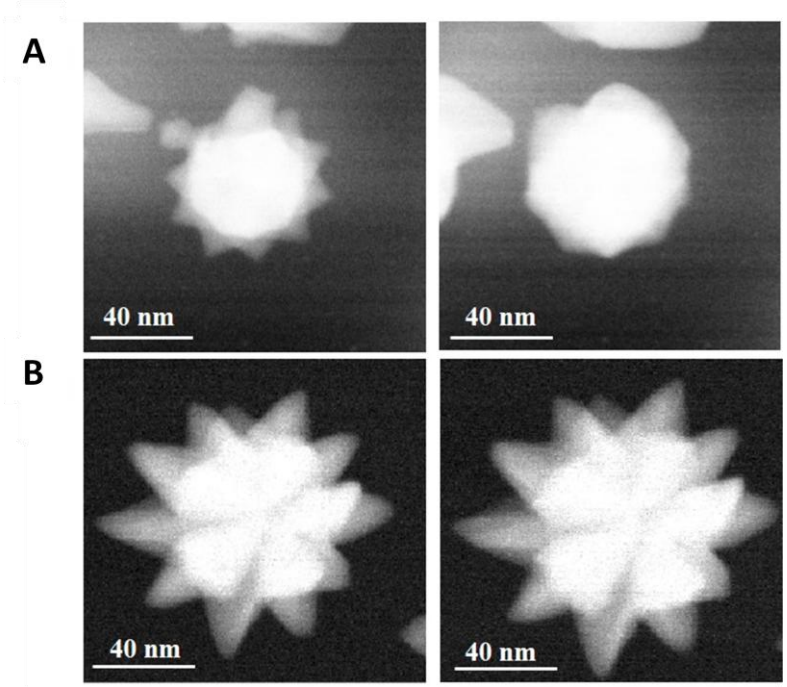

Fig 13: Stability of NSs as a function of DMA concentration. STEM-HAADF images acquired before (left images) and after (right images) a time (t) with no electron irradiation. (A) DMA concentration of 0.06 mM and t = 4 minutes. (B) DMA concentration of 0.2 mM and t = 7 minutes.

It also highlights the inability of DMA to prevent surface atom diffusion when low-concentrations of capping agent are used. Note that this transition regime in which DMA drives the formation of NSs but cannot maintain their shape when the growth stops could not be revealed by analysing *ex situ* snapshots of the nanomaterials extracted from their formation medium at given time points of the synthesis. Interestingly, increasing the DMA concentration prolongs the reshaping time and can even ensure the long term stability of NSs when the concentration reaches 0.2 mM (Figures 13B and 14). In line with the established stabilizing role of capping agent[39], these *in situ* observations perfectly illustrate the direct link between the surface-energy equilibrium of Au NSs and the amount of capping agents on their surface. Increasing DMA concentration in the liquid-cell has also the practical advantage that the formation of NSs can be monitored with much higher magnification.

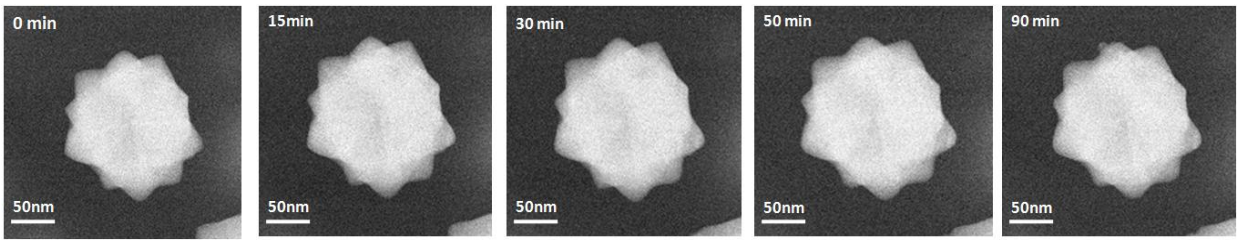

Fig 14: Stability of a NS formed in methanol with DMA concentration of 0.2mM. Series of in situ STEM HAADF images acquired in the growth media after the formation of the NS. The waiting period during which the liquid-cell was not irradiated by the electron beam is indicated in the top left corner of each image (the electron beam was switched on for only 5 seconds intermittently to acquire the images). There is no discernible change in the shape of the NS after 30 minutes and a slight rounding of the NS arms is observed after 90 minutes.

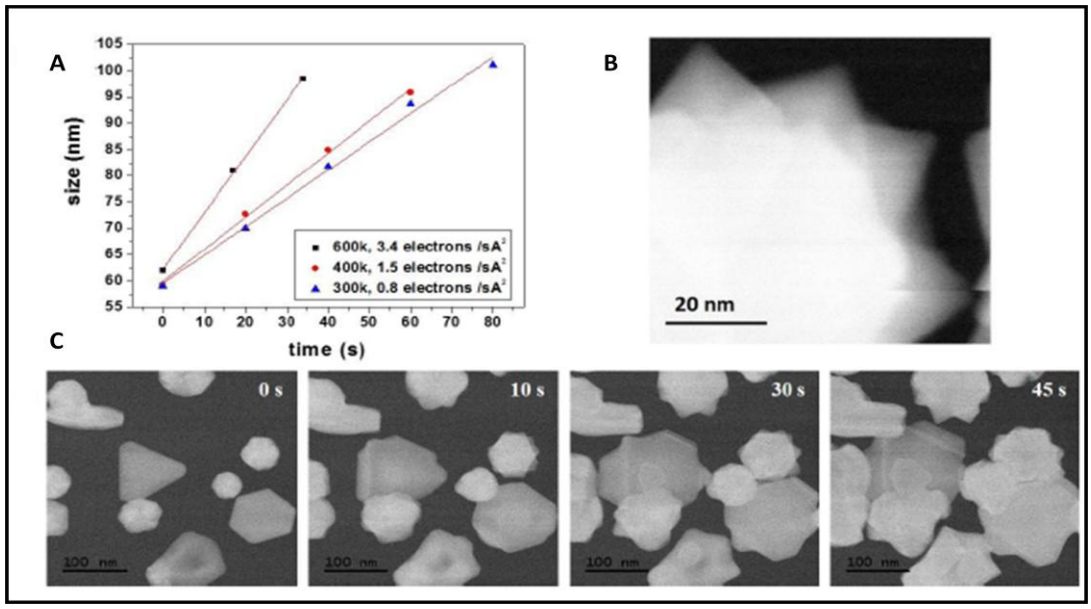

Fig 15: (A) Mean size of the NSs as the function of time for various magnification (i.e. various $\dot{d}$). Data obtained with no DMA in the growth media. (B) STEM HAADF image acquired during the growth of a NS in growth media with 0.06 mM of DMA (magnification of 1500k and $\dot{d}$ = 21 electrons/Å^{2}s). (C) Time series of STEM HAADF images illustrating that high magnification observation (600k) in a growth media with no DMA leads rapidly to the coalescence of nanoparticles. These fast growth processes inhibit the acquisition of clear high magnification pictures of NSs. The irradiation time of the observed area is indicated in the top right corner of each image.

Indeed, as the growth speed increases with $\dot{d}$ (Figure 15A)[21], increasing the magnification of STEM imaging leads to growth processes dominated by kinetic effects in which the nanoparticles cannot reach well-facetted morphology and tends to rapidly coalesce because of the very high flow of adsorbed monomers (Figure 15C). By reinforcing the stability of Au NSs and reducing the adsorption rate of gold atoms, DMA allows studying the morphology of isolated NSs with magnification up to 1 500 k (Figure 15B).

4.7 Critical Aspects of Nanostar Growth Mechanism

Finally, we want to shed light on a peculiar feature of NS formation which could not be emphasised without dynamical *in situ* imaging. The habit of a crystal is determined by the relative rates at which different crystal planes grow. Thus, the faster growing facets (i.e. the more attractive for ad-atoms) are usually eliminated at the expense of slow growing ones[39]. This faceting process is well exemplified by the transformation of a 2D nanoprisms into a 2D hexagonal nanoplate observed in pure methanol (Figure 16).

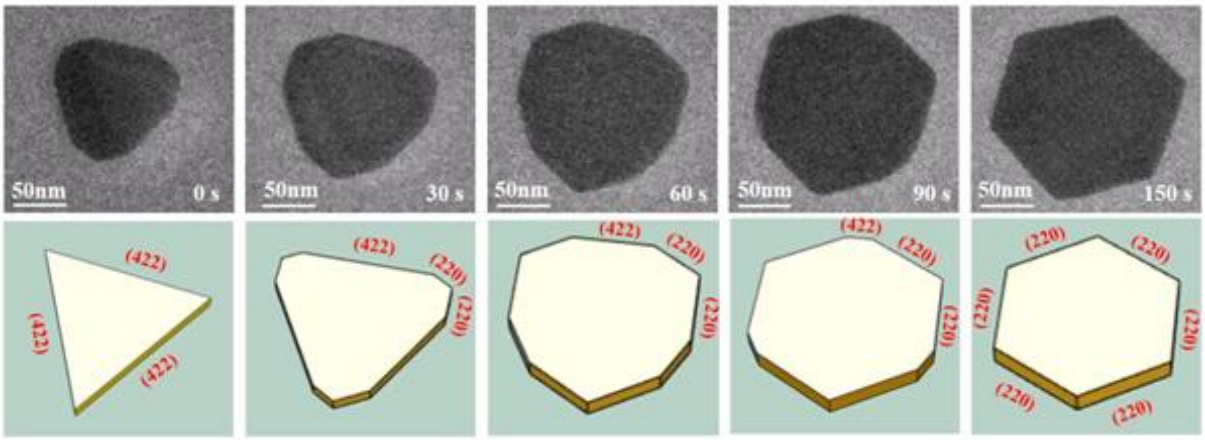

Fig 16: Time series of TEM images showing the transformation of a nanoprism into a hexagonal nanoplate in pure methanol. The irradiation time of the observed area is indicated in the bottom right corner of each image. The geometric models below the experimental images highlight the transformation process: the reshaping of the nanoprism corners creates six (220) edges that expand rapidly at the expense of the (422) edges because of the highest growth rate of the nanoprism along the [422] directions.

The initial nanoprisms always exhibit three (422) edges but the reshaping of the nanoprism corners lead to the formation of six (220) edges. Thereafter, Au monomers attach preferentially to

the (422) edges that grow rapidly out of existence leading to hexagonal nanoplates terminated with (220) edges. Interestingly, the transformation of gold nanoprisms in water systematically follow a different pathway ending with hexagonal nanoplates with 6 (422) edges (Figure 17).

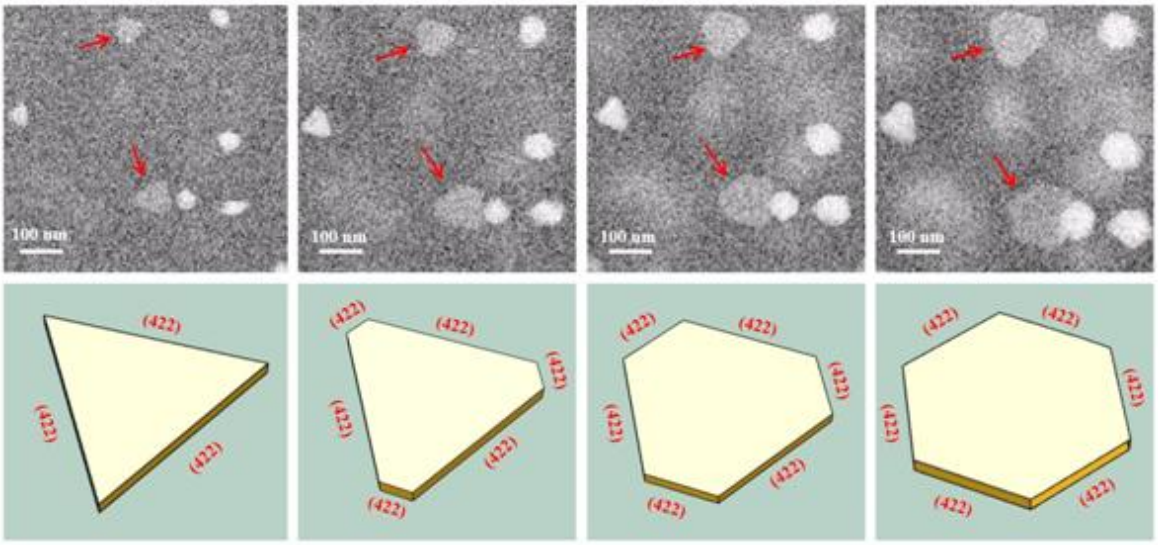

Fig 17: Time series of STEM-HAADF images showing the transformation of a nanoprism into a hexagonal nanoplate with $\dot{d} < 10^{-2}$ electrons/Å^{2}s. In pure water, the reshaping of the nanoprism corners creates three new (422) edges that are parallel to the opposite sides of the triangle. The growth rate along the six [422] directions is then equivalent leading to the formation of quasi-regular hexagonal plate.

Note that the edge indexes were deduced from *ex situ* HRTEM experiments described in figure 6C, but they do not correspond to the indexes of the side-faces which are usually a mix of (111) and (100) planes dictated by the planar-defect configuration [31, 33, 45]. In fact, as the growth rate of the nanoplate edges depends on the side-face structure[45, 46], monitoring the growth processes in cross-section view would provide a deeper understanding of these faceting mechanisms and the impacts of solvents.

According to this very common view of crystal growth, the shape of NSs should depend on the competition between the growth of a given high-index facet, with (hkl) that would depend on DMA concentration and the growth of the (111) facets of the icosahedral seed. Therefore, NSs with apexes truncated by (111) planes should be observed during the transformation of an icosahedral seed into a NSs enclosed by high-index facets. Surprisingly, nanoscale *in situ* imaging reveals that NSs display sharp tips through the whole growth process of their arms and

the expected truncation of these arms is never observed. In fact, the growth of the pyramidal arms on each triangular facet of the seeds goes through a continuous increase of the distance between the apex and the base of the pyramids (Figure 18).

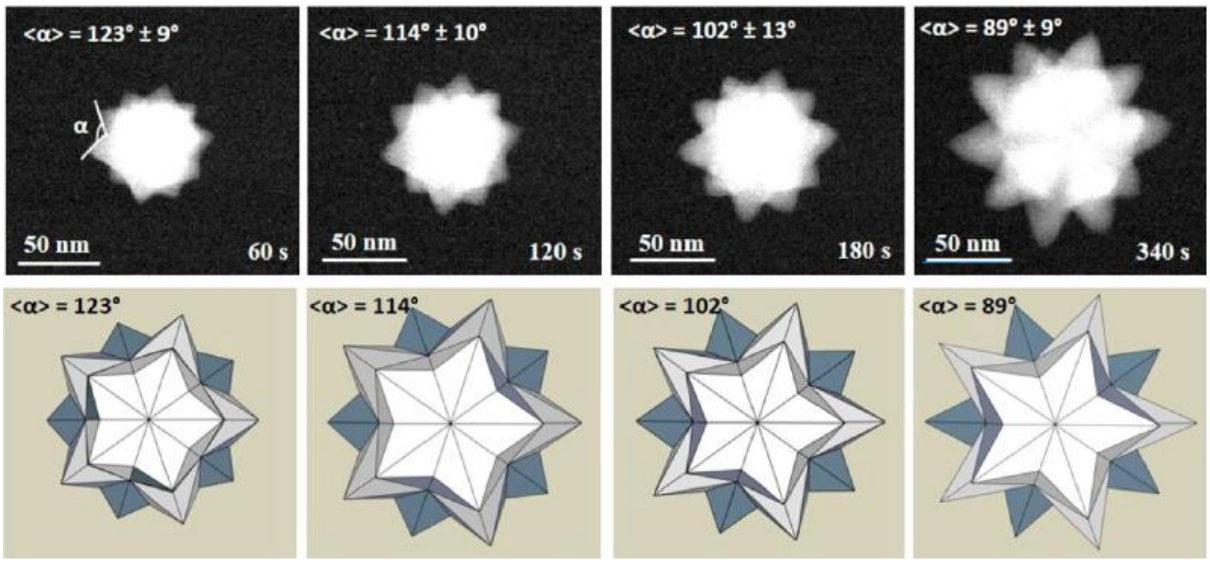

Fig 18: Growth mechanisms of Au nanostars. Time series of STEM-HAADF images showing the growth of a NS in methanol with a DMA concentration of 0.2 mM and $\dot{d}$ = 6 electrons/Å^{2}s. The irradiation time of the observed area and the means inter-arm angle (<α>) are indicated in the bottom right corner and the top left corners of each image, respectively. The geometric models below the experimental images highlight the transformation process: the growth rate of the 20 pyramidal arms is higher along the tip direction than along the basal plane leading to a sharpening of the arms and to a decrease of <α>.

This stellation process systematically observed in all growth conditions, implies that the indexes of NS facets continuously changes during the formation of the arms, as it is evidenced by the continuous reduction of the mean inter-arms angle during NS growth (Figure 18). Given the dispersion of inter-arm angles that is always experimentally observed and the resemblance of NSs enclosed by facets with close (hkl) indexes, it is difficult to unambiguously determine the crystal planes at the NS surface by comparing electron microscopy images with theoretical NS shapes[16]. Like the tip sharpness, the final indexes of the facets enclosing a NSs will depend on the growth time and on the competition between the expansion of the arms and the growth of the NS core which induces a widening of the triangular base of the arms. This fresh look at the formation of nanostructures with high-index facets indicates that DMA likely enhances the surface diffusion

and the mobility of kinks, steps and edges that are necessary to continuously change crystal facets. These first insights have the potential to motivate further experimental and theoretical investigations on this keystone process of NS growth.

4.8 Conclusion

In this chapter liquid-cell TEM has been exploited to explore the growth mechanisms of gold NSs in methanol. These *in situ* investigations reveal that the symmetry of the NSs is directly related to the faceting of the initial seeds. We observed the formation of highly symmetric NSs *via* the growth of pyramidal arms on the 20 facets of icosahedral seeds. Besides confirming the efficiency of DMA to stabilise sharp NSs terminated by high-index facets, we show that the shape of NSs is driven by the competitive growth of the core and the arms of the stellated nanostructures. Interestingly, the expansion of the arms involves a continuous and very dynamic restructuring of crystal surfaces which emphasise the crucial role of DMA in the surface diffusion processes leading to the formation of high-index facets. More generally, this work shed light on the unique potential of LCTEM to study sophisticated synthesis protocols, combining both seed and functionalization-mediated strategies.

.

.

References

1. Grzelczak, M.; Perez-Juste, J.; Mulvaney, P.; Liz-Marzan, L. M. *Chem. Soc. Rev.* **2008,** 37, 1783-1791.
2. Sau, T. K.; Murphy, C. J. *J. Am. Chem. Soc.* **2004,** 126, 8648-8649.
3. Daniel, M.-C.; Astruc, D. *Chem. Rev.* **2004,** 104, 293-346.
4. Eustis, S.; El-Sayed, M. A. *Chem. Soc. Rev.* **2006,** 35, 209-217.
5. Li, N.; Zhao, P.; Astruc, D. *Angew. Chem., Int. Ed.* **2014,** 53, 1756-1789.
6. Chirico, G.; Borzenkov, M.; Pallavicini, P., *Gold Nanostars: Synthesis, Properties and Biomedical Application*. Springer: 2015.
7. Nehl, C. L.; Liao, H.; Hafner, J. H. *Nano Lett.* **2006,** 6, 683-688.
8. Liu, Y.; Yuan, H.; Fales, A.; Register, J.; Vo-Dinh, T. *Front. Chem.* **2015,** 3.
9. Rodríguez-Lorenzo, L.; de la Rica, R.; Álvarez-Puebla, R. A.; Liz-Marzán, L. M.; Stevens, M. M. *Nat. Mater.* **2012,** 11, 604-607.
10. Rodríguez-Lorenzo, L.; Álvarez-Puebla, R. A.; Pastoriza-Santos, I.; Mazzucco, S.; Stéphan, O.; Kociak, M.; Liz-Marzán, L. M.; García de Abajo, F. J. *J. Am. Chem. Soc.* **2009,** 131, 4616-4618.
11. Hrelescu, C.; Sau, T. K.; Rogach, A. L.; Jäckel, F.; Laurent, G.; Douillard, L.; Charra, F. *Nano Lett.* **2011,** 11, 402-407.
12. Li, M.; Kang, J. W.; Dasari, R. R.; Barman, I. *Angew. Chem.* **2014,** 126, 14339-14343.
13. Schütz, M.; Steinigeweg, D.; Salehi, M.; Kömpe, K.; Schlücker, S. *Chem. Commun.* **2011,** 47, 4216-4218.
14. Guerrero-Martínez, A.; Barbosa, S.; Pastoriza-Santos, I.; Liz-Marzán, L. M. *Curr. Opin. Colloid Interface Sci.* **2011,** 16, 118-127.
15. Pallavicini, P.; Cabrini, E.; Borzenkov, M., Gold Nanostar Synthesis and Functionalization with Organic Molecules. In *Gold Nanostars*, Springer: 2015; pp 1-23.
16. Niu, W.; Chua, Y. A. A.; Zhang, W.; Huang, H.; Lu, X. *J. Am. Chem. Soc.* **2015,** 137, 10460-10463.
17. Williamson, M. J.; Tromp, R. M.; Vereecken, P. M.; Hull, R.; Ross, F. M. *Nat. Mater.* **2003,** 2.
18. Liao, H. G.; Niu, K. Y.; Zheng, H. M. *Chem. Commun.* **2013,** 49, 11720-11727.
19. Ngo, T.; Yang, H. *J. Phys. Chem. Lett.* **2015,** 6.
20. Ahmad, N.; Le Bouar, Y.; Ricolleau, C.; Alloyeau, D. *Adv. Struct. Chem. Im.* **2016,** 2, 9.
21. Alloyeau, D.; Dachraoui, W.; Javed, Y.; Belkahla, H.; Wang, G.; Lecoq, H.; Ammar, S.; Ersen, O.; Wisnet, A.; Gazeau, F.; Ricolleau, C. *Nano Lett.* **2015,** 15, 2574-2581.
22. Woehl, T. J.; Evans, J. E.; Arslan, I.; Ristenpart, W. D.; Browning, N. D. *Acs Nano* **2012,** 6, 8599-8610.
23. Jungjohann, K. L.; Bliznakov, S.; Sutter, P. W.; Stach, E. A.; Sutter, E. A. *Nano Lett.* **2013,** 13, 2964-2970.
24. Wu, J.; Gao, W.; Wen, J.; Miller, D. J.; Lu, P.; Zuo, J.-M.; Yang, H. *Nano Lett.* **2015,** 15, 2711-2715.
25. Liao, H.-G.; Zherebetskyy, D.; Xin, H.; Czarnik, C.; Ercius, P.; Elmlund, H.; Pan, M.; Wang, L.-W.; Zheng, H. *Science* **2014,** 345, 916-919.
26. Baxendale, J. H.; Wardman, P., *The Radiolysis of Methanol: Product Yields, Rate Constants, and Spectroscopic Parameters of Intermediates*. National Bureau of Standards: 1975.
27. Ferradini, C.; Jay-Gerin, J. P. *Radiation Physics and Chemistry* **1996,** 48, 473-480.
28. Barnard, A. S.; Young, N. P.; Kirkland, A. I.; van Huis, M. A.; Xu, H. *Acs Nano* **2009,** 3, 1431-1436.
29. Ling, T.; Xie, L.; Zhu, J.; Yu, H.; Ye, H.; Yu, R.; Cheng, Z.; Liu, L.; Liu, L.; Yang, G.; Cheng, Z.; Wang, Y.; Ma, X. *Nano Lett.* **2009,** 9, 1572-1576.
30. Zhang, Q.; Xie, J.; Yang, J.; Lee, J. Y. *Acs Nano* **2009,** 3, 139-148.
31. Germain, V.; Li, J.; Ingert, D.; Wang, Z. L.; Pileni, M. P. *J. Phys. Chem. B* **2003,** 107, 8717-8720.
32. Kirkland, A. I.; Jefferson, D. A.; Duff, D. G.; Edwards, P. P.; Gameson, I.; Johnson, B. F. G.; Smith, D. J. *Proc. R. Soc. London Ser. A-Math. Phys. Eng. Sci.* **1993,** 440, 589-609.

33. Le Beulze, A.; Duguet, E.; Mornet, S.; Majimel, J.; Treguer-Delapierre, M.; Ravaine, S.; Florea, I.; Ersen, O. *Langmuir* **2014,** 30, 1424-1434.
34. Berriman, R. W.; Herz, R. H. *Nature* **1957,** 180, 293-294.
35. Goessens, C.; Schryvers, D.; Vanlanduyt, J.; Amelinckx, S.; Verbeeck, A.; Dekeyzer, R. *J. Cryst. Growth* **1991,** 110, 930-941.
36. Lofton, C.; Sigmund, W. *Adv. Funct. Mater.* **2005,** 15, 1197-1208.
37. Liao, H.-G.; Shao, Y.; Wang, C.; Lin, Y.; Jiang, Y.-X.; Sun, S.-G. *Mater. Lett.* **2014,** 116, 299-303.
38. Burt, J. L.; Elechiguerra, J. L.; Reyes-Gasga, J.; Martin Montejano-Carrizales, J.; Jose-Yacaman, M. *J. Cryst. Growth* **2005,** 285, 681-691.
39. Xia, Y. N.; Xiong, Y. J.; Lim, B.; Skrabalak, S. E. *Angew. Chem.-Int. Edit.* **2009,** 48, 60-103.
40. Hofmeister, H., Shape variations and anisotropic growth of multiply twinned nanoparticles. In *Zeitschrift für Kristallographie International journal for structural, physical, and chemical aspects of crystalline materials*, 2009; Vol. 224, p 528.
41. Patala, S.; Marks, L. D.; Olvera de la Cruz, M. *J. Phys. Chem. C* **2013,** 117, 1485-1494.
42. Quan, Z.; Wang, Y.; Fang, J. *Acc. Chem. Res.* **2013,** 46, 191-202.
43. Zhou, Z.-Y.; Tian, N.; Li, J.-T.; Broadwell, I.; Sun, S.-G. *Chem. Soc. Rev.* **2011,** 40, 4167-4185.
44. Alloyeau, D., Transmission Electron Microscopy: A Multifunctional Tool for the Atomic-scale Characterization of Nanoalloys. In *Nanoalloys: synthesis, structure and properties*, Alloyeau, D.; Mottet, C.; Ricolleau, C., Eds. Springer London: 2012; pp 113 - 157.
45. Bogels, G.; Meekes, H.; Bennema, P.; Bollen, D. *J. Cryst. Growth* **1998,** 191, 446-454.
46. Bogels, G.; Pot, T. M.; Meekes, H.; Bennema, P.; Bollen, D. *Acta Crystallogr. Sect. A* **1997,** 53, 84-94.

Chapter 5

Reversible Redox Reactions at Solid / Liquid Interfaces Driven by Electron Beam of a Transmission Electron Microscope

In this last chapter chemical reactions at the interface between solids and liquids were investigated. It is shown here that the electron beam can be used to drive reversible deposition / dissolution cycles of copper shells over gold nanoparticles in methanol. Besides revealing the influence of irreversible processes on the kinetic of growth/etching cycles, this study of nanostructure behavior as a function of the dose rate highlights the possibility to switch the oxidizing or reducing nature of liquid environment only with the electron beam. The chemical and electronic processes possibly involved in these tunable redox reactions are qualitatively discussed together with their possible impacts on electrochemical LCTEM experiments.

5.1 Key Aspects of Redox Reactions in Materials Sciences

The redox reactions ruling the deposition or dissolution of matter at the interfaces between liquids and solids play a key role in the conception, the use and life-cycle of materials in their application media. Since the advent of liquid-cell transmission electron microscopy (LCTEM), there has been a great desire to study such growth or dissolution processes at the nanoscale, notably to provide a better understanding of nanomaterial synthesis[1, 2], mass transport in electrochemical cells[3, 4] and materials corrosion[5-7]. Nevertheless, a critical parameter in interpreting LCTEM data is to take into account the effects of the electron beam, because the strong oxidizing and reducing species that are generated by radiolysis can obviously disturb nanoscale *in situ* studies in liquid[8-10]. As already described in the preceding chapters two strategies are employed to deal with the beam effects in LCEM experiments. Predominantly LCTEM studies tends to reduce the steady-state concentration of radiolysis products by using low dose rate to monitor dynamical phenomena that are then minimally affected by these chemical

modifications. This strategy was for instance, employed for studying the electrochemically-induced deposition and dissolution of Li on electrodes during charge/discharge cycling of battery[11, 12]. The second approach consists in exploiting radiolysis processes to drive the redox reactions leading to material transformations. Thus, the dose rate and the cumulative dose become meaningful parameters that have been successfully exploited to control and to study kinetic effects on the formation of metallic nanoparticles[13-15].

5.2 Tuning the Redox Environment in LCTEM

The chemical environment in a liquid cell can be specifically adjusted for a particular experiment by creating conditions which are conducive to either nanoparticles growth or degradation. The fields of radiation chemistry and LCEM have successfully exploited several strategies to obtain desired chemical environment.

5.2.1 Modifying Redox Environment by Means of Solution Chemistry

It is worth noting that the reduction of metallic precursors by radiologically-produced solvated (or hydrated) electrons continuously compete with oxidative reaction that may lead to the degradation of nanomaterials. This competition between very opposite chemical pathways can be tuned by intentionally modifying solution chemistry with radical scavengers, complexing agents or by changing the solvent or its pH[9]. As in water radiolysis several strong reducing and oxidizing species are simultaneously produced hence one of these strategies can be employed with certain advantages and disadvantages. Radical scavengers offer the unique advantage of specifically targeting a particular radical e.g alcohols like isopropanol reacts with the highly oxidizing $OH^{\bullet}$ (rate constant: $k > 10^9\ M^{-1}s^{-1}$) and thus creates a unique reducing environment since their reactivity with solvated electrons (e_s) is much less ($k < 10^5\ M^{-1}s^{-1}$)[16, 17]. In addition to scavengers, additives can be added such as halides (Cl^-, I^-, Br^-) which can modify the oxidizing power of $OH^{\bullet}$ and make it more selective since it attacks any chemical bond. As well as the aforementioned changes in solution chemistry, the pH of solution can be modified which alters the concentrations of primary and secondary reactions. This can have significant implications for the nanoparticle stability[18]. Lastly since most LCTEM experiments lie in a regime of low solute concentration (< 0.1 M) hence the radiochemistry of the solvent is the important criteria for understanding reaction kinetics[19]. In this regard choosing the type of solvent (aqueous, organic,

aromatic….) for a particular experiment is of utmost importance. Abellan et al[20]. recently demonstrated the use of aromatic hydrocarbon (toluene) for synthesis of palladium nanoparticles. It was shown in their study that the solvent was very resistant to irradiation damage at high electron doses and formulated a net reducing environment without the addition of any scavengers. The application of these strategies to control the liquid environment is fast becoming an integral part of LCTEM experiments.

5.2.2 Manipulation of Redox Environment by Electron Beam

Kinetic models taking into account the volumetric production rates of radiolysis products in water, their destruction and production through chemical reactions and their diffusion, demonstrated that the steady state concentrations of radicals in the irradiated area increases with the electron dose rate with power-law behaviors (Schneider et al[21].). The scaling of radical concentrations is not uniform. Some radicals scale linearly with the dose rate while others scale quadratically[22]. This results in relative changes in the steady state concentrations of reducing and oxidizing radicals at various dose rates. However, understanding the role of the electron irradiation in this complex equilibrium remains much more complicated because of the many possible interactions between the beam and the environment and their resulting reactions. One such factor is the role of LCTEM membranes. These membranes can contribute to radiolysis processes as these are an additional source of secondary electron. As well as this the membranes can affect the chemical diffusion profile of reactants near the growing nanoparticles[23]. Due to these complex constraints it is only possible to qualitatively study redox phenomenon by this approach.

In the following passages, we report a simple LCTEM study in which the electron dose rate is used to control reversible cycles of deposition / dissolution of copper over gold nanoparticles in methanol. This study conducted with minimal modifications of the solution chemistry provides direct evidence of the electron-beam impacts on the chemical nature of the liquid environment.

5.3 Experimental Protocol

The formation of the gold-copper nanostructures was realized in two steps. First experiment was performed in a methanol solution containing 1 mM of Gold (III) chloride trihydrate to grow gold nanostructures on the SiN membranes. Then, the liquid-cell was unsealed, rinsed in pure

methanol, dried and reused for a second experiment with methanol containing 1 mM of Cu(II) acetylacetonate ($Cu(acac)_2$). The microfluidic system of the sample holder was also abundantly flushed with pure methanol between the two steps. For these two steps, sample preparation was done by depositing a 2.4 µl droplet of Au or Cu precursors in methanol on the small e-chip. The accelerating voltage during all experiments was maintained at 200 kV. A 5 µL/min flow of methanol containing 1 mM of Au precursors (first step) or 1 mM of Cu precursors (second step) was continuously injected in the liquid-cell. LCTEM imaging was performed in scanning mode on a High Angular Annular Dark Field detector (STEM – HAADF) with a pixel dwell time of 5 µs.. STEM imaging was mostly performed on the top e-chip (the small one in the JEOL ARM microscope) to improve image resolution and quality.

5.3.1 Synthesis of Au Nanostructures (1st Stage)

As a first step, a low-dose LCTEM experiment was conducted to form gold nanoparticles on the SiN membranes of the liquid-cell (Figure 1). Chloroauric acid diluted in methanol was imaged in STEM-HAADF mode with dose rate ranging from $4.1*10^{-3}$ to $3.7*10^{-2}$ electrons/Å^{2}s (magnification from 50k to 150k). For the growth of gold nanoparticles, small probe size (8c) and small condenser aperture (50 µm in diameter) were used to reduce the beam current to 1.5 pA. As previously mentioned, low-dose conditions induce the formation of 2D platelets with triangular and hexagonal forms, together with 3D facetted nanoparticles with much brighter contrast on the STEM-HAADF images because of their higher thickness (Figure 1).

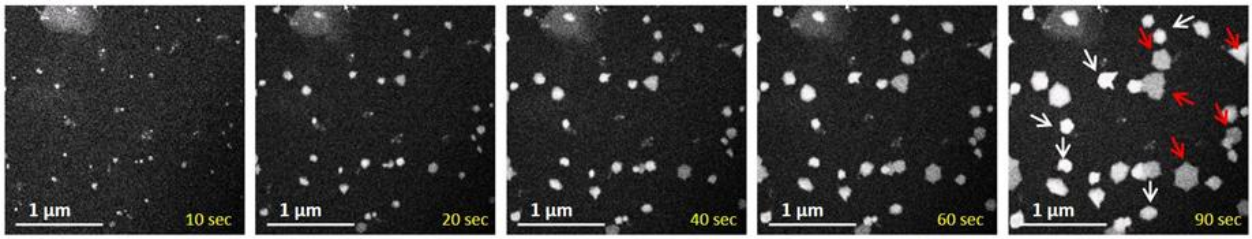

Fig 1: Growth of gold nanoparticles by radiolysis in methanol. (a) Au nanoparticles growth monitored by STEM HAADF with a magnification of 80 k (dose rate = 10^{-2} electrons/Å^{2}s). Some 3D and 2D nanoparticles are indicated by white and red arrows, respectively. The irradiation time is indicated in the bottom right corner of each image.

5.3.2 Formation of Copper shells (2nd stage)

After forming several patches of Au nanoparticles on the SiN membranes, the liquid cell was unsealed, rinsed with methanol and dried to make sure it was clean from gold precursors for the second step of the experiments. The same liquid-cell was sealed again and LCTEM experiment was carried out to form Cu shells over the Au nanoparticles remaining on the SiN membranes. As in a first step, the metallic complexes are most likely reduced by solvated electrons (and probably by $H^{\bullet}$ also produced by radiolysis of methanol). For the growth of copper on gold nanoparticles the beam current was increased up to 8.4 pA by using a larger probe size (5c).

5.4 Radiochemistry of Methanol

The main primary products of methanol radiolysis are solvated electrons (e_s) and $CH_3O^{\bullet}$ radicals[24, 25]. These strong reducing and oxidizing species are equivalent to the aqueous electrons (e_{aq}) and the hydroxyl radicals ($OH^{\bullet}$) formed during the radiolysis of water, respectively. Solvated electrons most likely reduce gold precursors leading to the nucleation and growth of Au nanoparticles. Radiolysis of methanol typically produces a reducing environment however one way to modify chemical environment is by introducing various complexing agents. In the presence of such complexing agents such as halides, the regime can change from net reducing to net oxidizing[19, 26].

5.5 Growth/Etching Dynamics of Copper Shells over Au Nanoparticles

In all the areas studied, Cu-layer growth systematically starts for dose rate above 6.1 electrons/$Å^2$s (magnification of 800k). Interestingly, Cu deposition only occurs on the gold nanoparticles and not on the SiN membranes (Figure 2A). This localized growth mechanisms could be explained by a higher chemical affinity of Cu monomers for capping-agent-free gold surfaces than for amorphous SiN or by a catalytic effect of the gold surfaces since the reduction potential of metal ions can be increased upon adsorption on nanoparticles[27].

Interestingly, Hu et al[28]. theoretically demonstrated that $Cu(acac)_2$ can chemisorbs on metal surfaces and decomposes easily into a Cu atom and acac-ligands *via* a sequential dissociation and reduction of the Cu ion. It has been also proposed that the many secondary electron generated by

irradiated metallic interfaces can locally increase the energy absorbed by the solvent[21]. The resulting enhancement of radiolytic Cu growth would then be confined at the vicinity of the Au nanoparticles, because of the short mean free path of secondary electrons. Cu deposition follows a Volmer-Weber growth mode[29], consisting in the nucleation of small 3D clusters on the Au surfaces that rapidly grow and coalesce to form rough layers over all the 2D or 3D gold nanoparticles present in the irradiated area. Full covering of the Au surface with 50 nm thick Cu layers was obtained in less than a minute. Surprisingly, as soon as the electron dose rate was reduced down to 1.5 electrons/Å^{2}s (magnification 400k), the rapid dissolution of these Cu films was observed (figure 2B).

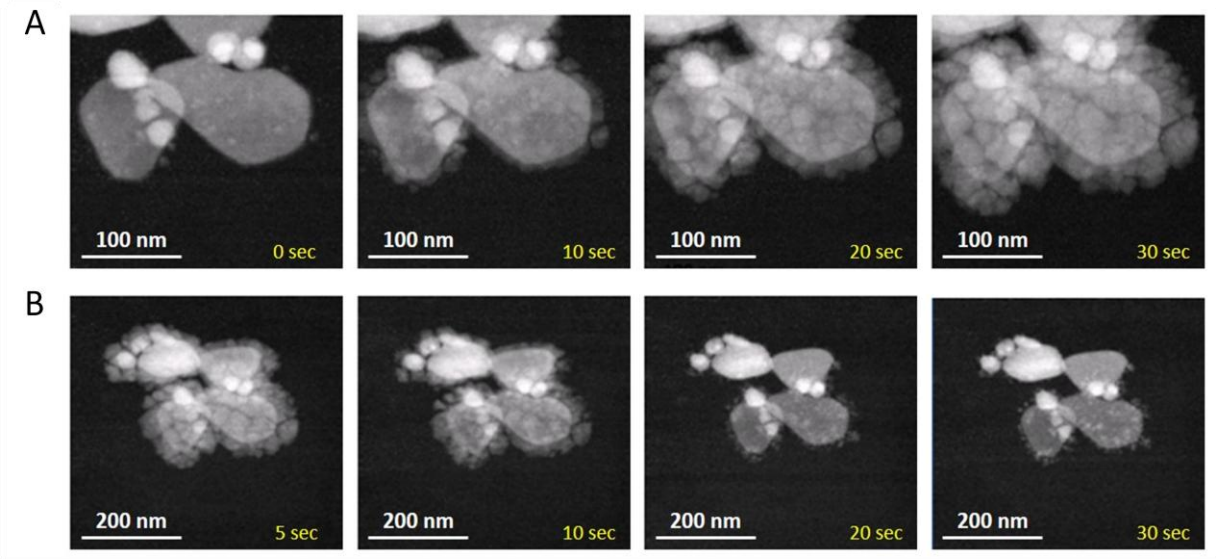

Fig 2: Cycle of deposition and dissolution of Cu nanoshell on gold nanoparticles in methanol. (A) Nucleation and growth of Cu nanoshells monitored by STEM HAADF with a magnification of 800 k (dose rate = 6.1 electrons/Å^{2}s). (B) Dissolution of Cu nanoshells monitored by STEM HAADF with a magnification of 400k (dose rate = 1.5 electrons/Å^{2}s). The irradiation time at a given magnification is indicated in the bottom right corner of each image.

More importantly, these growth/etching phenomena are cyclic processes that can be repeated many times on the same area with the same dose-rate-dependant behaviour. By cycling back and forth between deposition and dissolution, we could clearly establish that Cu growth is activated for dose rate greater than or equal to 6.1 electrons/Å^{2}s (magnification of 800k), while Cu dissolution occurs for dose rate below or equal to 1.5 electrons/Å^{2}s (magnification 400k). At intermediate magnifications between these two ranges neither growth nor etching is possible. As

observed in figure 3, the Cu shells formed when magnification reaches 800k are stable when magnification is maintained at 600k or 500k.

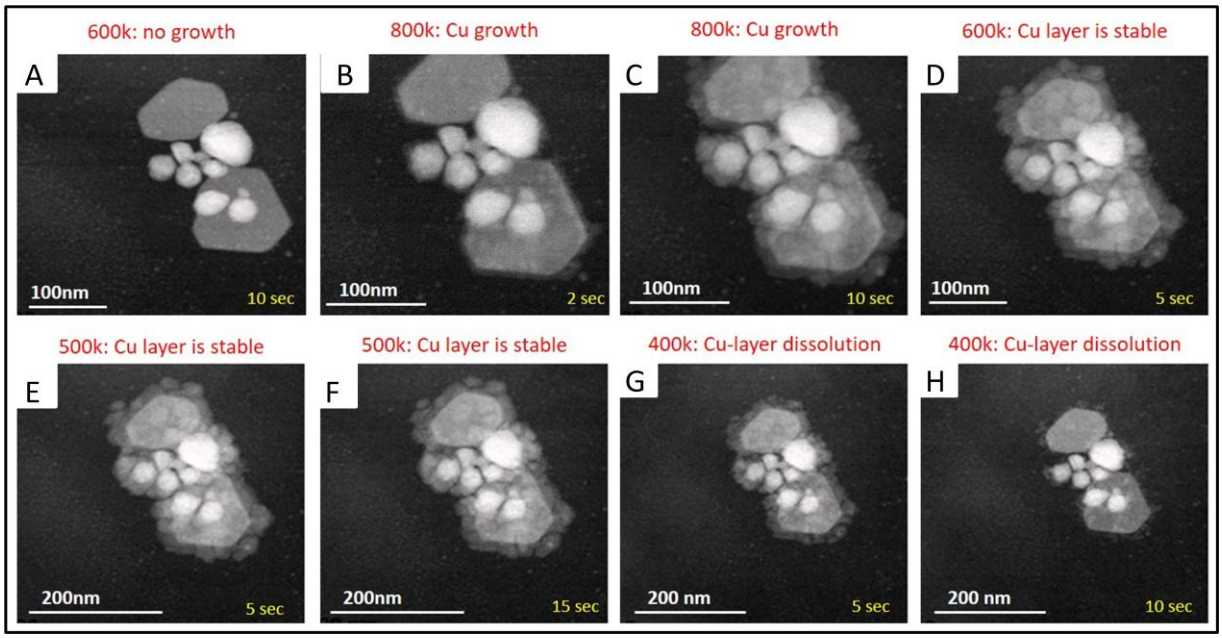

Fig 3: Strutural stability of the nanoparticles at intermediate dose rate. (A – H) Cycle of deposition and dissolution of Cu nanoshell on gold nanoparticles in methanol. The magnification and the observed phenomena are indicated above each image. The irradiation time at a given magnification is indicated in the bottom right corner of each image. At 500k and 600k, Cu shells are either absent (image a) or stable (images E and F).

5.5.1 Effect of Redox Cycling on Growth Kinetics of Cu Shells

Repeating growth and etching cycles on the same nanostructure reveals further interesting dynamics. Indeed, if the dose-rate-dependent behaviour of Cu remains similar over several cycles, the repetition of these reversible processes clearly affect the growth kinetic and the resulting structure of the Cu layer.

Figure 4 shows Au-Cu nanostructures after four consecutive Cu-growth steps of 20 seconds performed at 800k (Fig. 4B, 4D, 4F and 4H) and three dissolution steps of several minutes performed at 400k (Fig. 4C, 4E and 4G). The thickness of the Cu-shells obtained after 20 seconds of growth obviously increases with cycling, owing to the rising of the growth rate from a cycle to

another (figure 5). Additionally, surface roughness also increases with cycling. This tendency of Cu layers to be more and more dendritic when getting thicker highlights that the growth processes are increasingly limited by the diffusion of Cu atoms from the solution to the Au/Cu nanoparticles[15].

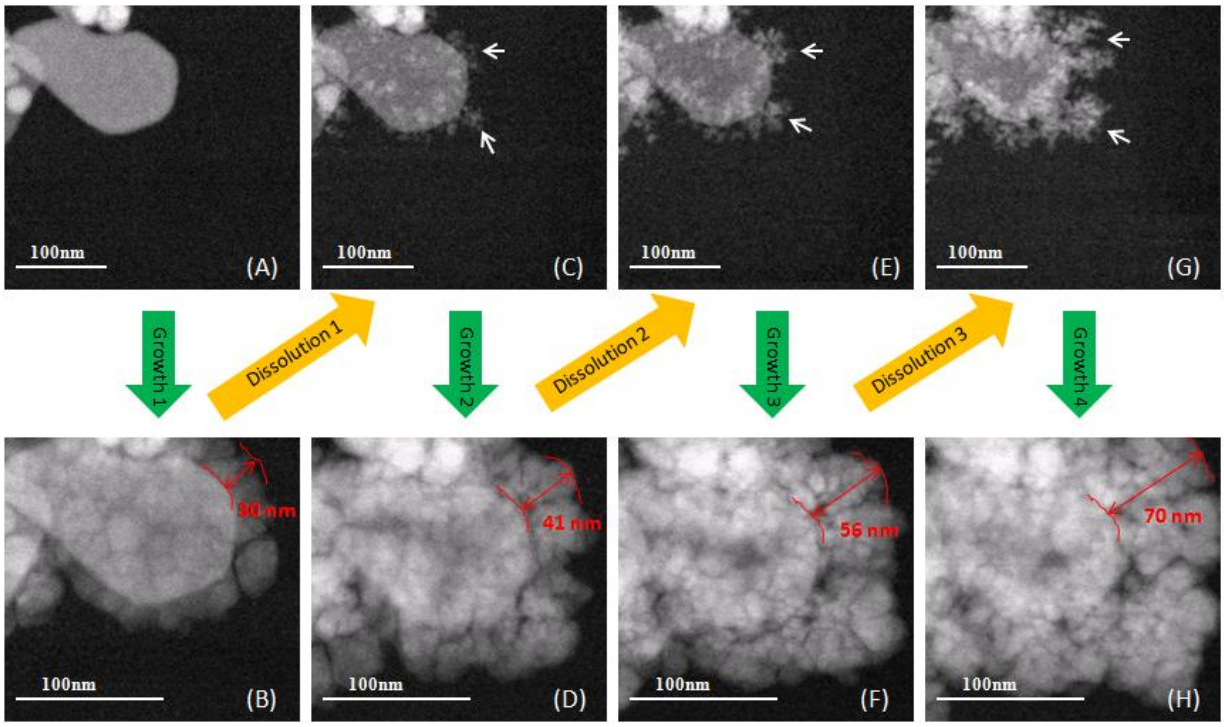

Fig 4: Four consecutive deposition/dissolution cycles of Cu nanoshells on gold nanoparticles in methanol. (A) Gold nanoparticles before Cu shell growth. (B, D, F, H) STEM-HAADF images of Au-Cu nanostructures after four consecutive Cu-growth steps of 20 seconds performed at 800k (dose rate = 6.1 electrons/Å^{2}s). The thickness of the Cu layers is indicated on each image. (C, E, G) STEM-HAADF images of Au-Cu nanostructures after three consecutive dissolution steps of several minutes performed at 400k (dose rate = 1.5 electrons/Å^{2}s). The remnant Cu on the gold nanoparticles after the dissolution steps is indicated by white arrows.

Figure 4 also reveals that deposition/dissolution cycles are not fully reversible. Indeed, Cu layers are never completely dissolved at the end of dissolution steps and many residual Cu particles are still observed on the Au nanoparticles after several minutes of observation at 400k.

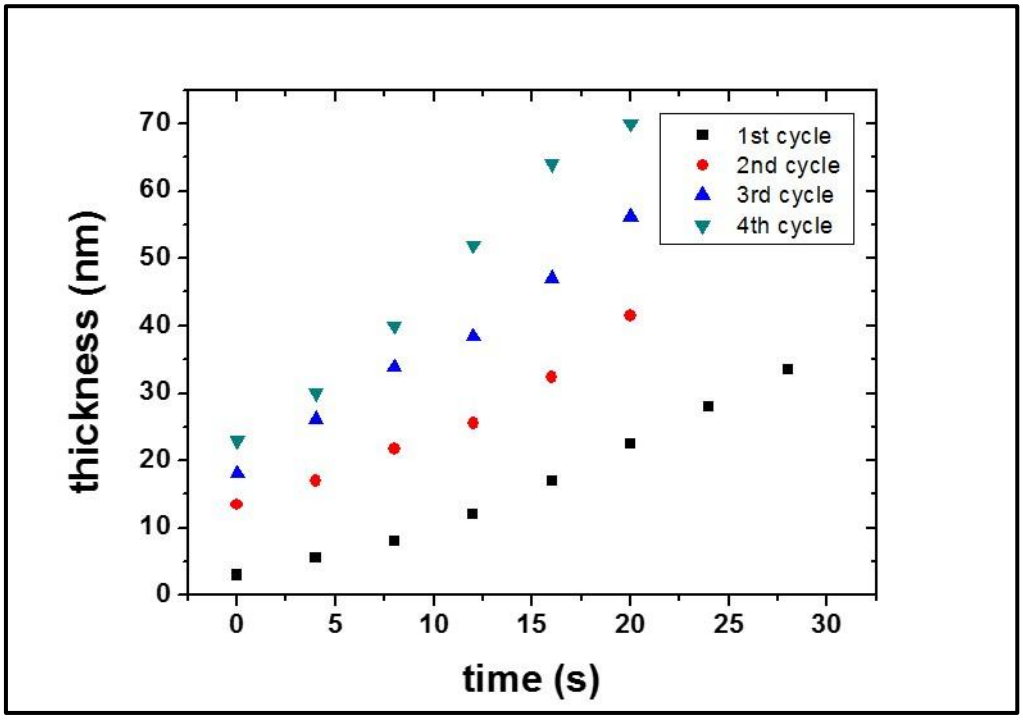

Fig 5: Evolution of the growth rate during deposition/dissolution cycling. Thickness of the Cu layer seen in figure 4 as a function of time during four consecutive growth steps.

Some of these persistent deposits do not seem to be anymore attached to the gold surface. We note that these Cu residues still persist even if we drastically reduce the magnification. Interestingly, the amount of Cu residues rises with cycling. This irreversible phenomenon certainly contributes to the growth-process enhancement of the Cu layers as these persistent Cu nanoparticles act as pre-existing nucleation sites during the next layer formation. The Cu deposition/dissolution mechanisms, here controlled by the electron beam, bear striking resemblance to electrochemical processes that occurs at the electrode/electrolyte interface during charge/discharge cycling of batteries. Mehdi et al[12]. have notably shown that Lithium deposition/dissolution mechanisms on a Pt working electrode were similarly influenced by the presence of remnant Li on the Pt surface after the discharge of their operando electrochemical cell.

5.6 Interpretation of Results

Radiolysis modelling developed by Schneider and co-workers indicated that the concentration ratio of the primary reducing (e_s) and oxidizing ($OH^{\bullet}$) species produced in pure water slightly

increases with the dose rate[21]. This qualitative result was exploited to explain the beam-induced growth and dissolution of gold nanoparticles observed in water by the same authors. As in our LCTEM experiment in methanol, nanoparticle growth was activated at higher dose rate than their dissolution and a dose-rate range of stability was observed in between.

By drawing an analogy with water, we can then hypothesize that in methanol high dose rate generates a reducing environment because of predominant effects of solvated electrons, whereas low dose rate induces an oxidizing medium due to a higher concentration of $CH_3O^{\bullet}$. In between, the dose-rate range of Cu-shell stability certainly corresponds to an equilibrium between competing redox reactions. Although this hypothesis satisfactorily explains the beam-dependent behavior of metals, many phenomena can also impact the redox reactions driving growth and dissolution processes. First of all, the only presence of $Cu(acac)_2$ influences the radiation chemistry of methanol because it inevitably leads to additional reactions, including the reduction of this metal precursor, that modify the steady state concentrations of radiolysis products[30]. In the experiment of Schneider *et al*. the presence of CTAB made possible the dissolution of Au nanoparticles *via* oxidative reactions with $OH^{\bullet}$, because halide ions, like Br^-, are complexing agents that lower the reduction potential of metals[5, 21]. In our experiments, such complexification mechanisms can be ruled out because the solution only contains Cu precursors. However, the direct contact between Au and Cu in an electrolytes solution can lead to the galvanic corrosion of Cu. Indeed, the difference in voltage potential between the Au and Cu will favor the dissolution of Cu that acts as the anode in a galvanic cell[31]. In a similar way that dead Li is formed during Li-battery cycling, the residual copper observed after the dissolution steps could then results from local contact losses between the Au cores and the Cu shells, preventing galvanic corrosion processes. Furthermore, the stability of metals in solution is directly linked to their voltage potential and the pH of the solution. On the one hand, the pH of the reaction medium is expected to change under irradiation[21], but local pH measurements remain challenging. On the other hand, the electric potential of metals can be modified by charging effects within the SiN substrate that increase with the dose rate and could generate charge transfer between the amorphous film and the supported nanoparticles[32]. Evaluating the respective weight of all these parameters is a key milestone to provide a quantitative understanding of the stability of metallic nanoparticles in LCTEM experiments.

5.7 Implications for LCTEM Studies

The possible implications of these results for LCTEM investigations, notably for electrochemical studies that have been one of the primary motivation for the development of this technique[33] are analyzed in this study. Common practice for studying electrochemical interfacial reactions consists in maintaining the electron dose below the electrolyte damage threshold[11]. Nevertheless, if the threshold of visible phenomena such as metal growth or polymerization, can be calibrated with LCTEM imaging, other chemical modifications can affect the electrochemical reactivity of materials without necessarily changing the electrolyte contrast. The present works show that very low-dose rate (< 1 electrons/$Å^2$s) in methanol seems to favour oxidizing environment that could affect externally-controlled deposition and dissolution of metals. It is worth noting that comparing cyclic voltammetry experiments acquired in a liquid-cell with and without electron irradiation could be an interesting approach to quantify the chemical and/or electronic modifications of the environment as a function of the dose rate.

5.8 Conclusion

It is shown here that the electron beam of a TEM can be exploited to control deposition / dissolution cycles of Cu nanoshells over Au nanoparticles in methanol. The mechanistic study of growth/etching cycles of Cu layers reveals that the kinetic of formation of Cu nanoshells increases with cycling because of the incomplete dissolution of the previous layers. The similar dose-rate-dependent behaviors of metallic nanostructures observed in aqueous and organic solvents allows assuming that the oxidizing or reducing nature of many environments can be tuned with the electron beam. In the present case, high dose rates create reducing media leading to the growth of metallic nanostructures, whereas low dose rates reinforce oxidizing media favoring metal etching. The dissolution of metallic nanostructures is not observed in all LCTEM experiments because metal etching most likely requires the help of complexing agents or bimetallic corrosion processes. More generally, this work highlights the crucial need for a better understanding of the electron beam effects that are neither linear with the dose rate nor necessarily marginal when very low-dose rate are used.

References

1. Liao, H.-G.; Niu, K.; Zheng, H. *Chemical Communications* **2013,** 49, (100), 11720-11727.
2. Ngo, T.; Yang, H. *The journal of physical chemistry letters* **2015,** 6, (24), 5051-5061.
3. De Jonge, N.; Ross, F. M. *Nature nanotechnology* **2011,** 6, (11), 695-704.
4. Ross, F. M. *Science* **2015,** 350, (6267), aaa9886.
5. Jiang, Y.; Zhu, G.; Lin, F.; Zhang, H.; Jin, C.; Yuan, J.; Yang, D.; Zhang, Z. *Nano letters* **2014,** 14, (7), 3761-3765.
6. Chee, S. W.; Pratt, S. H.; Hattar, K.; Duquette, D.; Ross, F. M.; Hull, R. *Chemical Communications* **2015,** 51, (1), 168-171.
7. Elgrabli, D.; Dachraoui, W.; Ménard-Moyon, C. c.; Liu, X. J.; Bégin, D.; Bégin-Colin, S.; Bianco, A.; Gazeau, F.; Alloyeau, D. *ACS nano* **2015,** 9, (10), 10113-10124.
8. Abellan, P.; Mehdi, B. L.; Parent, L. R.; Gu, M.; Park, C.; Xu, W.; Zhang, Y.; Arslan, I.; Zhang, J.-G.; Wang, C.-M. *Nano letters* **2014,** 14, (3), 1293-1299.
9. Woehl, T.; Abellan, P. *Journal of microscopy* **2017,** 265, (2), 135-147.
10. de Jonge, N.; Peckys, D. B. *ACS nano* **2016,** 10, (10), 9061-9063.
11. Holtz, M. E.; Yu, Y.; Gunceler, D.; Gao, J.; Sundararaman, R.; Schwarz, K. A.; Arias, T. A.; Abruña, H. D.; Muller, D. A. *Nano letters* **2014,** 14, (3), 1453-1459.
12. Mehdi, B. L.; Qian, J.; Nasybulin, E.; Park, C.; Welch, D. A.; Faller, R.; Mehta, H.; Henderson, W. A.; Xu, W.; Wang, C. M. *Nano letters* **2015,** 15, (3), 2168-2173.
13. Woehl, T. J.; Evans, J. E.; Arslan, I.; Ristenpart, W. D.; Browning, N. D. *Acs Nano* **2012,** 6, (10), 8599-8610.
14. Alloyeau, D.; Dachraoui, W.; Javed, Y.; Belkahla, H.; Wang, G.; Lecoq, H. l. n.; Ammar, S.; Ersen, O.; Wisnet, A.; Gazeau, F. *Nano letters* **2015,** 15, (4), 2574-2581.
15. Ahmad, N.; Le Bouar, Y.; Ricolleau, C.; Alloyeau, D. *Advanced Structural and Chemical Imaging* **2017,** 2, (1), 9.
16. Belloni, J.; Mostafavi, M.; Remita, H.; Marignier, J.-L.; Delcourt, M.-O. *New Journal of Chemistry* **1998,** 22, (11), 1239-1255.
17. Buxton, G. V.; Mulazzani, Q. G.; Ross, A. B. *Journal of Physical and Chemical Reference Data* **1995,** 24, (3), 1055-1349.
18. áde Jonge, N. *Chemical Communications* **2015,** 51, (91), 16393-16396.
19. Buxton, G. V.; Mulazzani, Q. G. *Electron Transfer in Chemistry* **2001**, 503-557.
20. Abellan, P.; Parent, L. R.; Al Hasan, N.; Park, C.; Arslan, I.; Karim, A. M.; Evans, J. E.; Browning, N. D. *Langmuir* **2016,** 32, (6), 1468-1477.
21. Schneider, N. M.; Norton, M. M.; Mendel, B. J.; Grogan, J. M.; Ross, F. M.; Bau, H. H. *The Journal of Physical Chemistry C* **2014,** 118, (38), 22373-22382.
22. Grogan, J. M.; Schneider, N. M.; Ross, F. M.; Bau, H. H. *Nano letters* **2013,** 14, (1), 359-364.
23. Henglein, A. *Chemical Reviews* **1989,** 89, (8), 1861-1873.
24. Baxendale, J. H.; Wardman, P. *The radiolysis of methanol: product yields, rate constants, and spectroscopic parameters of intermediates*; NATIONAL STANDARD REFERENCE DATA SYSTEM: 1975.
25. Ferradini, C.; Jay-Gerin, J.-P. *Radiation Physics and Chemistry* **1996,** 48, (4), 473-480.
26. Wardman, P. *Journal of Physical and Chemical Reference Data* **1989,** 18, (4), 1637-1755.
27. Sakamoto, M.; Tachikawa, T.; Fujitsuka, M.; Majima, T. *Advanced Functional Materials* **2007,** 17, (6), 857-862.
28. Hu, X.; Schuster, J.; Schulz, S. E.; Gessner, T. *Physical Chemistry Chemical Physics* **2015,** 17, (40), 26892-26902.
29. Venables, J.; Spiller, G.; Hanbucken, M. *Reports on Progress in Physics* **1984,** 47, (4), 399.
30. Park, J. H.; Schneider, N. M.; Grogan, J. M.; Reuter, M. C.; Bau, H. H.; Kodambaka, S.; Ross, F. M. *Nano letters* **2015,** 15, (8), 5314-5320.

31. Roberge, P. R., *Corrosion Engineering*. McGraw-Hill New York, NY, USA:: 2008.
32. Woehl, T. J.; Prozorov, T. *The Journal of Physical Chemistry C* **2015,** 119, (36), 21261-21269.
33. Williamson, M.; Tromp, R.; Vereecken, P.; Hull, R.; Ross, F. *Nature materials* **2003,** 2, (8), 532.

General Conclusion

The main goal of our work was to exploit LCTEM to understand the growth mechanisms of Au and Au-Cu nanoparticles during liquid-phase synthesis. In our case, the growth was simply induced by radiolysis of precursor loaded solvent. This beam induced radiolytic syntheses constitutes part of the LCTEM strategy which is used to observe dynamic processes taking place at solid / liquid interfaces. While many LCTEM studies focus on reducing the beam effects in LCTEM experiments, our works demonstrate that the electron dose and the electron dose rate can be effectively used to control the speed of the growth processes. This possibility to control the reaction kinetics in the TEM is a fantastic opportunity to distinguish the kinetic and thermodynamic effects that are related to the flow of matter and the environment-dependent stability of nanostructures (solvent nature, temperature, capping agent…), respectively.

The first results of this thesis (chapter 3) dealt with studying the effects of electron dose irradiation history on shape of Au nanoparticles. The results of this study were compared with an extended DLA model. The electron irradiation history was comprehensively taken into account implying that both instantaneous dose and cumulative dose were considered. These particular series of experiments were performed under high dose regime (>150 electrons/$Å^2$s) in TEM mode of microscope. Comparing LCTEM observations with DLA model explicitly revealed the atomic and molecular diffusion processes that affected the shape of dendritic nanostructures. Comprehensive evaluation of growth model established the fact that cumulative dose in the irradiated area induced drastic transitions in the growth mode of nanostructures. The study clearly showed that high dose rates in an irradiated area induces monomer depletion zones and hence the growth at this stage is driven by the extended diffusion pathways of the diffusing monomers. This subsequently resulted in anisotropic and dendritic growth due to the screening effect.

In chapter 4 kinetics and thermodynamics effects on the formation mechanisms of faceted Au nanoparticles was investigated. We systematically studied the effects of the dose rate, the solvent nature and capping agents on the faceting mechanisms of Au nanostructures. In water and methanol, the use of low dose rate condition lead to the formation of facetted nanostructures mainly including icosahedra, decahedra and nanoplates. *Ex situ* HRTEM analyses demonstrate

that the 2D or 3D shapes of these nanostructures was driven by crystal defects (stacking faults/ twinning) formation during the growth. Although the distribution of particle morphologies was not altered by the nature of the solvent, we have shown that transformation mechanisms of 2D nanoprisms to 2D hexagonal nanoplates are different when the solvent is changed from polar (water) to non polar (methanol). This critical *in situ* observation reveals that the nature of solvent is a critical extrinsic parameter for shape transformations, since it can modulates crystal defect formation and the surface energies of the exposed facets. Apart from these interesting mechanistic insights, differences in the growth rates of nanoplates in the two solvents were also observed. As both water and methanol contain strongly oxidizing and reducing radicals, this slight variation could be attributed to relative differences between the ratio of oxidizing to reducing radicals at the described dose rate regimes.

In second part of chapter 4 we functionalized the 3D particle seeds grown under low electron doses by flowing capping agent (DMA) to drive the formation of complex morphology (Au nanostars, NSs). Interestingly the formation of gold NSs was observed on icosahedral seeds but not on decahedral seeds which may point towards the effects of strain heterogeneity in the structure of seeds. By comparing the arrangement of NS arms along different projection axes with the aid of geometric models, it was established that the NSs derive their excellent symmetry from the initial shape of the seeds. This was further proved by formation of several partial NSs in the case of deformed seeds. Furthermore the concentration of capping agent played a crucial role in growth kinetics and overall tip sharpness of NSs. The most important insight gained from the *in situ* observation of these stellation processes was the fact that the inter-arm angle between the various arms changes continuously during growth. This points to the restructuration of high index facets during the growth process. Such kind of growth proves to be counter-intuitive from classical growth model point of view, however direct *in situ* observations in our work clearly points to this surface-diffusion-driven mechanisms. We believe that the use of DMA can contribute to surface diffusion processes along high index facets leading to continuous restructuration of high index facets during the entire growth cycle. Further examination of this growth process preferably by means of HRTEM could provide a concrete foundation for understanding the crystallographic changes occurring on the high index facets.

In the last chapter the tunability of redox environment in methanol with the aid of electron beam was studied. These realtime, spatially resolved observations of the growth/etching processes

enabled us to gain critical insights into the morphology and kinetics of growth at interfaces. Such type of studies are very relevant to electrochemical processes occuring inside batteries as they shed light onto the instabilities of the growth front. We were able to observe the growth of Cu shells on Au nanoparticles at high dose rates in STEM mode, while at lower electron doses etching was observed. As there was no external stimuli involved, the whole process was dictated by the relative concentrations of reducing and oxidizing species at a particular dose rate. We were able to inter-relate our findings with previous radiolytic studies on water and hypothesize that at low doses the concentration of main oxidizing species ($\cdot CH_3O$) is relatively higher than the primary reducing species (e_s^-) while the inverse is true at higher dose rates. It is also pertinent to mention here that metal etching is not universally observed for all metals under such conditions. Therefore additional factors such as complexing agents and bimettalic corrosion must be considered. Most electrochemical studies rely on threshold of visible phenomena such as metal growth or polymerization. Nevertheless other chemical changes without visible contrast can take place. Hence it is impossible to eliminate beam effects, but important to characterize them.

To conclude, it could be said with near certainty that liquid cell TEM is well placed to explore exciting new avenues within the domain of nanomaterial growth, electrochemical processes and radiation physics. Coupled with improvements in experimental instrumentation and data acquisition capabilities it is well on its way to address key material challenges. With hindsight, apart from the initial flurry of studies focusing on obtaining images of phenomena happening in liquid, more recent work is targeted towards implementing a greater range of stimuli such as flow, mixing, biasing, heating etc. The greatest challenge in all LCTEM studies is to quantify beam effects which are unavoidable. An improved understanding of beam-sample interactions is a necessary tool to interpret, minimize or exploit beam mediated phenomena. This aspect of LCTEM is further exacerbated by the interconnected nature of the chemical species produced. Improvement in the precision and accuracy of results also requires better understanding of membrane materials and liquid thickness profile as these can have serious consequences with regards to observed phenomena. Use of graphene and SiN window materials have clearly demonstrated differences in electron-dose-rate-dependent phenomena. Concerning the liquid thickness profile, it is necessary to choose an optimized value of thickness in order to replicate true bulk processes as well as maintain a reasonable resolution. Lastly with the current setup of capillary inlets and outlets, cross-contamination is also a big challenge. These effects need to be mitigated altogether to improve the reproducibility and reliability of experimental work.

Appendix

1. Measurement of Liquid Thickness Profile

Liquid thickness is an important parameter of liquid cell experiments. It helps to determine what is resolvable through liquid[1] as well as helping in determining whether the processes taking place in liquid cell are true representation of macroscopic processes. The method employed was to first check qualitatively at the beginning and end of experiment if the liquid cell is fully filled. This was done by taking a low magnification image of the cell. In the image illustrated in figure 1B, the contrast was always of a fully filled liquid with an increasing liquid thickness (i.e. the contrast decreases) from the corners to the center of the viewing window, due to an outward bowing of the SiN membranes under vacuum. A corresponding intensity profile as a function of distance (Figure 1C), taken diagonally across the liquid cell shows a decrease in number of counts as liquid thickness increases, further cementing this conclusion.

Then, energy-filtered TEM (EFTEM) was used to quantitatively evaluate the liquid thickness. These measurements were performed on a test liquid-cell filled with water, in 12.5 μm^2 areas near the corners of the liquid cell. EFTEM (or Electron-Energy-loss spectroscopy) is a very convenient technique to estimate the thickness of the sample (t) crossed by the electron beam[2]. We acquired an unfiltered image and a zero-loss filtered image from the same region with the same optical conditions. Then, these two images were used to compute a relative thickness map (figure 2A) by using the Poisson statistic of inelastic scattering:

$$\frac{t}{\lambda} = -\ln\left(\frac{I_0}{I_t}\right)$$

with λ being the inelastic mean free path of electron in the sample, t the sample thickness, I_0 and I_t the intensity of the filtered and unfiltered images, respectively.

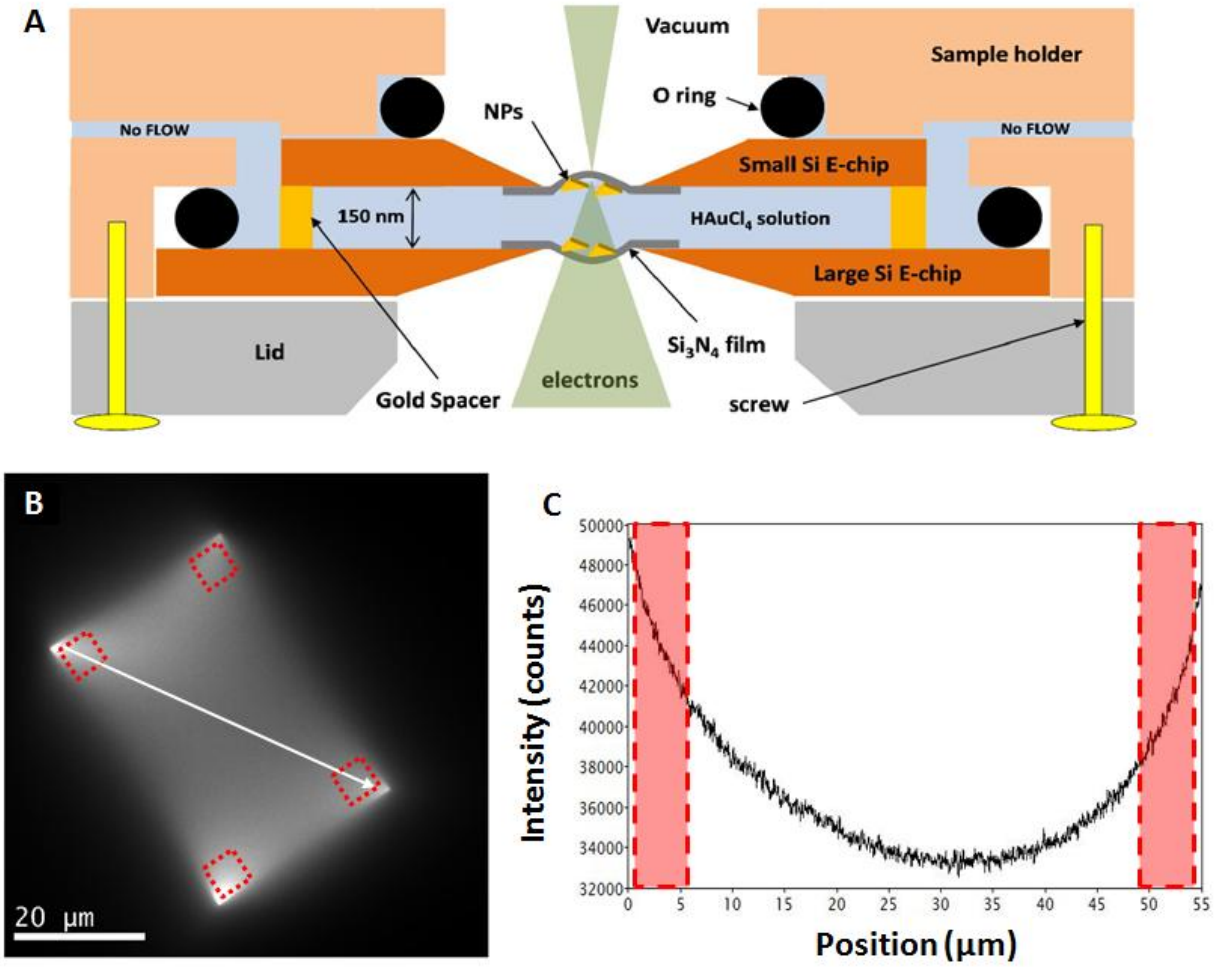

Fig 1. ***(A) Schematic cross section of the sealed liquid cell in the JEOL ARM microscope. (B) Low-magnification TEM image of the viewing window after imaging showing the characteristic contrast of a filled liquid cell. The 12.5 µm^2 observation areas are indicated by red squares. (C) Intensity profile measured along the white arrow indicated on the low magnification image.***

On this thickness map we can measure the t / λ profile that show the variability of the liquid thickness in the liquid-cell because of the bowing effect (black curve in figure 2B). As expected the lowest t / λ values are found at the corners and this ratio increases linearly along the diagonal of the viewing window. It is worth noting that this signal is affected by both the water layer and the two SiN membranes that encapsulate the liquid. Nevertheless, given that:

$$\left(\frac{t}{\lambda}\right)_{sample} = \left(\frac{t}{\lambda}\right)_{water} + \left(\frac{t}{\lambda}\right)_{SiN\ membranes}$$

we can easily deduce the contribution of the SiN films by measuring the t / λ value of a single membrane. The relative thickness map of a SiN film acquired with the same optical conditions has a mean t / λ ratio of 0.36 ± 0.02. Assuming that the two membranes have the same thickness, we can extract the t / λ profile of water in the liquid-cell (red curve in figure 2B). Importantly, we note that the t / λ profiles were very similar in all corners of the liquid-cell.

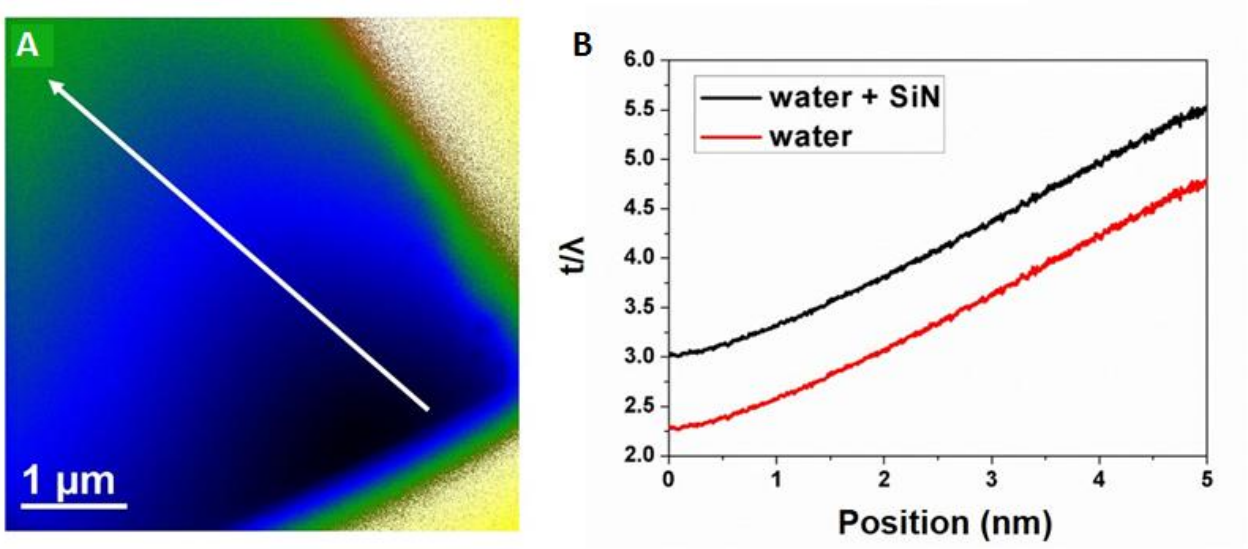

Fig 2: (A) Relative thickness map of a corner area of the liquid cell filled with water. (B) t/λ profile measured along the white arrow indicated on the thickness map (black curve). The red curve corresponds to the t/λ profile from which the contributions of the two SiN membranes (0.36 per film) has been subtracted.

Previously reported EELS measurements of liquid-cell thickness showed that in the microscope each membrane bows out and takes a parabolic shape that are orthogonal to each other. Because of this liquid cell geometry, most likely due to the cross configuration of the two rectangular windows, the water layer is thinner at the corners where its thickness was found to roughly correspond to the thickness of the gold spacers separating the two E-chips[1]. The parabolic intensity profile measured along the diagonal of the viewing window on the low-magnification image of the liquid-cell (figure 1C) indicates that during our experiments, the liquid cell takes this very common geometry. If we assume that the thickness of liquid at the corner is 150 nm (thickness of the gold spacers), we can conclude that the liquid thickness in 12.5 μm^2 area near the corner of liquid cell varies linearly along the diagonal of the viewing window. All the images

and videos of the present work were recorded in 12.5 μm^2 areas located 1 µm away from the liquid-cell corners (Figure 1B). By extrapolating the t / λ curves 1 µm further along the x-axis, we estimate that the water thickness in the observation areas to vary from 185 nm to 350 nm. These observation areas were chosen as contrast is significantly higher than in the middle of the liquid-cell.

Note that in chapter 3, the use of high dose rate illumination in TEM mode favours the formation of H_2 bubbles due to intensive radiolysis processes. This production of gaseous H_2 occurs when the concentration of this radiolysis product exceed the saturation level of water[3]. Interestingly, this sudden phenomena completely changes the liquid distribution, since a very large H_2 bubble is immediately formed at the centre of the liquid cell (figure 3A). As the SiN membranes are hydrophilic, a very thin layer of water remains between the gas bubble and the membranes. The presence of the liquid in the central region of the liquid cell is confirmed by the observation of nanoparticle growth and diffusion phenomena that would not occur if the membranes were dried. Low-magnification image of such bubble-filled liquid cells (figure 3B) illustrates that the liquid thickness is then very thin in the central region and increases in the corners as shown in figure 3C at a much higher magnification. This phenomena can be used to improve TEM image resolution in liquid. As illustrated in Chapter 3, atomic-scale images of growing nanoparticles can then be obtained, suggesting that the liquid layer in the central region does not exceed a few tens of nanometers. Further works are in progress to measure the thickness of these very thin liquid films by EFTEM.

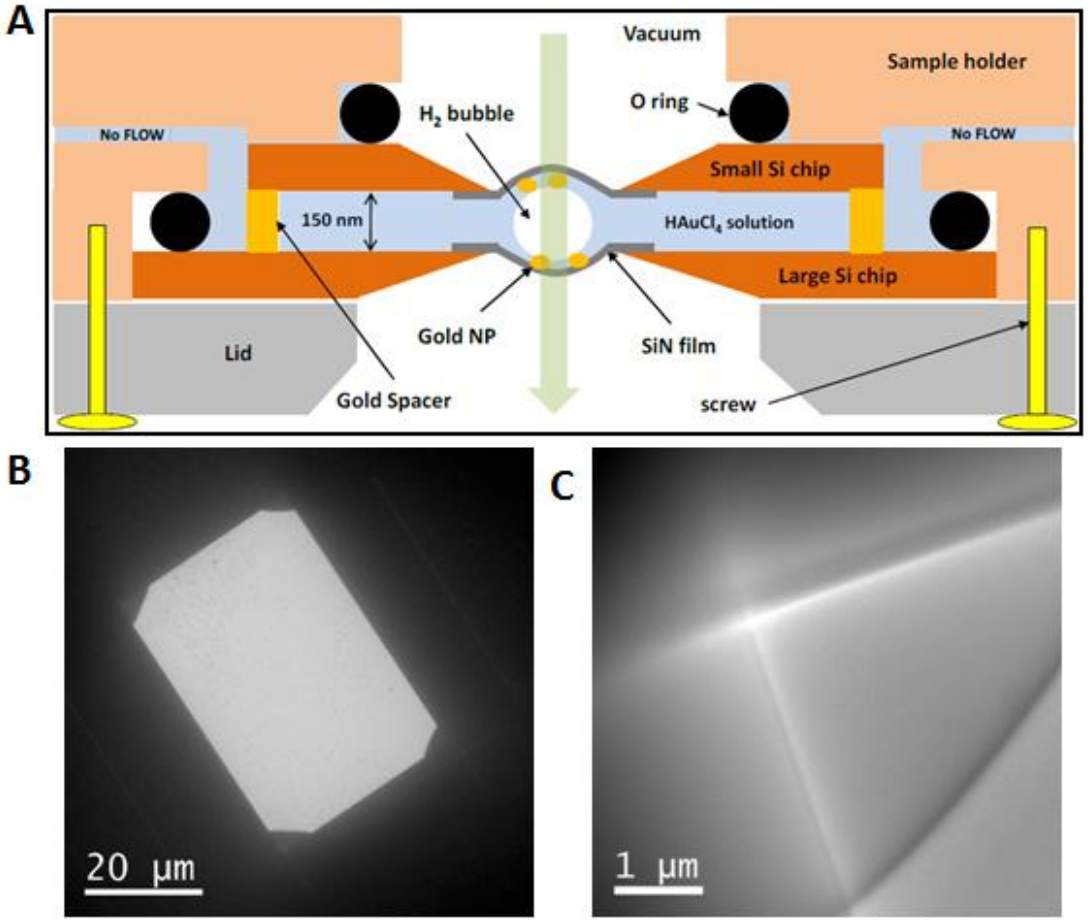

Fig 3: (A) Schematic cross section of the sealed liquid cell in the JEOL ARM microscope under high dose rate with a H_2 bubble at the center of the viewing area. (B) Low-magnification TEM image of the viewing window after high-dose rate TEM imaging, showing the characteristic contrast of a bubble-filled liquid cell. (C) Higher magnification image of the liquid-cell corner where the liquid thickness rapidly increases and where the liquid/gas interface is directly observed.

References

1. Holtz, M. E.; Yu, Y.; Gao, J.; Abruña, H. D.; Muller, D. A. *Microscopy and Microanalysis* **2013,** 19, (4), 1027-1035.
2. Egerton, R. F., *Electron energy-loss spectroscopy in the electron microscope*. Springer Science & Business Media: 2011.
3. Grogan, J. M.; Schneider, N. M.; Ross, F. M.; Bau, H. H. *Nano letters* **2013,** 14, (1), 359-364.